ISSN 8755-6839

SCIENCE OF TSUNAMI HAZARDS

Journal of Tsunami Society International

Volume 39 Number 4 2020

WWW.TSUNAMISOCIETY.ORG

TSUNAMI SOCIETY INTERNATIONAL, 1741 Ala Moana Blvd. #70, Honolulu, HI 96815, USA.

SCIENCE OF TSUNAMI HAZARDS is a CERTIFIED OPEN ACCESS Journal included in the prestigious international academic journal database DOAJ, maintained by the University of Lund in Sweden with the support of the European Union. SCIENCE OF TSUNAMI HAZARDS is also preserved, archived and disseminated by the National Library, The Hague, NETHERLANDS, the Library of Congress, Washington D.C., USA, the Electronic Library of Los Alamos, National Laboratory, New Mexico, USA, the EBSCO Publishing databases and ELSEVIER Publishing in Amsterdam. The vast dissemination gives the journal additional global exposure and readership in 90% of the academic institutions worldwide, including nation-wide access to databases in more than 70 countries.

OBJECTIVE: Tsunami Society International publishes this interdisciplinary journal to increase and disseminate knowledge about tsunamis and their hazards.

Submit manuscripts of research papers, notes or letters to the Editor. If a research paper is accepted for publication the author(s) must submit a scan-ready manuscript, a Doc, TeX or a PDF file in the journal format. Issues of the journal are published electronically in PDF format. There is a minimal publication fee for authors who are members of Tsunami Society International for three years and slightly higher for non-members. Tsunami Society International members are notified by e-mail when a new issue is available.

Recent and all past journal issues are available at: http://www.TsunamiSociety.org CD-ROMs of past volumes may be purchased by contacting Tsunami Society International at postmaster@tsunamisociety.org Issues of the journal from 1982 thru 2005 are also available in PDF format at the U.S. Los Alamos National Laboratory Library http://epubs.lanl.gov/tsunami/

ISSN 8755-6839

SCIENCE OF **TSUNAMI HAZARDS**

Journal of Tsunami Society International

Volume 39 **Number 4** **2020**

THE SIMULATION STUDY OF GNSS SIGNAL REFLECTION IN MONITORING SEA LEVELS AND TSUNAMI

Buldan Muslim[1)], Mokhamad Nur Cahyadi[2)], Bambang Sunardi[3)] and

Charisma Juni Kumalasari[3)]

[1] *National Institute of Aeronautics and Space (LAPAN), Bandung 40173, Indonesia*

[2]*Department of Geomatics Engineering, Institut Teknologi Sepuluh Nopember Kampus ITS Sukolilo ,Surabaya, 60111, Indonesia*

[3]*Mathematics Department, Master's Programme, Institut Teknologi Sepuluh Nopember, Surabaya 60111, Indonesia*

Corresponding author: mbuldan@gmail.com

ABSTRACT

A real-time Global Navigation Satellite System (GNSS) data managed by the Geospatial Information Agency (BIG) can be developed for indirect tsunami monitoring. This involves using GNSS TEC data due to the atmospheric-ionosphere coupling through tsunami-triggered infrared waves. The application of this method is, however, limited to tsunamis originating from earthquake epicenter which is far from the coast. Meanwhile, the arrival of tsunamis to the coast requires a longer time than the propagation of infrasound waves into the ionosphere. This GNSS signal reflection technique can, therefore, be used to detect tsunamis which are close to shore in order to overcome the detection weakness associated with the GNSS TEC and also routinely used to monitor sea waves. This research conducted a simulation of this technique using single-frequency code distance data to determine the sea level and the results showed its effectiveness in determining sea wave height using one differentiation. It is also possible to ignore the difference in the bias of two receivers of direct and reflected signals by sea-level assuming they are similar and have identical antennas. The use of pseudo distance from the GNSS signal code data makes it possible to estimate the height of the sea waves by simulation with a standard deviation of approximately 5.6 cm.

Keywords: GNSS, Signals, Reflections, Sea Levels, Tsunamis

1. INTRODUCTION

Sea level monitoring is an important concept in understanding several aspects of hydrosphere such as local hydrodynamics, tidal wave activity, and others. It is also related to the weather due to the ability of typhoons to cause major damage in coastal areas in extreme conditions and greater damage associated with tsunamis. Therefore, the Meteorology Climatology and Geophysics Council (BMKG) builds and operates a tsunami early warning system motivated by the Aceh earthquake and tsunami of December 26, 2004 (Harijono et al. 2010).

Tides are a natural phenomenon defined as the periodic rise and fall of sea levels due to the gravitational forces of celestial bodies, especially the moon and the sun. The influence of other astronomical objects can, however, be ignored due to their relatively smaller distance and size compared to the moon and sun. Meanwhile, the non-astronomical factors influencing tides, especially in semi-closed waters such as bays, are the shape of the coastline and the bottom topography of the waters (R.H. Stewart. 2008).

Sea level is monitored conventionally by tidal devices which measure the vertical distance of the water surface from the point of observation. Several countries operate tidal observation networks to monitor changes in sea level due to the ability of the measurement tools to provide precise and accurate results. The installation of these devices, however, requires direct contact with water and this limits their frequent use and maintenance. Moreover, the equipment is very vulnerable to coastal hazards such as coastal flooding and tsunamis thereby causing measurement errors and damage during the extreme natural phenomenon. They also require expensive regular maintenance, especially due to the need of divers (Artru et al. 2005).

GNSS has the ability to function as an alternative approach to sea level monitoring, especially due to some signals received through reflections from a surface near the antenna which are called multipath (Artru et al. 2005). This, therefore, means there is possibility of using the multipath technique for tidal monitoring and, unlike the devices used in measuring sea level near shore, it also has the ability to monitor sea levels far from shore. The extent of sea-level monitoring with GNSS, however, depends on the height of its antenna and the elevation angle of its satellite. Therefore, the GNSS signal reflection technique is also applicable for tsunami monitoring when it is slightly far from the coast.

GNSS has been successfully applied for positioning, navigation, and remote regulation over the past few decades, especially the GNSS-Reflectometry (GNSS-R) which is an innovative sensing technique using GNSS signals reflected from the Earth's surface (Jin et al. 2005 and Zavarot et al. 2014). Its data application for marine altimetry was first proposed by (Martin-Neira. 1993) while Garrison et al. also conducted a study on the reflected signal of the global positioning system (GPS) used for roughness on the reflection surface (Garrison et al. 1998).

In sea-level observations, especially coastal areas, it is usually difficult to use radar altimeters. Moreover, geophysical factor models such as the earth's gravitational field or ocean currents are not sufficient to predict local sea levels and the changes in these levels in the 21st century are usually accompanied by storm surges and extreme flood (Semmling et al. 2012) which are dangerous for the population.

Stosius et al. (2010) conducted a tsunami detection simulation using GNSS-Reflectometry in the Indian Ocean with the focus on six historic tsunami events generated by earthquakes with different magnitudes in several types of constellations and orbit parameters, as well as the GNSS-R carrier phase compared to the PARIS approach or the altimetry code (Peltier and Hines. 1976).

Muslims et al. (2019) also conducted a simulation study using the JOG2 station and the results showed the reflecting point with the ability to reflect GNSS signals and are received at an altitude of about 20 meters from sea level has the furthest distance around 1150 meters from receivers on the beach (Muslim et al. 2019). The tsunami has a speed of 75.2 m/s at a depth of 1000 meters for the coast with a depth of 30 degrees and, assuming a constant speed, it was observed to have reached the coast in 13 seconds. This time is not enough to make people avoid the tsunami based on the early warning system and in order to ensure it is effectiveness, the GNSS signal amplifier antenna is required to be at least 60 m high to produce a 39-second chance of avoiding a tsunami. The study of GPS satellite elevation angles with signal receiver antennas at a height of 20 meters showed the availability of satellites observed in the GPS signal simulation at JOG2 station has an elevation angle lesser than 30 degrees by the sea for almost 24 hours except at 11:00 AM-11:50 AM.

This paper provides a brief overview of the simulations of GPS signal reflections to determine sea level using an IGS station, JOG2, located in Java. The process involved investigating the sea level estimation using pseudo distance data of GPS code signals at L1 frequency.

2. METHODOLOGY TO DETERMINE THE SEA LEVELS WITH GNSS SIGNAL REFLECTIONS

The absolute sea level height can be obtained based on ITRF using two receivers, RHCP receiver facing upward or peak and LHCP facing sea level or nadir (Rudenko et al. 2019). The RHCP receiver receives signals coming directly from the GNSS satellite and is used to estimate the absolute position of the antenna (Lofgren et al. 2014) while LHCP receivers receive those reflected by the sea level (Chen et al. 2012).

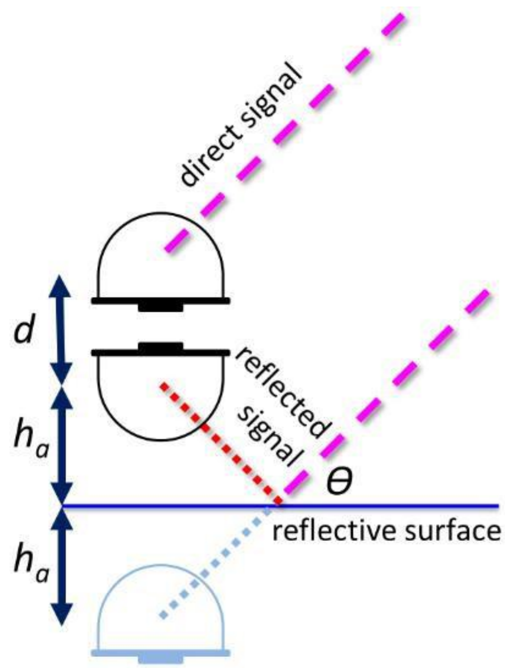

Figure 1. The arrangement of the direct signal receiver antenna as a reference station (above), the reflected signal (below) from the GNSS satellite, and the shadow rover antenna (below sea level).

First, the baseline between RHCP and LHCP antennas needs to be determined to obtain sea-level changes. The arrangement of the direct and reflected signal receiver antenna is, however, explained in Figure 1.

According to the figure, when a nadir antenna receives a signal reflected from the sea level, it is possible to assume a direct signal below sea level is received with an elevation angle Θ and the reflected signal observed is considered the rover receiver data while the direct signal is considered the reference station data. The equation of the rover antenna position can, therefore, be formulated with an ordinary differential method in order to determine the relative position. In Figure 1, d is the actual distance between the direct and reflected signal receiving antennas while ha is the sea level height which is the same for the shadow rover receiver below the sea level (Muslim et al. 2019).

A change in the sea level causes a variation in the ha and the sea level height is directly related to the basic distance between the reference antenna and rover with a geometric relationship.

$$\Delta v = 2h_a + d$$

where:

Δv is the baseline between the RHCP and LHCP antennas
h_a is the distance between the LHCP antenna and sea level
d is the distance between the phase center of the RHCP and LHCP antennas

RHCP and LHCP antennas allow users to change the base and sea levels in the ITRF reference.

2.1 The positioning of shadow rover receiver antenna using phase data

One of the methods used to estimate the position of the shadow rover is the differential method with the GNSS observation equation for two different receivers, A (reference) and B (rover), stated as follows:

$$L_A^j = \rho_A^j + c(\tau_A - \tau^j) + Z_A^j - I_A^j + B_A^j + \epsilon \quad (1)$$
$$L_B^j = \rho_B^j + c(\tau_B - \tau^j) + Z_B^j - I_B^j + B_B^j + \epsilon \quad (2)$$

where:

L_n^j : Phase distance data observed ($\lambda\Phi_n^j$)

B_n^j : Ambiguity phase (λN_n^j) in meter

ρ_n^j : satellite geometry to the receiver

c : Speed of light

τ_n : receiver time bias

τ^j : satellite time bias

Z_n^j : troposphere bias

I_n^j : ionosphere bias

ϵ : multipath and noise

The difference between the two observations of the direct (A) and reflected (B) signals from the same satellite produces the following equation:

$$\Delta L_{AB}^{j} = \Delta \rho_{AB}^{j} + c\Delta \tau_{AB} + \Delta B_{AB}^{j} \tag{3}$$

The result of a single difference between the two receivers has receiver bias errors as observed between the master and rover receivers as well as the variation in the level of ambiguity between the two receivers. There is, however, the opportunity to eliminate the receiver time bias and phase ambiguity cycles using the differences from the single difference equation in the two epochs which are written as follows

$$\nabla \Delta L_{AB}^{jk} = \nabla \Delta \rho_{AB}^{jk} + \nabla \Delta B_{AB}^{jk} \tag{4}$$

The distance of the two receivers between the two epochs can be determined using the least-squares method after the variation in the phase distance between them is known. Subsequently, the sea level height determined at the beginning of the measurement can be used as the reference at the next epoch by integration.

2.2 Determination of the distance of the master and rover receivers with GNSS code distance data

There is no need to eliminate the difference in the number of ambiguity cycles with the use of code data. Moreover, using an identical receiver and antenna makes it possible to consider the difference in the receiver bias as zero and this means the variations can be used to propagate the distance between GNSS signals through reflection and direct to determine the distance of the two receivers or the distance of a shadow rover receiver and master receiver.

The use of code data and two identical receivers and antennas with the same model, brand, antenna, and cable length of the antenna to receiver can be used to formulate equation (3) in relation to the vertical distance of the two receivers as follows

$$\Delta P_{rm}^{j} = \Delta \rho_{rm}^{j} = h_{rr}^{i} Sin\left(\alpha^{j}\right) \qquad (5)$$

Therefore, the height of the rover receiver from the master is written as follows

$$h_{rr}^{i} = \frac{\rho_{r}^{j} - \rho_{m}^{j}}{\sin \alpha} + \ \ d \qquad (6)$$

α is the elevation angle of the GNSS satellite j as seen from the master receiver while d is the distance of the master from the actual reflecting receiver located just below the master receiver but with the antenna facing down. Meanwhile, there is an opportunity to ignore the d in case it is very small, for example 10 cm, when arranging the antenna height at 20 meters from sea level to anticipate tsunamis reaching more than 15 meters.

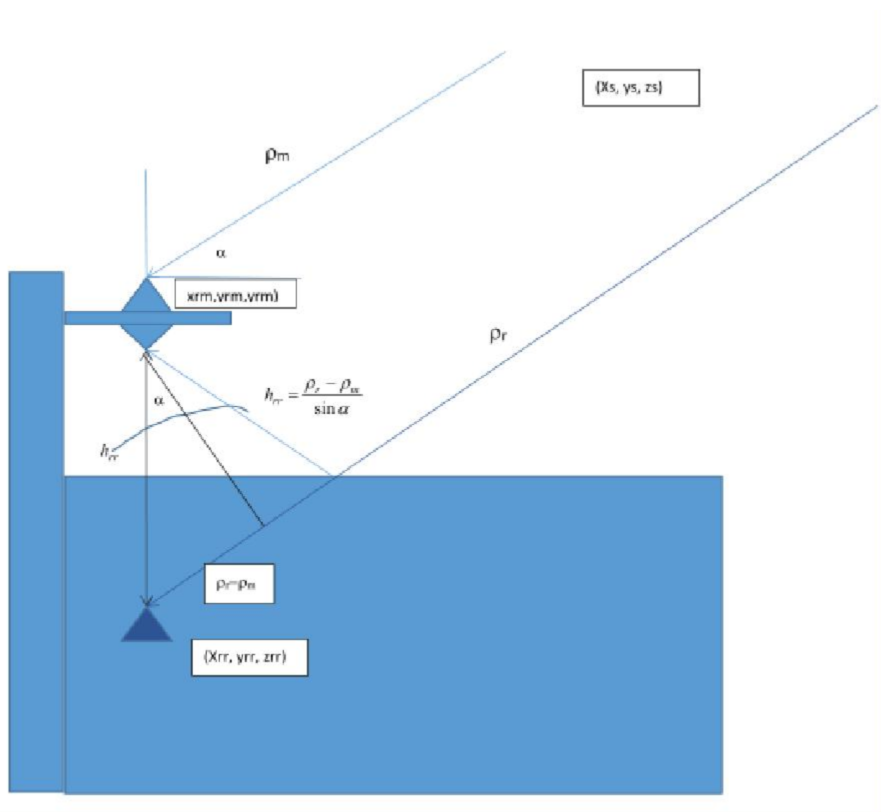

Figure 2. Scenarios for reflection and direct propagation of GNSS signals on shadow and actual rover receivers

The position of the reflected signal receiver is considered to be a shadow rover receiver at the following depth:

$$h_{rr} = h_{rm} - 20 - 2\sin\left(\frac{2\pi}{24}t\right) \tag{7}$$

2.3 Simulation Method of GNSS signal reflection data

The process involved in simulating the GNSS signal reflection data is as follows:

a. Changing ECEF satellite coordinates (xs, ys, zs) to geodetic coordinates (latitude, longitude, altitude (lbh))
b. Changing the coordinates of the ECEF receiver to lbh
c. Calculating the satellite elevation angle from the master receiver
d. Determining the coordinates of the rover receiver in a simulation

The GNSS signal is reflected based on the assumption that it is straight and received by a shadow (pseudo) rover receiver below sea level at an equal distance with the actual receiver to the sea level. In a situation the sea level is undulating with a period of 24 hours and a height of 1 meter which fulfills the sine wave equation,

$$Gal = -\sin\left(\frac{2\pi}{24}t\right) \tag{8}$$

then the height of the hrr shadow rover receiver can be calculated using equation (7).

The latitude and longitude coordinates of the shadow receiver are also the same as those of the master receiver. In this case, the sea level height from the master receiver is half the distance of the shadow rover receiver to the master receiver, which is $h_{al} = 0.5hrr$

e. Calculating satellite distance to the master receiver using the following relationship:

$$R_{rm}^{j} = \sqrt{\left(x_s^j - x_{rm}\right)^2 + \left(y_s^j - y_{rm}\right)^2 + \left(z_s^j - z_{rm}\right)^2} \tag{9}$$

f. Calculating satellite distance to the shadow rover receiver using the following equation:

$$R_{rr}^{j} = \sqrt{\left(x_s^j - x_{rr}\right)^2 + \left(y_s^j - y_{rr}\right)^2 + \left(z_s^j - z_{rr}\right)^2} \tag{10}$$

g. Simulating the data on satellite distance to the rover receiver which is identical to the direct signal received in the shadow in such a way it is assumed to be below the sea level receiving the direct signal even though it is above receiving the signal reflected by the seawater. The distance of the satellite received at the rover receiver is proportional to the comparison of its distance with the master receiver, which can be written as follows

$$\rho_r^j = \frac{R_{rr}^j}{R_{rm}^j}\rho_m^j \tag{11}$$

h. Calculating the distance of the shadow rover from the master receiver from the GNSS signal reflection data using formula (6)

In case the d is assumed to be very small, geometrically, the distance between the rover and master receivers is as follows:

$$h_{rre}^j = \left(\frac{\rho_r^j - \rho_m^j}{\sin\alpha}\right) \tag{12}$$

i. Calculating the height of sea level from the master receiver

The sea level height is half the distance of the rover from the master receiver and this is indicated in the following equation

$$h_{al}^j = \frac{1}{2}h_{rre}^j \tag{13}$$

j. Calculating the average sea level height from the master

Wave height is measured from the average sea level height per day. Therefore, the estimated sea level height needs to be averaged as follows:

$$h_{alrat}^j = \frac{1}{N}\sum_{t=0}^{t=N} h_{alrat}^j \tag{14}$$

k. Calculating sea wave height using the following equation

$$g_{ale}^{j} = h_{ale}^{j} - h_{alrar}^{j} \quad (15)$$

l. The actual sea wave height from the simulation is defined as follows

$$g_{al} = h_{rrm} - h_{rmmrat} \quad (16)$$

m. Estimation error of sea level height

The estimation error of sea level height from GNSS signal reflection data was calculated using the following relationship

$$\delta_{gale} = g_{ale}^{j} - g_{al} \quad (17)$$

The simulation method to calculate the sea waves from GNSS signal reflection data is shown in the following diagram.

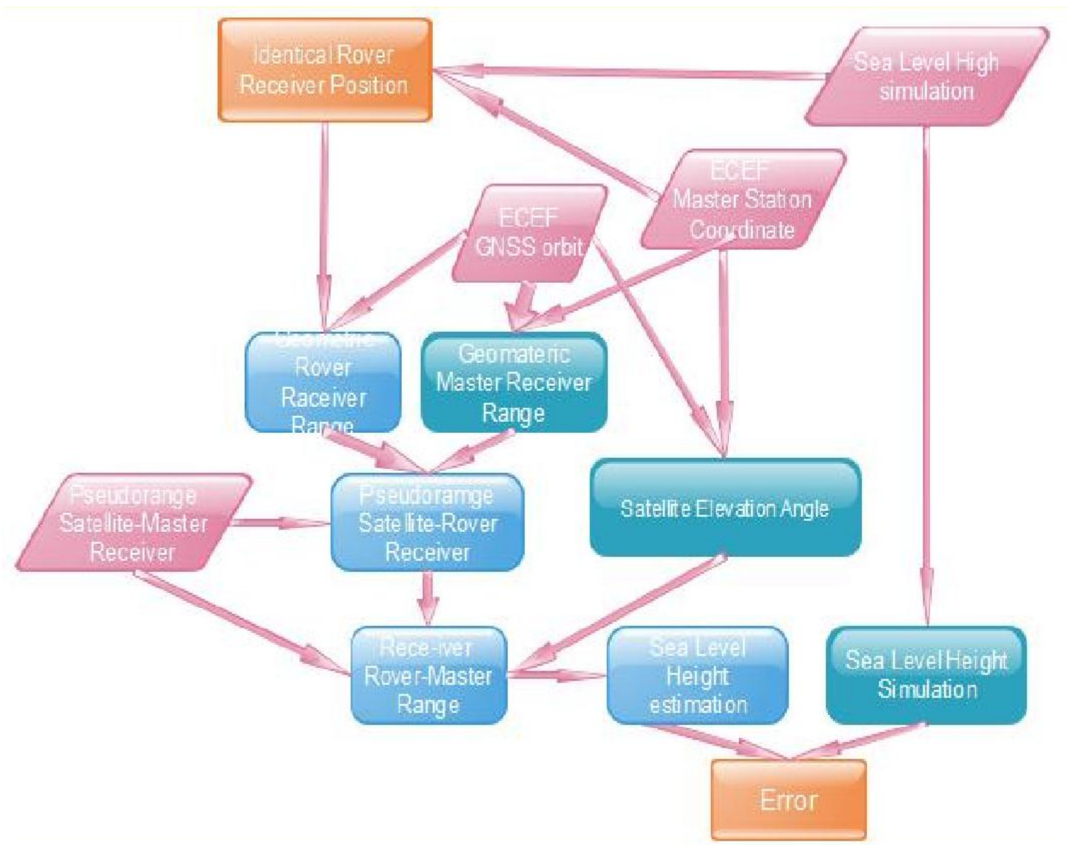

Figure 3. Methodology for estimating sea level height with the pseudo distance of GNSS signal code

3. RESULT AND DISCUSSION

Figure 4 shows a simulation of sea waves where the x-axis is UT and the y-axis is the sea wave height in meters. In this simulation graph, the waves experienced tides with a minimum value at 06:00 UT which corresponds with equation (10) at a period of 24 hours and an amplitude of 1 meter. Moreover, the minimum wave value due to the simulation equation at 06:00 is negative.

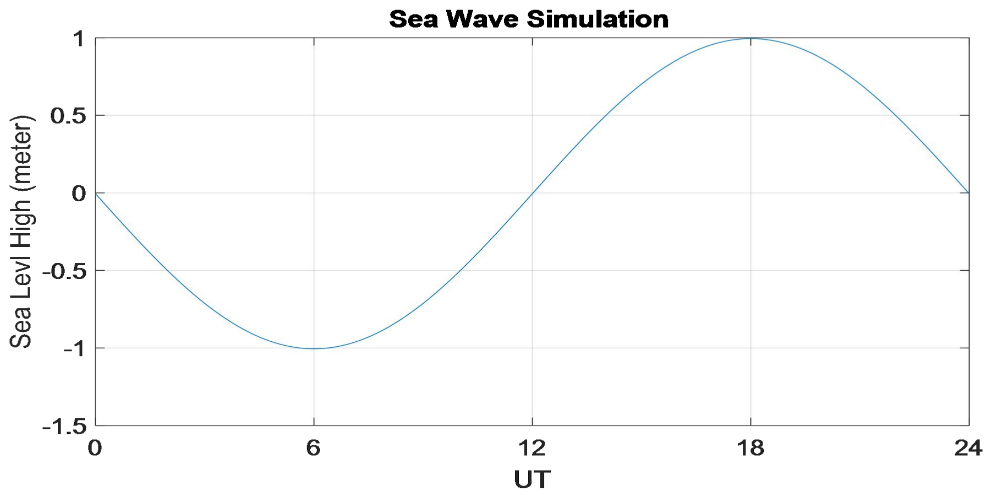

Figure 4. Simulation of sea waves

The sea waves shown in Figure 4 make the reflected signal pass through a distance which is proportional to the fluctuation of the sea wave height. Moreover, the total distance of the GPS signal reflected by the sea from the satellite to the reflected signal receiver is identical to the distance of the GPS satellite signal to the shadow rover receiver as shown in Figure 2. Therefore, the shadow receiver also seems to move periodically like sea waves but with twice the amplitude and at twice the distance for the actual reflected signal receiver above sea level. This means the rover receiver position is at the same latitude and longitude with the master receiver but at the height, as formulated in equation (9), which is shown in Figure 5.

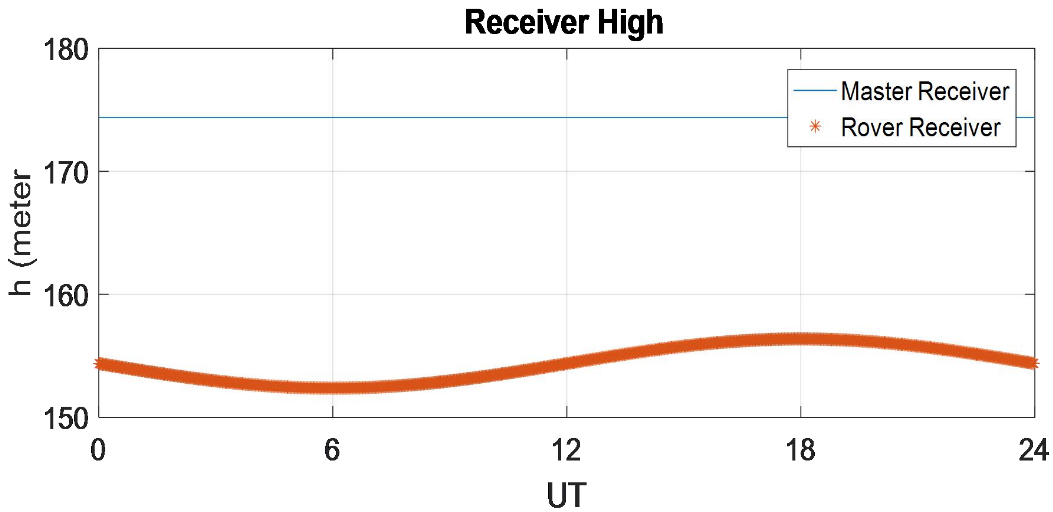

Figure 5. The height of the JOG2 master receiver is shown in the top graph while the shadow rover receiver is presented at the bottom graph in the simulation of signal reflection from GPS satellite No. 9 received just below the master receiver after experiencing reflections by sea level.

The geometry distance between the two receivers to the GPS satellite from their coordinates can be calculated using equations (10) and (11). Subsequently, it is possible to simulate the observation distance for the GPS satellites to the rover receiver with the code distance data received by the master receiver as shown in Figure 6 by multiplying it with the comparison of the geometric distance between the receivers using equation (12) and the results for satellite number 9 shown in Figure 7.

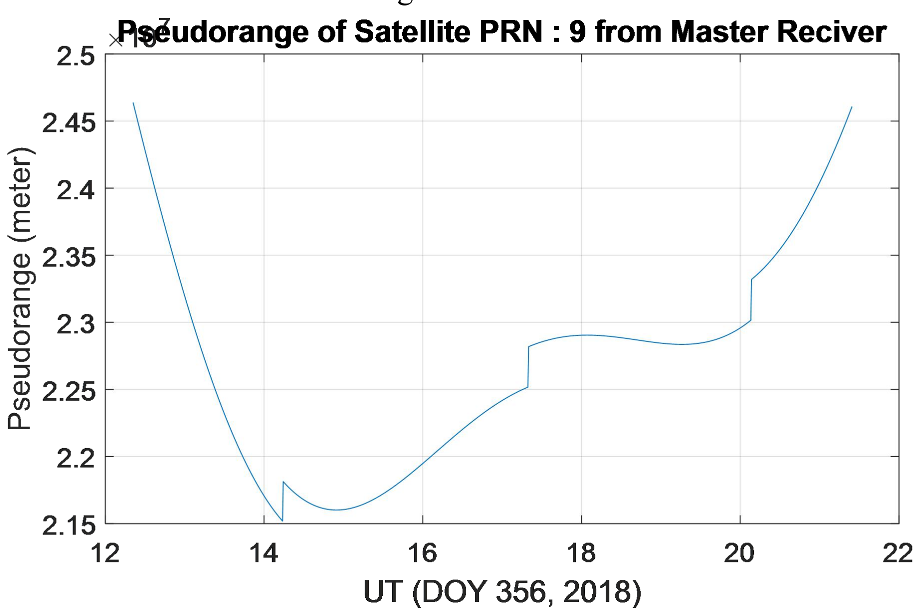

Figure 6. Satellite distance No 9 to Master Receiver

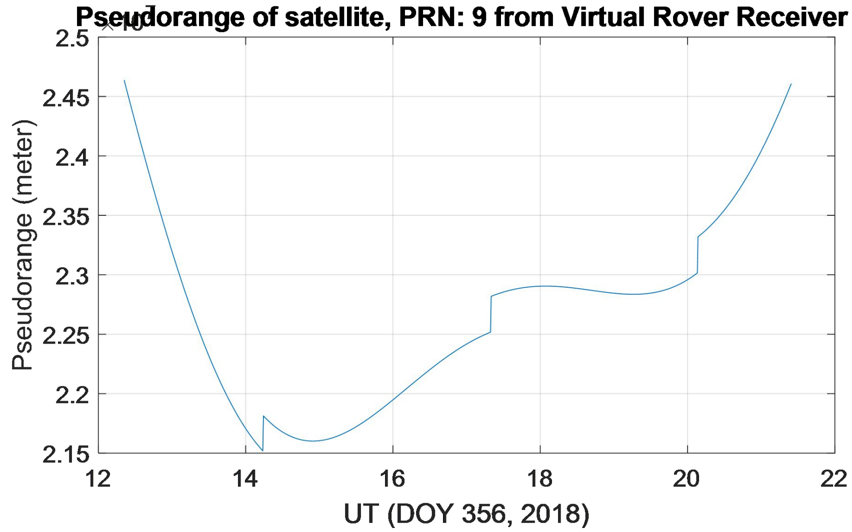

Figure 7. Pseudo Distance of Satellite No 9 to Virtual Rover Receiver

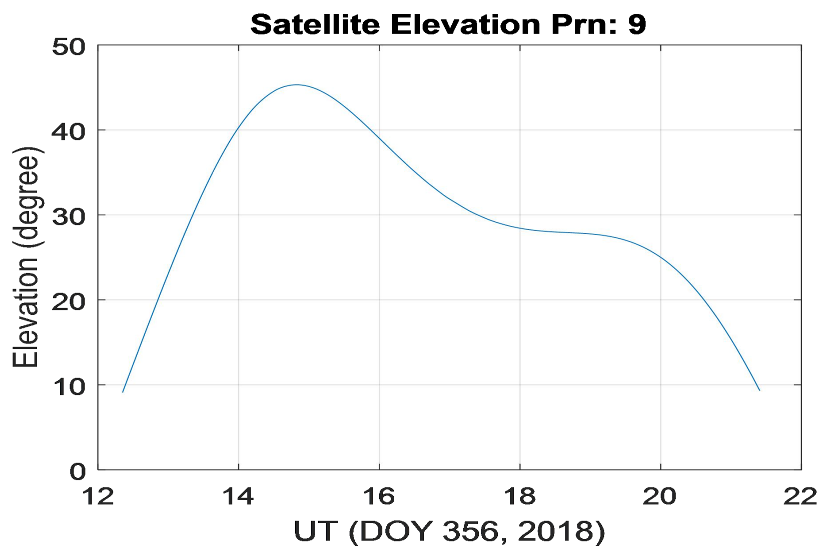

Figure 8. Elevation Satellite No 9

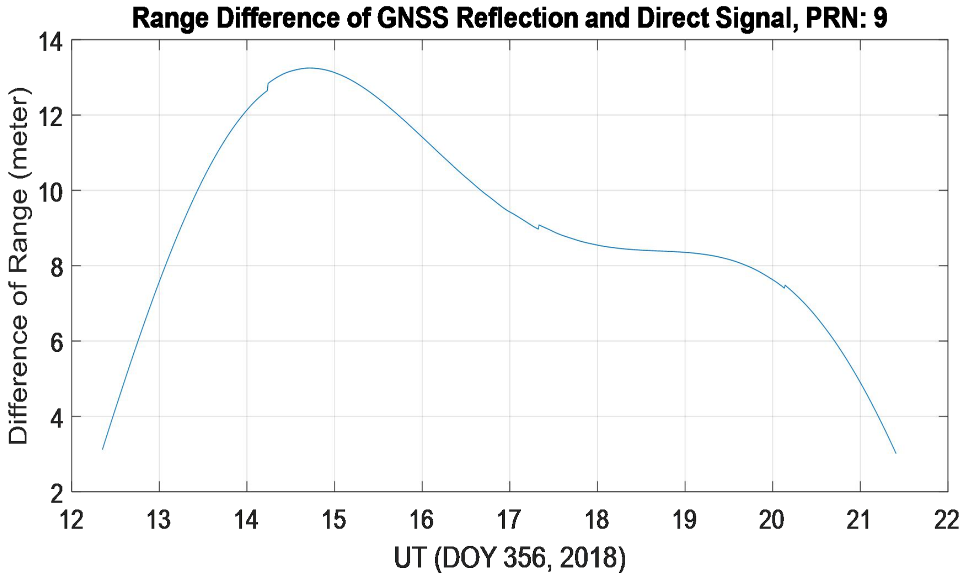

Figure 9. The difference in the observation distance of reflected and direct signals

Figure 9 shows the difference in the observation distance for the reflected and direct signals increased in between UT 12 to 15 with the mileage height almost close to 14 and, subsequently, decreased after experiencing stable conditions between 18 and 19. This is consistent with the elevation angle shown in Figure 8.

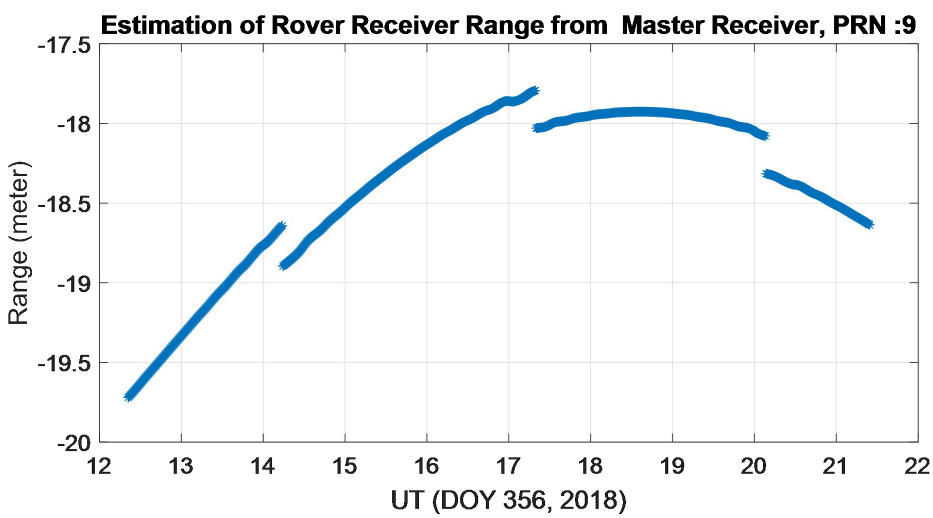

Figure 10. Estimated distance of rover receiver (shadow) from master receiver

Figure 10 shows the estimated distance of the rover receiver or shadow from the master receiver using equation (13) increased in between UT 12 and 19 and, subsequently, decreased at 19 to 22. The distance is negative and this means the rover is positioned under the master.

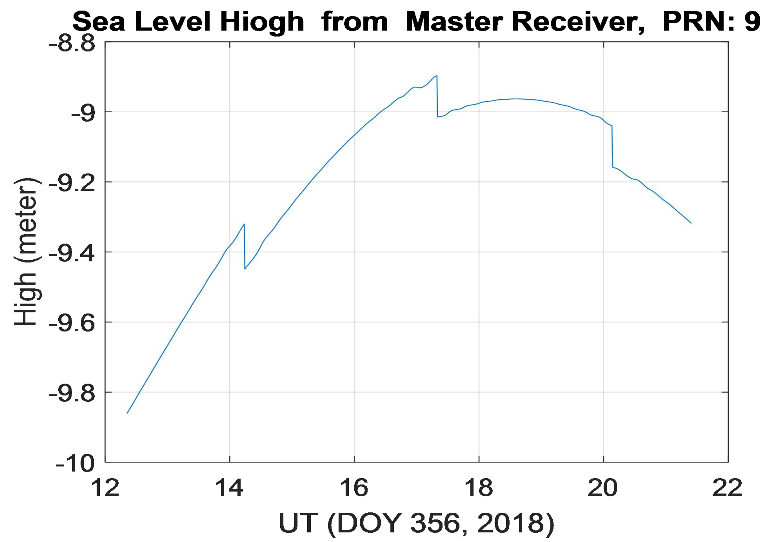

Figure 11. Height of sea level from the master receiver

Figure 11 shows the height of the sea level from the master receiver increased between 12 to 18 and later decreased.

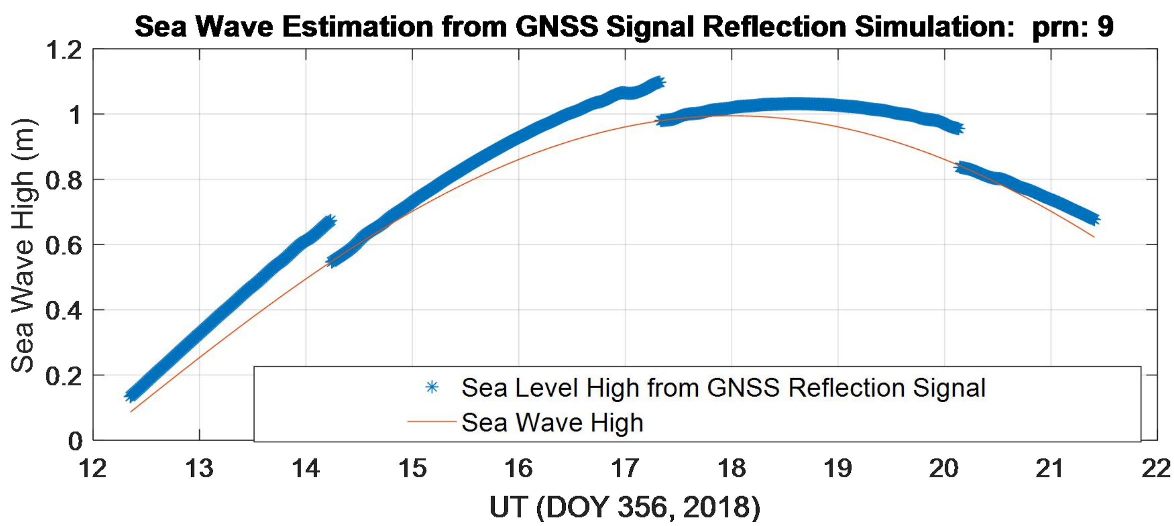

Figure 12. Simulation of determining sea wave height with GNSS

The sea wave height was estimated using equation (16) as shown in Figure 12 and the comparison with the simulated value was also recorded.

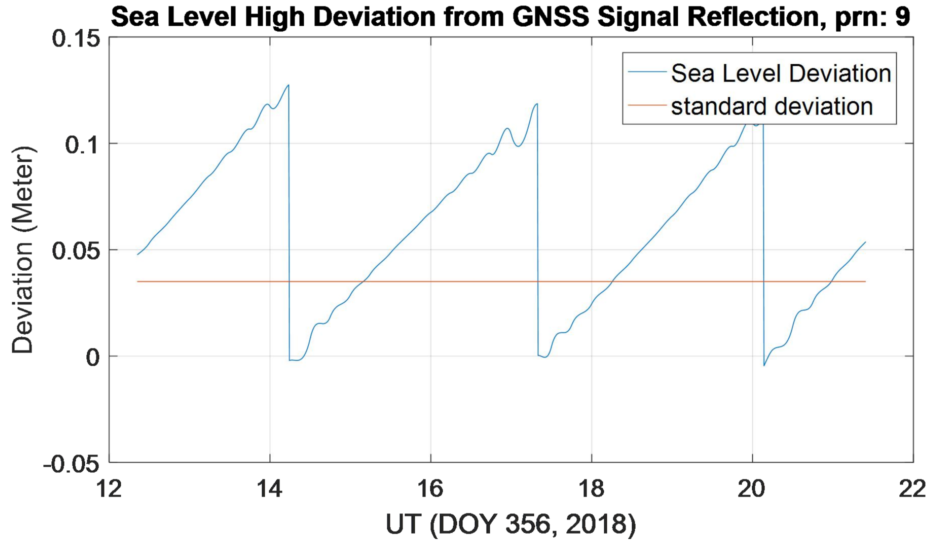

Figure 13. Deviation of sea wave height from a GNSS signal

Figure 13 shows the relative and standard deviations of sea wave height estimated from simulating the wave height in the reflection and direct data of GPS signal on satellite no. 9.

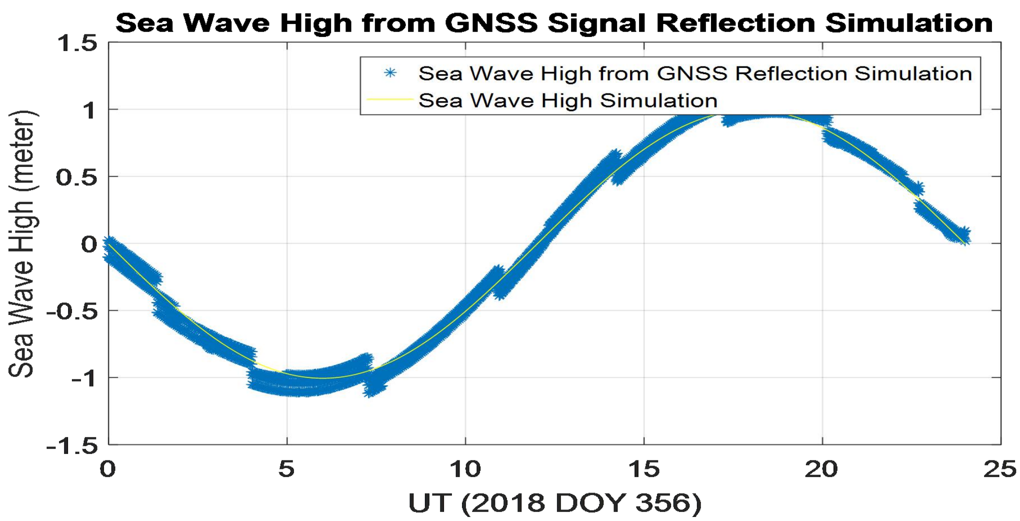

Figure 14. Wave height from the simulation of GNSS JOG2 signal reflection

All the GPS signal reflections observed to estimate the sea wave height were combined to generated a value for 24 hours as shown in Figure 14.

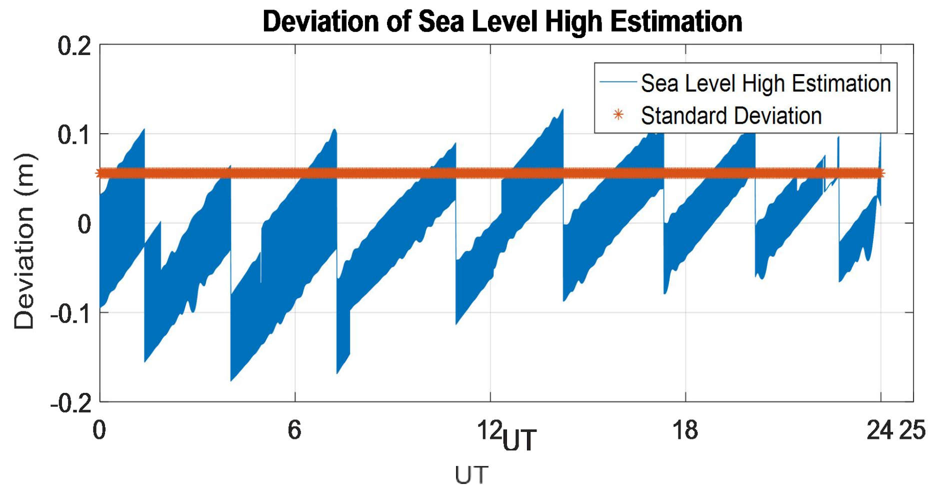

Figure 15. Deviation of estimated sea wave height from P1 code distance data

The relative deviation of the estimated sea wave heights shown in Figure 15 was 0.17 meters while the standard deviation was estimated at 0.056 meters. Therefore, based on simulations, the code distance of GPS signal reflections is suitable to monitor sea wave heights and tsunamis.

4.CONCLUSIONS

The simulations of GNSS signal reflection showed the possibility of using the pseudo distance from the GPS code data to determine sea level height with an accuracy of a few centimeters and this means it is feasible to be used in tidal and tsunami monitoring. The process, however, requires the two receivers are identical with the same length and type of antennas in order to ignore the bias using a single differential on the same satellite received on the receivers.

Acknowledgment

This research was funded through the INSINAS program of the Indonesian Ministry of research technology and higher education with contract No. 14/INS-1/PPK/E4/2020 which has been amended to be No. 70/iNS-1/PPK/E4/2020. And we gratefully thank the Indonesian Geospatial information agency for support in the preparation GNSS real time data. Also, Well deserved recognition is due to Joni Efendi for his consultations and suggestions for using GNSS RTCM data for real time TEC purposes.

REFERENCES

Artru J, Ducic V, Kanamori H, Lognonné P and Murakami M (2005), Ionospheric detection of gravity waves induced by tsunamis, Geophys. J. Int, 160 840-48.

Chen, C., C., Gao, S., and Maqsoos, M. (2012). Antennas for Global Navigation Satellite System Receivers. 10.1002.

Garrison, J.L.; Katzberg, S.J.; Hill, M.I. Effect of sea roughness on bistatically scattered range coded signals from the Global Positioning System. Geophys. Res. Lett. 1998, 25, 2257–2260. [CrossRef].

Harijono, S.W.B., Harjadi, P.,Fauzi . (2010). InaTEWS (Indonesia Tsunami Early Warning System) : Konsep dan Implementasi. Badan Meteorologi Klimatologi dan Geofisika (BMKG).

Jin, S.; Cardellach, E.; Xie, F. GNSS Remote Sensing: Theory, Methods and Applications; Springer: Dordrecht, The Netherlands, 2014; p. 276.

Lofgren, J.,S., and Haas, R (2014). Sea level measurements using multi-frequency GPS and GLONASS observations. EURASIP *Journal on Advances in Signal Processing*, 2014 50.

Martin-Neira, M. A passive reflectometry and interferometry system (PARIS): Application to ocean altimetry. ESA J. 1993, 17, 331–355.

Muslim, B., Kumalasari, C, J., Chiuman, N., and Arafah, M, I, F, (2019). Study of GNSS reflection application for monitoring of sea water level. Komunikasi Fisika Indonesia.

Peltier ,W.R. & Hines, C.O., 1976. On the possible detection of tsunamis by a monitoring of the ionosphere, J. geophys. Res., 81(12), 1995–2000.

R. H. Stewart, "Introduction To Physical Oceanography," *Am. J. Phys*., 2008.

Rudenko, S., Esselborn, S., Schone, T., and Dettmering, D (2019). Impact of terrestrial reference frame realizations on altimetry satellite orbit quality and global and regional sea level trends: a switch from ITRF2008 to ITRF2014. Solid Earth, 10, 293-305.

Semmling, A. M; Schmidt, T ; Wickert, J, dkk, 'On the retrieval of the specular reflection in GNSS carrier observations for ocean altimetry', Radio Science, Vol:47, RS6007, doi:10.1029/2012RS005007, 2012.

Zavorotny, V.U.; Gleason, S.; Cardellach, E.; Camps, A. Tutorial on remote sensing using GNSS bistatic radar of opportunity. IEEE Geosci. Remote Sens. Mag. 2014, 2, 8–45. [CrossRef].

ISSN 8755-6839

SCIENCE OF TSUNAMI HAZARDS

Journal of Tsunami Society International

Volume 39 Number 4 2020

NUMERICAL SIMULATION OF EARTHQUAKES AND TSUNAMIS IN MEXICO – Case Study: Earthquake and Tsunami of 8 September 2018

Raissa Mazova [1,2], Sergey Tyuntyayev [3], Adel Giniyatullin[1], Yury Orlov[1], Evgeny Orlov[1], Vladimir Mel'nikov[1]

[1]Nizhny Novgorod State Technical University n.a. R.E. Alekseev, 603600 Nizhny Novgorod, Russian Federation
[2]Moscow Institute of Physics and Technology (MIPT) 141701 Moscow, Russian Federation ,e-mail: raissamazova@yandex.ru
[3]Harman Connected Services (HCS), Nizhny Novgorod, Russian Federation; e-mail: ser.tyuntyaev@gmail.com

ABSTRACT

The present study pertains to a catastrophic earthquake with a magnitude of M = 8.1, which occurred in the southern region of Mexico on September 8, 2018. Taking into account the location of the earthquake source and its hypocenter, a numerical simulation of the generation of a seismic source of tsunami waves and their propagation over the water area for two different mechanisms of the seismic source, with their different localizations, was carried out. Two-block and four-block earthquake sources are considered and the obtained wave characteristics are compared with field data and data of other authors.

Keywords: *source of earthquake, tsunami waves, numerical modeling.*

1. INTRODUCTION

As predicted earlier by a number of authors (see, e.g., [1]), seismic activity along the perimeter of the Pacific Ocean should increase significantly by the end of the 20th and the beginning of the 21st centuries. The appearance of large earthquakes and associated tsunamis in the Pacific and Indian Oceans, at the beginning of this century, supports this assumption. The importance of this assumption leads to the need for a deeper analysis of historical data on catastrophic tsunamigenic earthquakes in specific ocean regions in order to reduce the tsunami hazard for coastal areas.

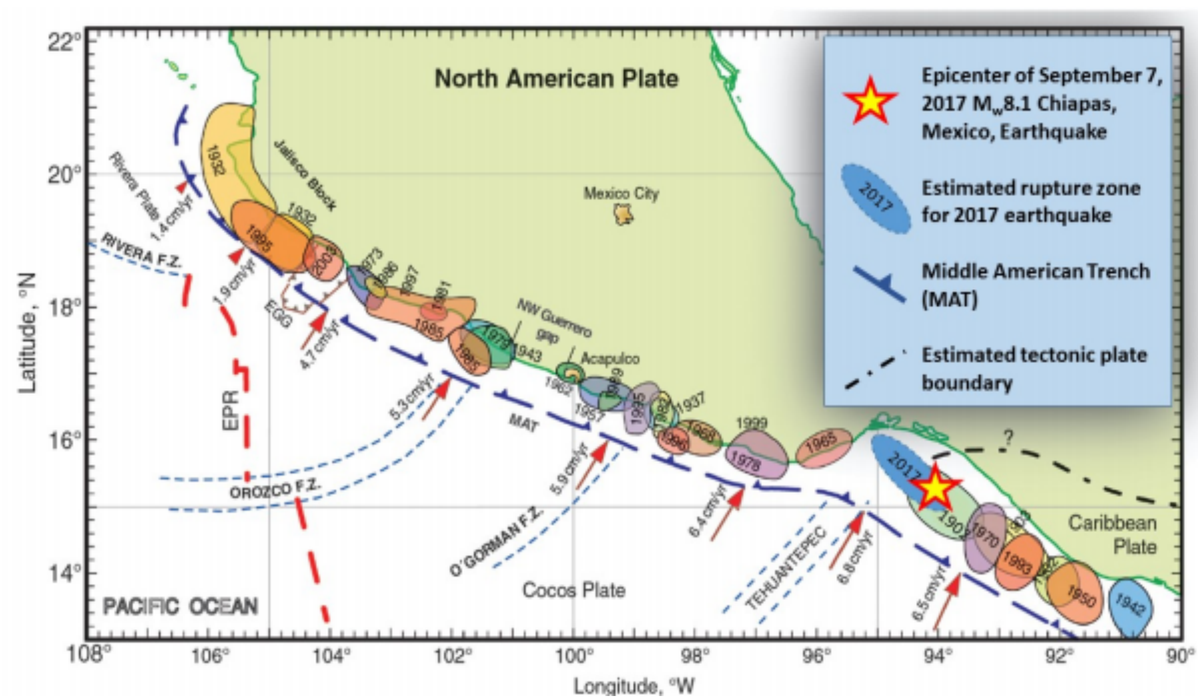

Fig.1. Historic Earthquakes in the Pacific Coastal Region of Mexico [2-3]

For example, it is well known that some of the largest earthquakes that occurred on the Guerrero coast (see Fig. 1), and located parallel to the active Mexican subduction zone, generated tsunamis. The occurrence of such historic earthquakes and tsunamis in this region has been relatively well documented since the 16th century. For example, during the last century, large earthquakes occurred near the Pacific coast of Mexico, such as in Jalisco in 1932 (M = 8.2), in Colima in 1995 (M = 8.0), and the earthquake in Mihoatskune in 1985 (M = 8.1), which devastated the coast of Mexico City, resulting in large human and economic losses, estimated in billions of dollars. Nevertheless, information about the geological evidence of earthquakes and a detailed description of the tsunami caused by them is practically not documented [2].

2. **THE 8 SEPTEMBER 2017 EARTHQUAKE IN MEXICO**

At the location of this event, the Cocos Plate converges with the North American Plate (see Fig. 2) at a rate of approximately 76 mm / yr, in a northeasterly direction. The Cocos Plate begins its subduction in Central America, 100 km southwest of this earthquake. Location, depth and mechanism of formation of faults of this earthquake indicates that the event is intraplate [3,4]. This earthquake is one of the largest ever recorded on the southern coast of Mexico. The tsunami wave following the earthquake caused significant damage and dozens of deaths. In the state of Oaxaco 45 people died, in the state of Chiapas 12 people and in the state of Tabasco 4 people, schools and hospitals were also de-energized. [5]

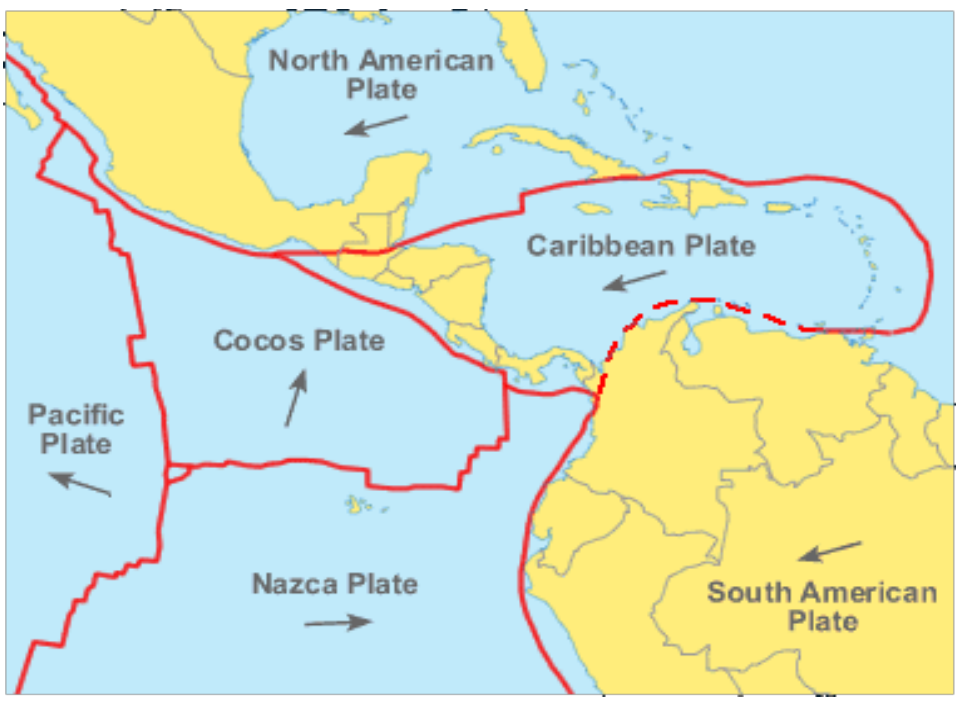

Fig. 2. The fault pattern (red lines) in the region of Central America. Black arrows indicate the direction of movement of the continental plates [5, 15]

3. STATEMENT OF THE PROBLEM

The location of the source for the numerical simulation of the considered earthquake was chosen based on the location of the hypocenter and processing of data from the NEIC information center [4, 5, 15, 16]. In Fig.3, the position of the seismic source on the map is shown, where the localization of aftershocks is marked with black dots.

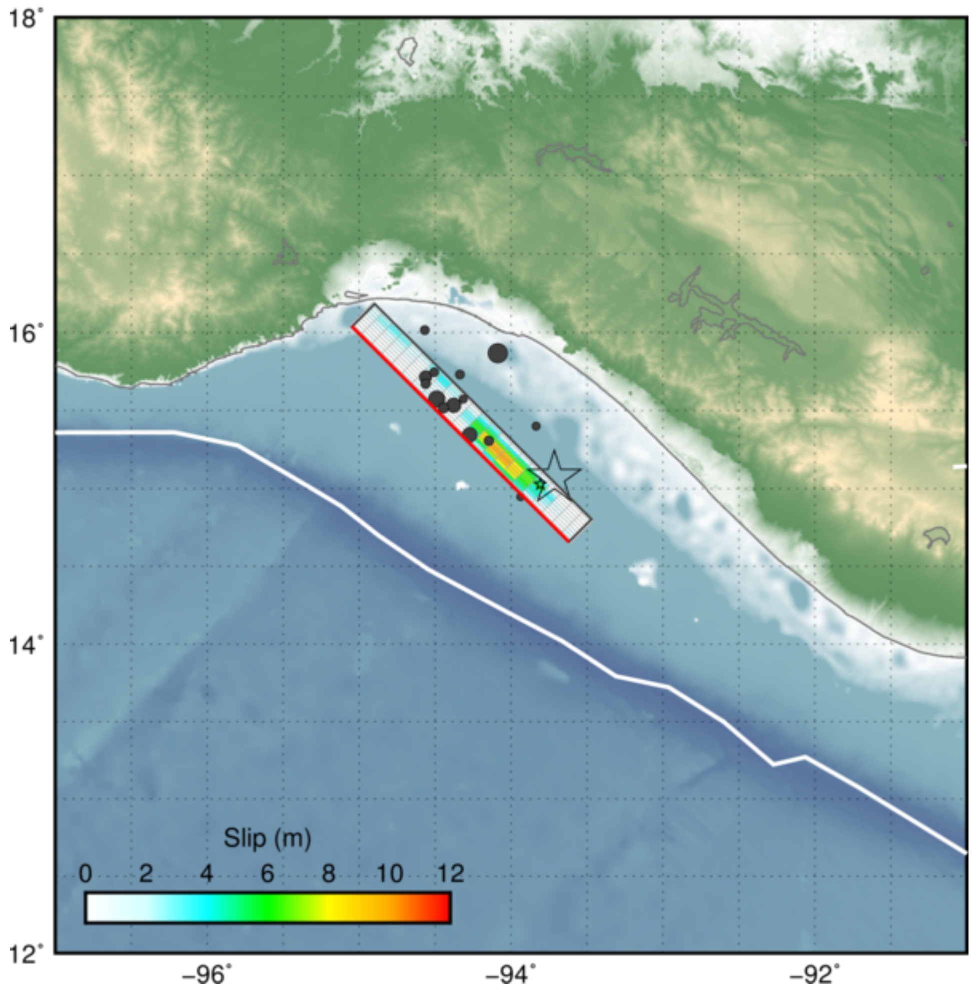

Fig. 3. Position of the seismic source on the map. The black dots mark the location of aftershocks [4]

Using the data given in [4, 5, 15, 16] and the results of [2-3], on the basis of the keyblock model of the earthquake source [6, 9], two possible scenarios for the realization of the Earth's crust movements in the region of the seismic source for this earthquake were considered:

In the first Scenario, a two-block source is considered, divided lengthwise into two longitudinal blocks. The implementation of the movement of blocks in the seismic source occurs in 35 seconds (Table 1). The first block, oriented towards the shore, moves down 3 meters within 20 seconds, the second block, oriented towards the open ocean, it rises 6 meters in 20 seconds, and its movement begins 15 seconds later than the movement of the first block. Fig.4 shows the location of the seismic source on the bathymetric map.

For the second Scenario, a kinematic model of a seismic source consisting of four blocks was used. The division into blocks during the selection of the seismic source was carried out according to the intensity and location of aftershocks (Fig.3, Fig.5). The implementation of the movement of blocks in the seismic source occurs in 30 seconds (Table 1).

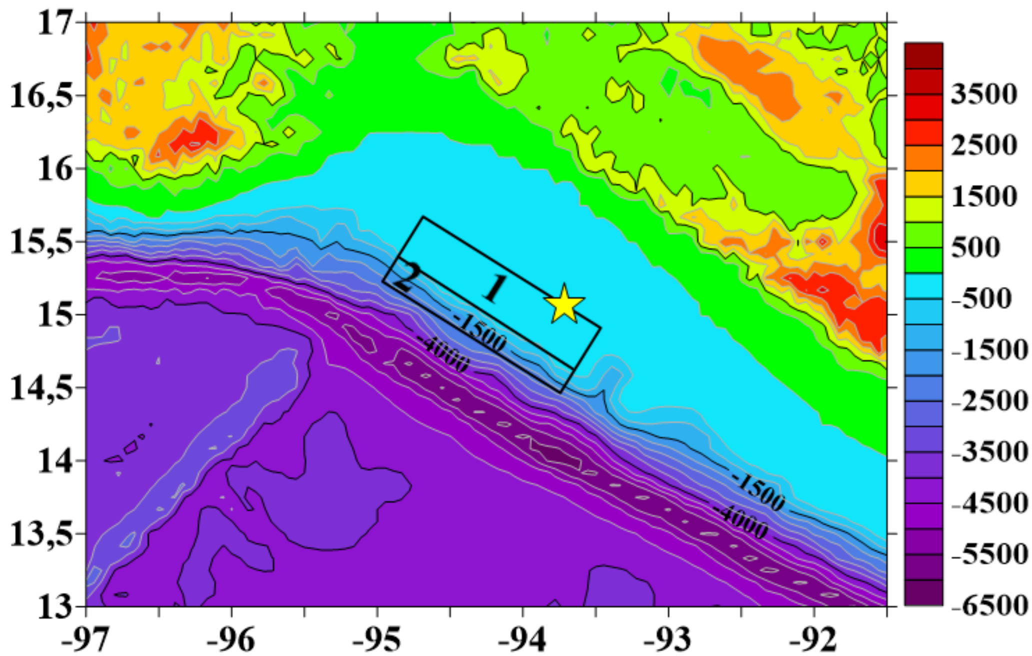

Fig. 4 Position of seismic source on Bathymetric map for Scenario 1.

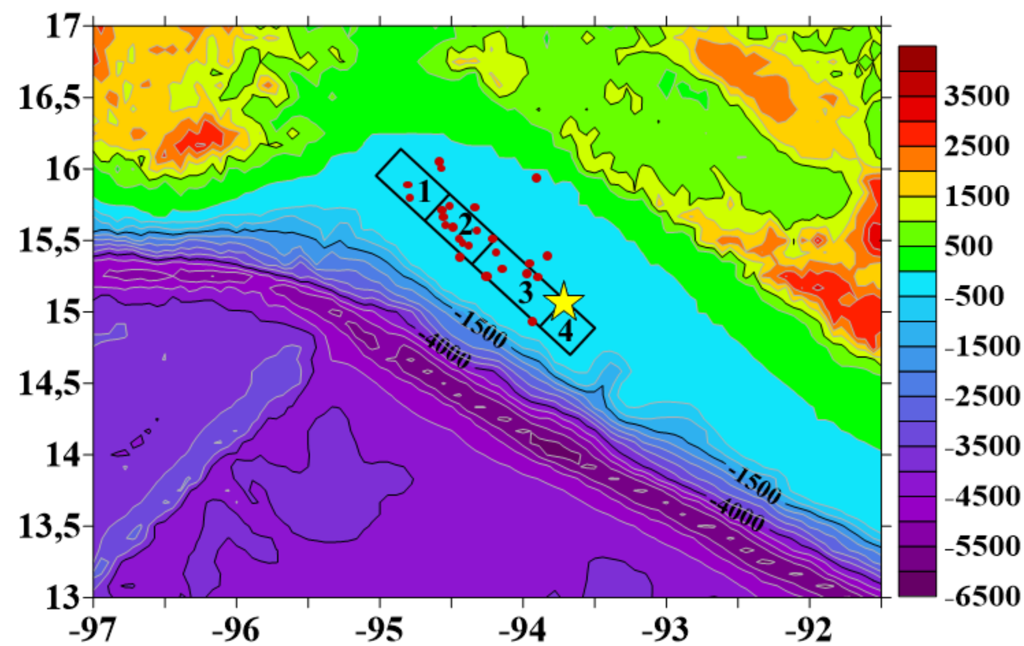

Fig. 5. Position of seismic source on bathymetric map for Scenario 2

The considered movements of the key blocks in the earthquake source for these two possible scenarios are given in Table 1.

Table 1. The movement of blocks in the earthquake source for Scenario 1 and 2

	Scenario 1		Scenario 2			
	Block №					
	1	2	1	2	3	4
Start of uplift (s)	**0**	**15**	**10**	**5**	**0**	**10**
Time of uplift (s)	**20**	**20**	**10**	**15**	**20**	**10**
Height of uplift (m)	**-3**	**6**	**-0.5**	**2**	**6**	**0.5**

4. MATHEMATICAL STATEMENT OF THE PROBLEM.

In this paper, we study long surface waves with lengths and periods characteristic of tsunamis. The non-linear system of shallow water equations [7-11] is used to describe the process of wave generation and propagation in accordance with the assumptions that were mentioned above.

$$\begin{cases} \vec{U}_t + \vec{U} \cdot grad\ \vec{U} + g \cdot grad\,\eta = 0 \\ \eta_t + div\left((H + \eta - B)\vec{U}\right) = B_t \end{cases} \qquad \vec{U} = \begin{pmatrix} u \\ v \end{pmatrix} \qquad (1)$$

Here the functions u and v are the velocities of water particles; g - acceleration due to gravity, $B(x,y,t)$ - function describing the law of motion of the bottom of the basinl; for a keyboard model, the function $B(x,y,t)$ describes the sequential movement of the key blocks.

The mechanism of realization of the movements of the Earth's crust in the seismic source was given from tectonic considerations using the WELLS formulas [12].

$$\begin{aligned} \lg L &= 0{,}59M - 2{,}44 \pm 0{,}16 \\ \lg W &= 0{,}32M - 1{,}01 \pm 0{,}15 \end{aligned} \quad , \qquad (2)$$

where M is the magnitude of the earthquake; L is the length of the rupture in the source (in km), W is the width of the rupture plane (in km). For this earthquake source, the parameters obtained are as follows: the source length will be 233 ± 82, and the source width will be 40 ± 14.

Using the Iida formula (3) (see, e.g., [8]), for a given earthquake with a magnitude of $M = 8.1$, the vertical component of the displacement of the water surface above the earthquake source can be obtained using the formula

$$\lg(H/2) = 0{,}8M - 5{,}6 \tag{3}$$

where M is the magnitude of the earthquake, and H is the maximum height of the vertical displacement of the bottom at the source of the earthquake. The values obtained by formulas (1) and (2) were used to simulate the generation of the tsunami source in scenarios 1 and 2.

Scenario 1. Let us consider the results of numerical simulation of scenario 1. For Scenario 1, an earthquake source is selected, consisting of two blocks, located along the coastline, and the block oriented towards the coast (block 1) has a negative shift (see Table 1). The entire process of tsunami source generation (water displacement on the surface of the water area above the earthquake source) during the movement of blocks takes 35 s. Fig.6 shows three time moments during the generation of the tsunami source. By the corresponding displacement of the wave surface, one can determine the downward movement of the first block (Fig. 6, left panel), then at 20 s, the rise of the second block by approximately 1.4 m (Fig. 6, middle panel) and at the 35th s the generation of the tsunami source ended (Fig.6, right panel).

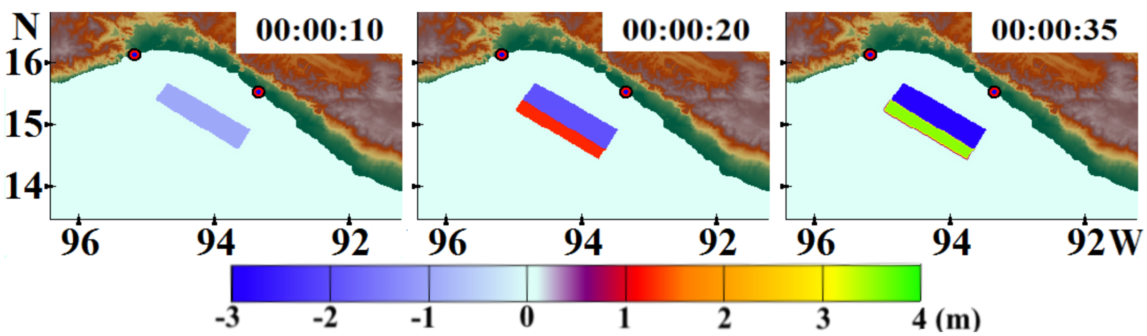

Fig. 6. Generation of the tsunami source for Scenario 1: a) 10s; b) 20 s; c) 35 s.

In Fig. 7 the position of the wave fronts when implemented in the considered water area is presented. It is clearly seen that at 23 min (Fig. 7, upper left panel), the elevation waves with a height of 0.2-0.5 m approach the cities of Mexico, Salina Cruz and Puerto Escondido. At the 33rd min (Fig.7, upper right panel), both points have already attacked by the first wave, and also the eastern front with an elevation with a height of 0.1-0.3 m approaches the city of Champerico (Guatemala). With a further spread to 48 minutes (Fig. 7, lower left panel), the western front continues to cover the southeast of Mexico, approaching the city of Acapulco with a height of up to 0.2 m, and the eastern front reaches El Salvador with a height of up to 0.1 m, namely to the city of Akahutla. After 1 hour and 20 min (Fig.7, lower left panel), the waves reached all near-field points, and also approach the cities of Lazaro Cardenas and Tamarindo with heights of up to 0.1 m.

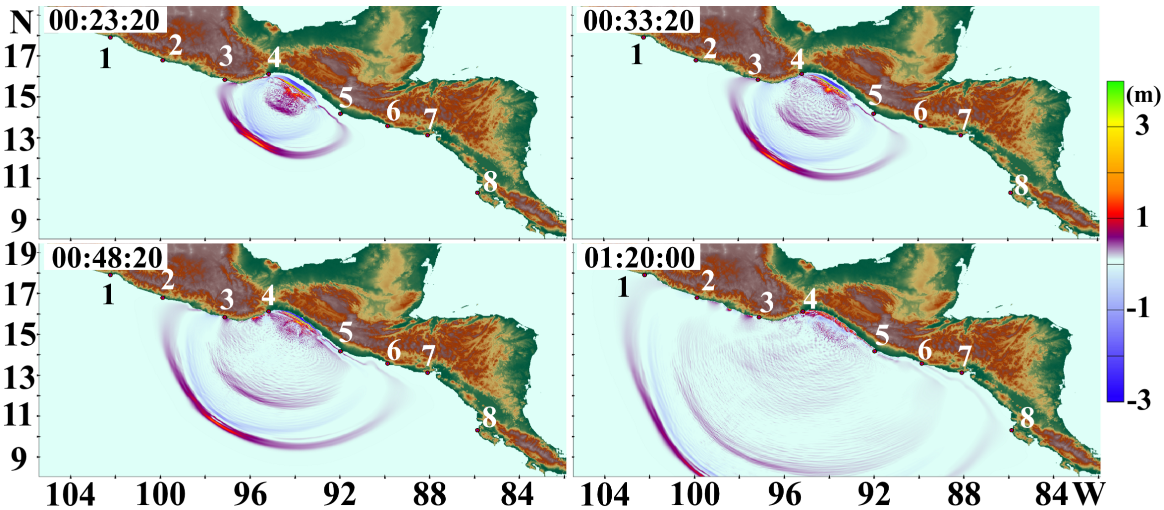

Fig.7. Position of wave fronts in numerical simulation for Scenario 1 for 4 time points: 1. Lazaro Cardenas (Mexico); 2. Acapulco (Mexico); 3. Puerto Escondido (Mexico); 4. Salina Cruz (Mexico); 5. Champerico (Guatemala); 6. Acajutla (Salvador); 7. El Cuco (Salvador); 8. Tamarindo (Costa Rica)

In Fig.8, the maximum distribution of wave heights over the entire calculated area is presented. The distribution of the maximum wave heights clearly shows that the most dangerous areas are near-field points, namely the cities: Salina Cruz (Mexico), (item 4), Puerto Escondido (Mexico), (item 3) and Champerico (Guatemala), (p.5).

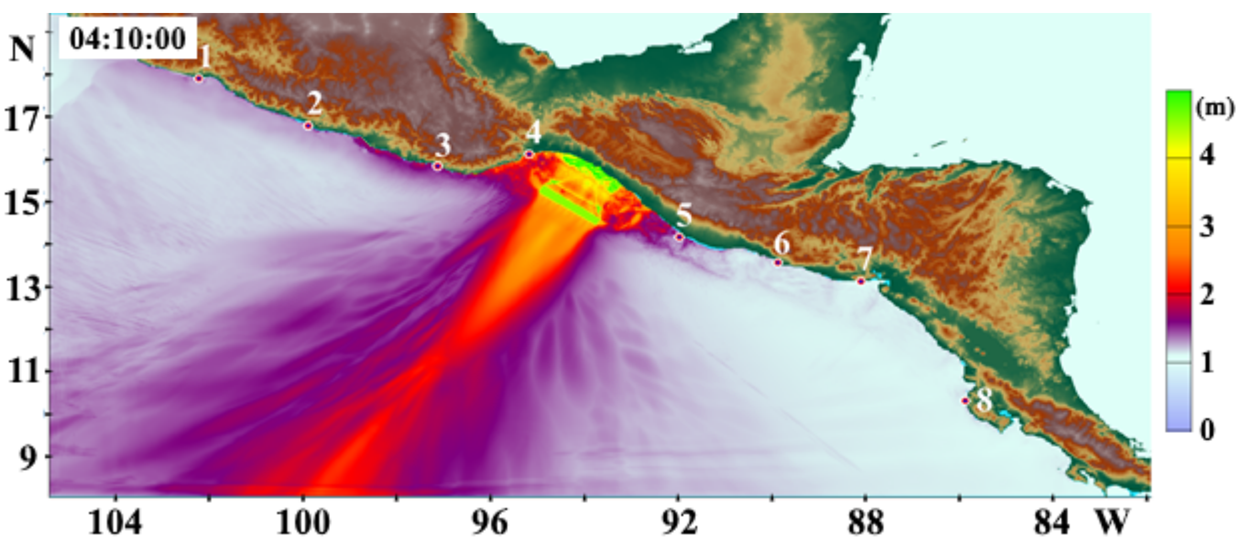

Fig. 8. The distribution of maximum wave heights in the water area when implementing Scenario 1: 1. Lazaro Cardenas (Mexico); 2. Acapulco (Mexico); 3. Puerto Escondido (Mexico); 4. Salina Cruz (Mexico); 5. Champerico (Guatemala); 6. Acajutla (Salvador); 7. El Cuco (Salvador); 8. Tamarindo (Costa Rica).

A more detailed distribution of the maximum tsunami wave heights along the coasts can be seen on the 3D histograms of the maximum wave heights plotted on the 5-meter isobath shown in Fig. 9. It is clearly seen that on the Mexican coast near the cities of Puerto Escondido and Acapulco (Fig.9a), the wave heights change in the region from 0.1 to 1 m. You can also notice that the most dangerous coast is the south the eastern coast of Mexico near the city of Salina Cruz (Fig. 9c), where the maximum wave height reaches 1.5 m. On the coast of Guatemala (Fig. 9b), the maximum wave height reaches 1.3 m, and in the area of the city of Champerico, the heights vary from 0.1 to 0.3 m.

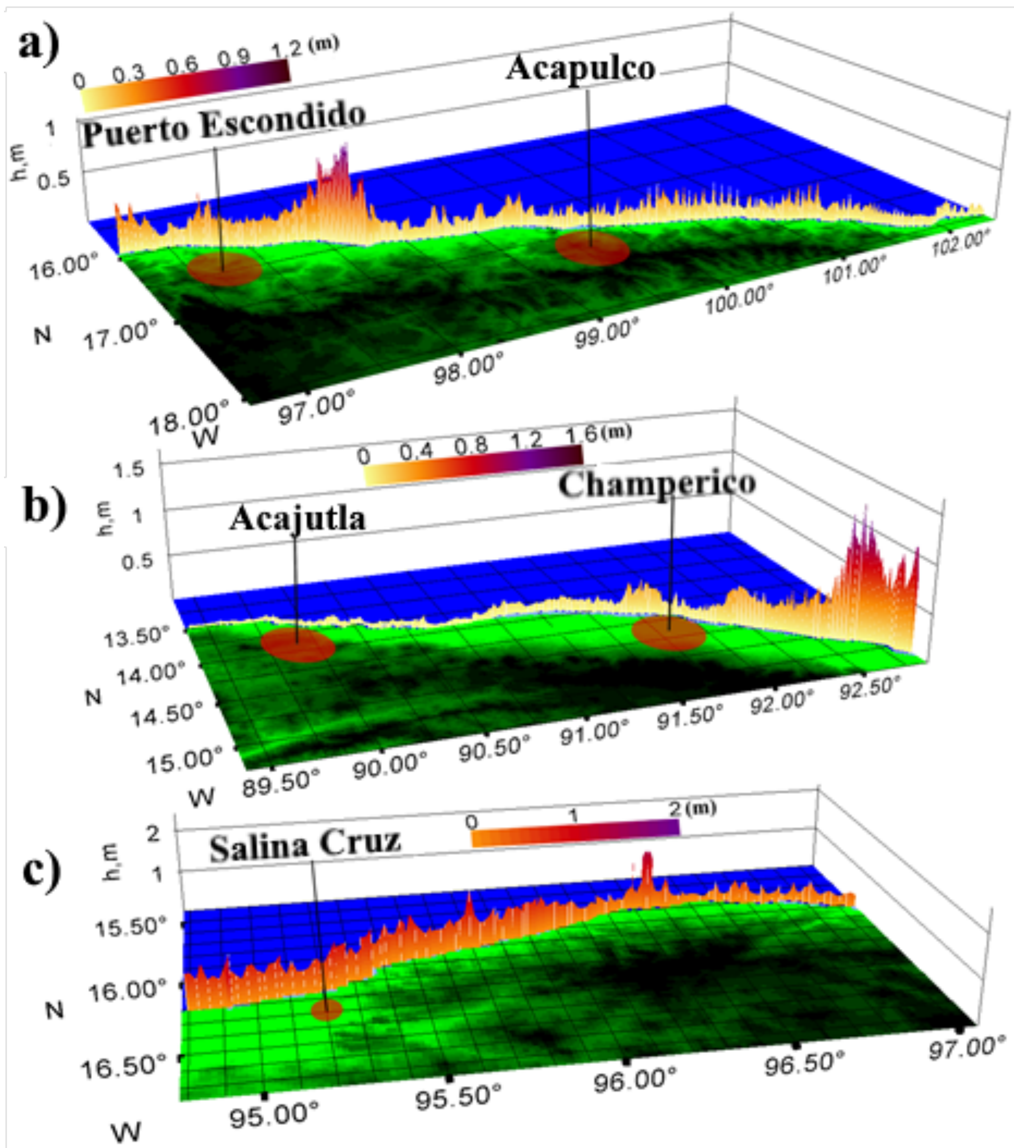

Fig. 9. Two-dimensional histograms for maximum wave heights on a 5-meter isobath when implementing scenario 1: a) Mexico; b) Guatemala, El Salvador; c) Salina Cruz (Mexico)

But the coast of El Salvador near the city of Akahutla is less dangerous compared to neighboring Guatemala, and the maximum wave heights reach up to 0.1. Data from virtual tide gauges, namely the maximum wave height, the largest decrease in the water level and the time of wave arrival to points, are given in Table 2.

Table 2. Data of virtual tide gauges for Scenario 1.

City name	Maximum wave height at 5m isobath (m)	Strongest water level depression at 5m isobath m)	Time of approaching the point
01. Lazaro Cardenas (Mexico)	0.24	-0.29	01:22:55
02. Acapulco (Mexico)	0.3	-0.3	00:52:55
03. Puerto Escondido (Mexico)	0.51	-0.96	00:25:00
04. Salina Cruz (Mexico)	1.35	-1.8	00:01:15
05. Champerico (Guatemala)	0.39	-0.36	00:38:45
06. Acajutla (Salvador)	0.24	-0.38	01:11:15
07. El Cuco (Salvador)	0.15	-0.14	01:42:55
08. Tamarindo (Costa Rica)	0.19	-0.26	01:26:15

5. RESULTS OF NUMERICAL SIMULATION FOR SCENARIO 2

The division into blocks during the implementation of the scenario under consideration was carried out according to the intensity and location of aftershocks (see Fig. 3, 5). Fig. 5 shows the position of the seismic source on the bathymetric map, divided into 4 blocks. The movement of the source starts from the 3rd block to a height of 6m in 20 s, then 10 s after the start of the rise of block 3, block 2 begins to move up to a height of 3m for 15 s. Blocks 1 and 4 begin to move up from 15 s within 10 s to a height of 1 m (see Table 1). Figure 10 shows the generation of a tsunami source for scenario 2, when blocks move in the earthquake source shown in Table 1.

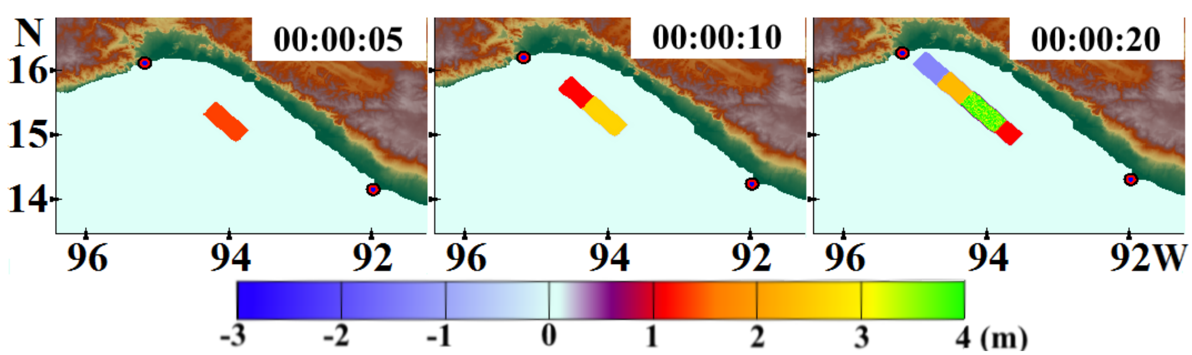

Fig. 10. Generation of the tsunami source in the implementation of Scenario 2

In Fig. 11 the position of the wave fronts in the numerical simulation of scenario 2 is presented. On the upper left panel, it is seen that the depression wave is approaching the city of Salina Cruz. Further, by the 35th min (Fig.11 (2)), the wave has already reached Salina Cruz, the western front with elevation approaches the Puerto Escondido and the eastern front approaches the coast of Guatemala. At the 55th min (Fig.11 (3)), the wave with elevation approaches Champerico Guatemala). With further propagation (1h 50m), the western front continues to cover the coast of Mexico, and is coming to the city of Acapulco, and the eastern front approaches the city of Akahutla (Fig. 11 (4)). After 1 hour 35 min from the beginning of the calculation (Fig.11 (5)), the wave covered most of the computed water area, so in the west, the wave reaches the city of Lazaro Cardenas, and in the east it approaches the cities of Tamarindo (Costa Rica) and El Cuco (Salvador). By 2h 2min (Fig. (11.6)), the wave covered the entire computed area.

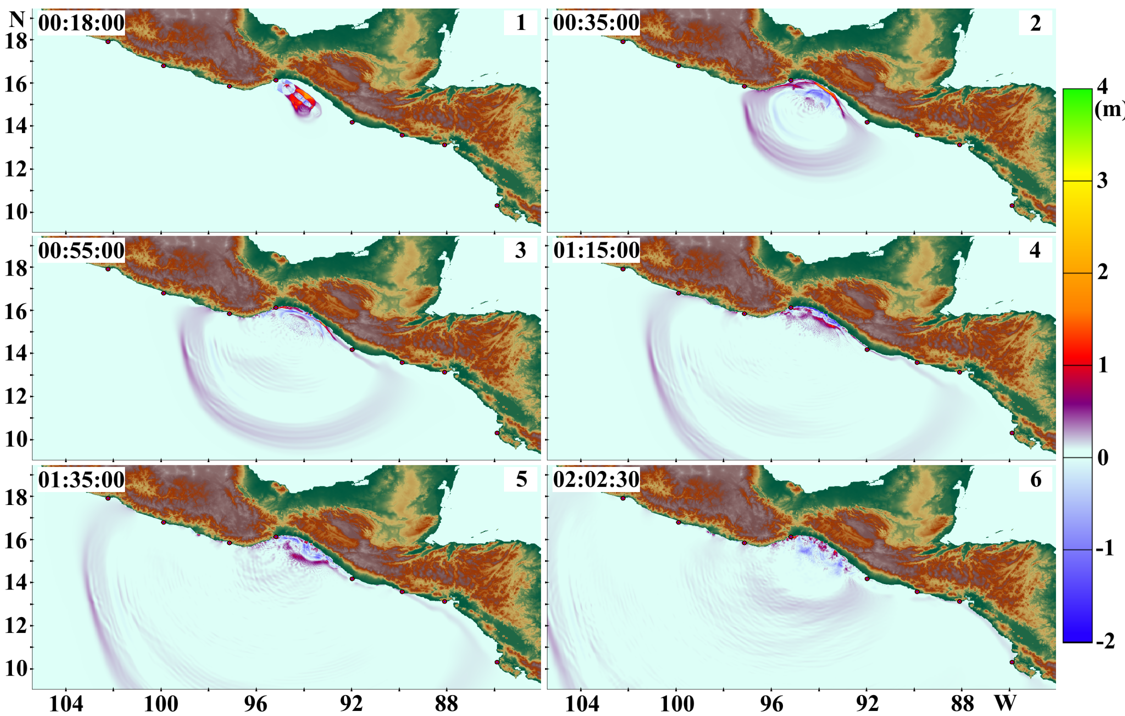

Fig. 11. Position of wave fronts in the numerical simulation of Scenario 2 for 6 time moments

Figure 12 shows the maximum distribution of wave heights. The distribution shows that the most dangerous areas are the cities: Salina Cruz (Mexico, p.4), Puerto Escondido (Mexico, p.3) and Champerico (Guatemalla, p.5).

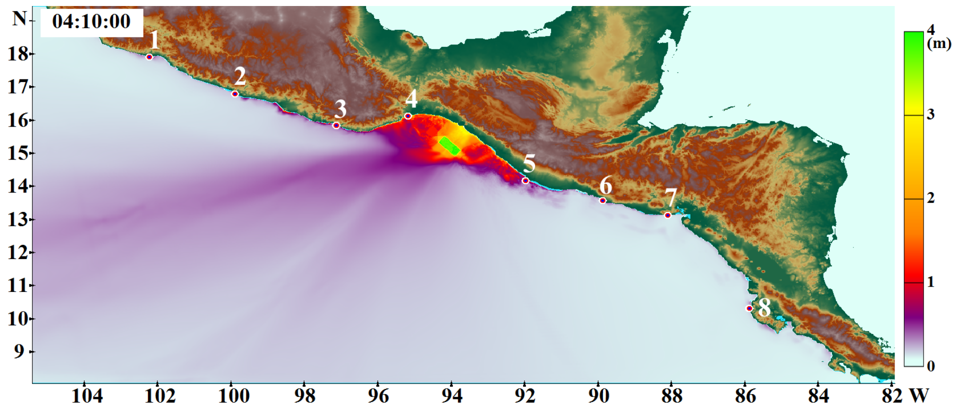

Fig. 12. The distribution of the maximum wave heights in the water area in the implementation of Scenario 2

A more detailed distribution of the maximum wave heights along a number of Pacific coasts can be seen in Fig.13, which shows two-dimensional histograms of the distribution of the maximum wave heights on the 5-meter isobath.

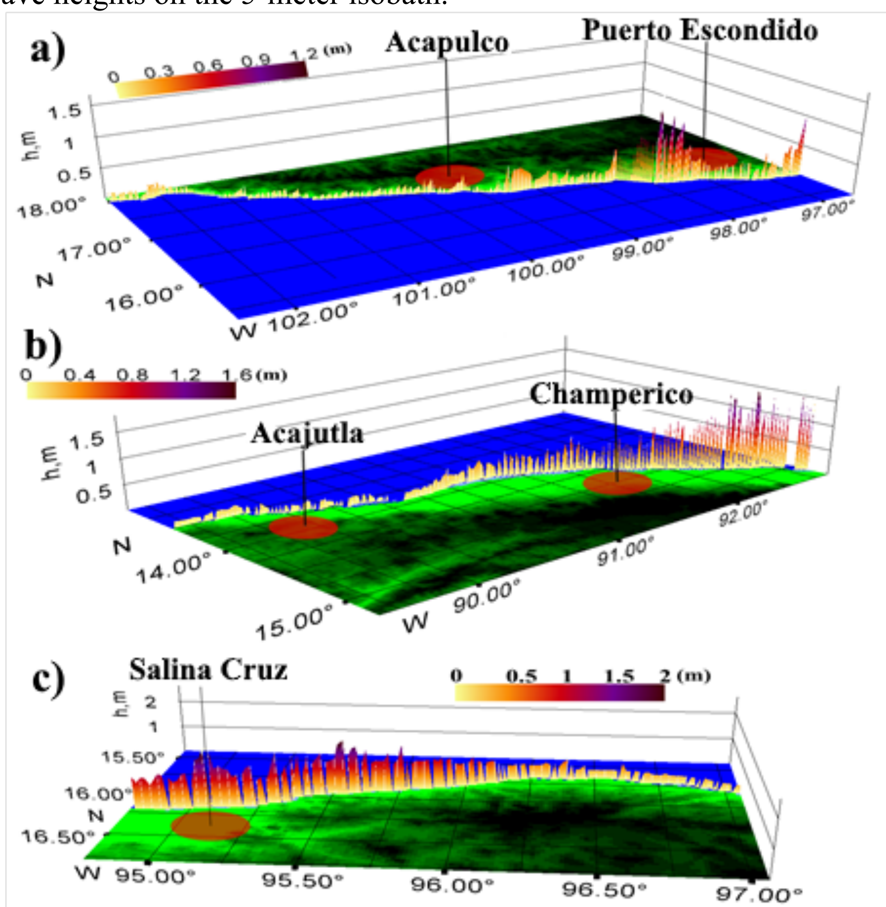

Fig. 13. Two-dimensional histograms for maximum wave heights on a 5-meter isobath in the implementation of Scenario 2 for the coasts: a) The coast of Mexico; b) The coast of Guatemala and El Salvador; c) Coast of Mexico near the city of Salina Cruz

It is clearly seen that on the coast of Mexico near the city of Acapulco the maximum wave height does not exceed 0.3 m, and on the coast near the city of Puerto Escondido the maximum wave height varies from 0.3 to 1 m (see. Fig.13 (a)). The maximum wave heights along the Guatemala and Salvador coasts (fig.13 (b)) decrease from west to east. Thus, the maximum wave heights near the coast of Champerico (Guatemala) vary from 0.2 to 1.5 meters, and near the coast of Acajutla (Salvador) they reach 0.2m. The highest wave heights are reached near the coast of the earthquake located near the source, so near the coast of Salina Cruz (Mexico), (Fig. 13 (c)) the maximum wave heights vary from 0.3 to 2 meters.

Data from virtual tide gauges, namely, the maximum wave height, the greatest decrease in the water level and the time of wave arrival to points, can be seen in Table 3.

Table. 3. Data from virtual tide gauges obtained during Scenario 2 implementation.

City name	Maximum wave heights at 5m isobath (m)	Strongest water level depression at 5m isobath (m)	Time of approaching the point
01. Lazaro Cardenas (Mexico)	0.25	-0.19	00:36:15
02. Acapulco (Mexico)	0.16	-0.08	00:19:10
03. Puerto Escondido (Mexico)	0.48	-0.5	00:04:10
04. Salina Cruz (Mexico)	1.38	-1.58	00:00:50
05. Champerico (Guatemala)	0.34	-0.4	00:46:15
06. Acajutla (Salvador)	0.26	-0.3	01:19:10
07. El Cuco (Salvador)	0.09	-0.1	01:51:40
08. Tamarindo (Costa Rica)	0.09	-0.1	01:34:35

6. COMPARISON OF NUMERICAL SIMULATION RESULTS

Table 4 shows comparisons of the data obtained with the results given in [13, 14, 15, 16,] for the earthquake under consideration. It should be noted that for the earthquake under consideration, data are provided only at some points along the coast. In a number of points given in [13, 14, 15, 16], where we also had virtual tide gauges are displayed, we have the possibility to compare the computation data. These data are shown in Table 3.

Table 4. Comparison of computation results with real data and date of another authors

Maximum wave heights / Название пункта	Scenario 1	Scenario 2	[15]	[16]	Real data [13]	Real data [14]
01. Lazaro Cardenas (Mexico)	0.24	0.25	-	0.3	0.219	0.25
02. Acapulco (Mexico)	0.3	0.16	-	-	-	0.7
03. Puerto Escondido (Mexico)	0.59	0.48	-	-	-	-
04 Salina Cruz (Mexico)	1.35	1.38	1.8	2.1	1.33	1.2
05. Champerico (Guatemala)	0.39	0.34	-	-	-	-

06. Acajutla (Salvador)	**0.24**	**0.26**	**0.1**	**0.18**	**0.194**	**0.13**
07. El Cuco (Salvador)	**0.15**	**0.09**	**-**	**-**	**-**	**-**
08. Tamarindo (Costa Rica)	**0.19**	**0.09**	**-**	**-**	**-**	**-**

It can be seen that the results of our computations are in better agreement with real data than, e.g., with works [15, 16].

Figures 14 and 15 also show a comparison of the tide gauges of both scenarios with data taken from real sensors for the city of Salina Cruz (Mexico). For scenario 1 (Fig. 14) it can be seen that the time of income of a positive wave, as well as the maximum tendency of the behavior of the wave propagating from the earthquake source, remains to be unchanged.

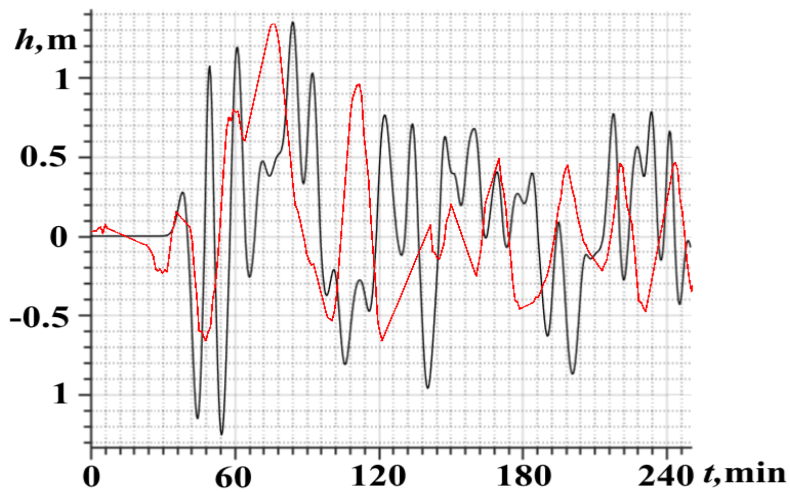

Fig. 14. Comparison of tide-gauge records of scenario 1 with real data for the city of Salina Cruz (Mexico)

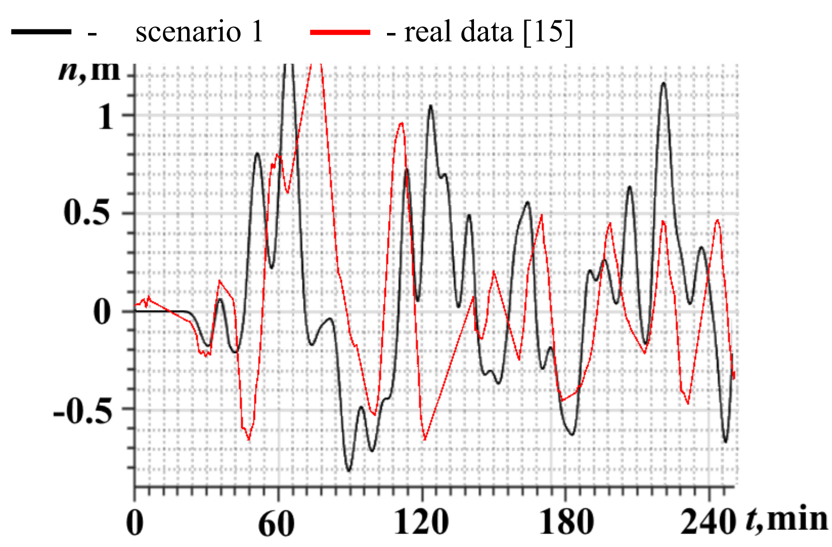

Fig. 15. Comparison of tide-gauge records of scenario 2 with real data for the city of Salina Cruz (Mexico).

Comparing scenario 2 with real data (Fig.15), it can be seen that in both cases the negative wave is the first to approach, and the maximum and minimum tendencies of the wave's behavior also remains to be unchanged.

Figures 16-19 show histograms for comparing the results of computations carried out in this work with the results of works [13, 14]. It is clearly seen that all scenarios are in good agreement with real data, with the exception of the point located in the area of 100 ° W (Acapulco city). The maximum heights do not exceed 3.8 m, both in our computations and in the histograms from [13, 14]. When comparing scenario 1 with work [13] (Fig. 16) and with work [14] (Fig. 17), it can be seen that the distribution of the maximum wave heights are similar, but in the region of 94 ° -96 ° W. there are differences. The maximum distribution of waves obtained in the implementation of scenario 2 has a distribution pattern that is closer to the works [13, 14] than the maximum distribution of scenario 1 (see Figs.17, 19).

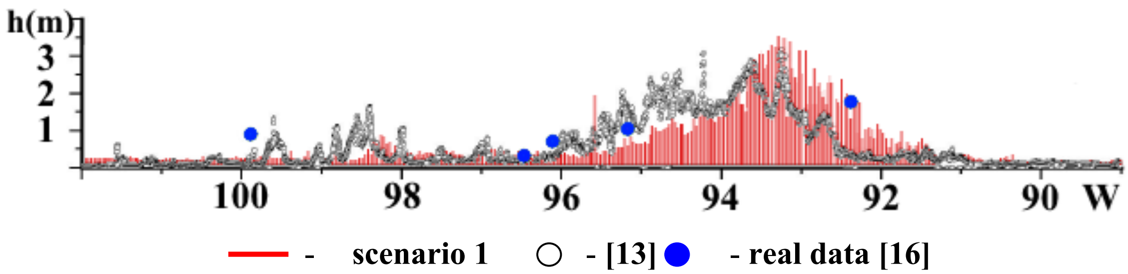

Fig. 16. Comparison of the histograms of the distribution of the maximum wave heights of scenario 1 with the work [13] for the calculated coast

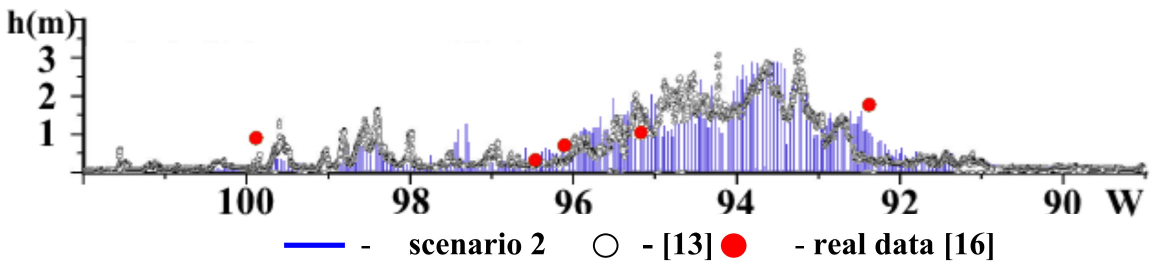

Fig. 17. Comparison of the histograms of the distribution of the maximum wave heights of scenario 2 with the work [13] for the calculated coast

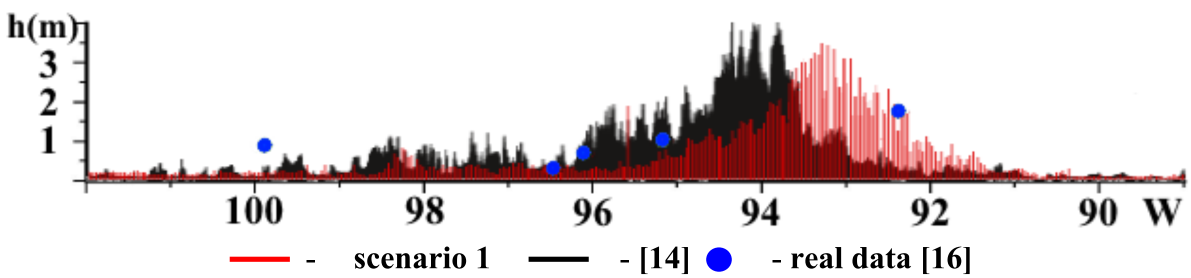

Fig. 18. Comparison of the histograms of the distribution of the maximum wave heights of scenario 1 with the work [14] for the calculated coast

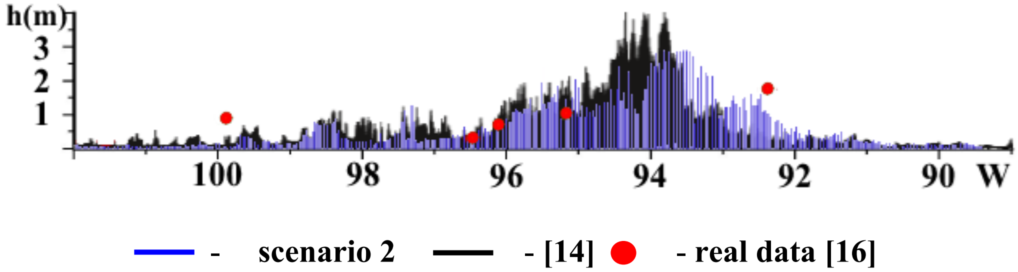

Fig. 19. Comparison of the histograms of the distribution of the maximum wave heights of scenario 1 with the work [14] for the calculated coast.

Thus, the analysis of the maximum wave heights for the selected 8 points of the water area in numerical modeling for a given earthquake magnitude, but different realization of the initial conditions, gives similar values for both far-field zones and near-field ones.

7. CONCLUSION

The paper considers a catastrophic earthquake with a magnitude of M = 8.1, which occurred in the southern region of Mexico on September 8, 2017. Numerical simulation of the generation of tsunami waves by a seismic source and their propagation over the water area was carried out. Modeling was carried out for two different mechanisms of the seismic source, at different locations. A two-block and four-block source with a negative movement oriented towards the coast is considered. In the area of the 5-meter isobath, the distribution histograms for the maximum wave heights are plotted. Comparison of wave characteristics mareograms showed that the selected mechanisms of the seismic source give good agreement with the numerical values of both real data and a number of other authors. Figures 16-19 show that the above computations indicate a close distribution of the maximum wave heights along the Mexican coast. This indicates the correct tendency for the selection of the dynamics of the seismic source during the implementation of this earthquake.

Acknowledgments

The research was supported by grant of the President of the Russian Federation for the state support of research projects by leading scientific schools of the Russian Federation (NSh-2485.2020.5).

REFERENCES

1. Mazova R.Kh. Soloviev S.L.. On influence of sign of leading tsunami wave on runup height on the coast // Science of Tsunami Hazards 12 (1994) 25-31.

2. M.RAMIREZ-HERRERA, N. CORONA, G. Suarez, A Review of Great Magnitude Earthquakes and Associated Tsunamis along the Guerrero, Mexico Pacific Coast: A Multiproxy Approach // American Geophysical Union. Published 2016 by John Wiley & Sons, Inc. 13 (2016)

3.R.WILSON, M. Ramirez-Herrera, L. Dengler, K. Miller, Y. LaDuke, Tsunami Generated by MW8.1 Chiapas, Mexico, Earthquake on September 7, 2017 // EERI Preliminary Notes on Tsunami Damage and Response , 13 (2017)

4. United States Geological Survey (USGS) https://earthquake.usgs.gov/

5. Pacific Coastal and Marine Science Center https://walrus.wr.usgs.gov/

6. Lobkovsky L.I. Geodynamics of spreading and subduction zones and two-level plate dynamics (Nauka Press, Moscow, USSR, 1988)

7. Voltzinger N. E., Klevanny K. A., Pelinovsky E. N. Long wave dynamics of the coastal zone, Leningrad: Gidrometeoizdat, 1989.272 p.

8. Pelinovsky E. N. Nonlinear dynamics of tsunami waves // Gorky: IAP USSR Acad.of Sci., 1982 .—226p.

9. Lobkovsky L.I., Mazova R.Kh., Baranov B.V., Kataeva L.Yu. Generation and propagation of tsunamis in the Sea of Okhotsk: possible scenarios // DAN, T.410, pp.528-532, 2006.

10. Lobkovsky L., Mazova R., Tyuntyaev S., Remizov I. Features and Pronlems with Historical Great Earthquakes and tsunamis in the Mediterranean Sea // Journal Science of Tsunami Hazards, Vol. 35, .No. 3, pp. 167-188, (2016).

11. Lobkovsky L., Garagash I., Baranov B., Mazova R., Baranova N., Modeling Features of Both the Rupture Process and the Local Tsunami Wave Field from the 2011 Tohoku Earthquake, Pure Appl. Geophys. (2017). V.174, p. 3919-3938, doi: 10.1007 / s00024-017-1539-5 (March 2017) pp.1-20.

12. WELLS D.L., Coppersmith K.J. New empirical relationships among magnitude, rupture length, rupture width, rupture area, and surface displacement // Bull. Seism. Soc. Am. 1994. Vol. 84. P. 974-1002

13. B. ADRIANO, E. Mas, S. Koshimura, Preliminary Tsunami Simulation of the Mw = 8.1 (USGS) - 96km SW of Pijijiapan, Mexico (ver. 2) // Laboratory of Remote Sensing and Geoinformatics for Disaster Management IRIDeS, Tohoku University, JAPAN, 7 (2017)

14. B. ADRIANO, Y. Fujii, S. Koshimura, E. Mas, A. Ruiz-Angulo, M. Estrada, Tsunami Source Inversion Using Tide Gauge and DART Tsunami Waveforms of the 2017 Mw8.2 Mexico Earthquake // Pure Appl ... Geophys. 175 (2018), 35–48

15. Global Disaster Alert and Coordination System (GDACS) http://www.gdacs.org/

16. Tsunami Bulletin Board, Tsunami Information Center (ITIC) http://www.ioc-sealevelmonitoring.org/

ISSN 8755-6839

SCIENCE OF TSUNAMI HAZARDS

Journal of Tsunami Society International

Volume 39 Number 4 2020

ESTIMATION OF RUPTURE DIRECTIVITY, CMT AND EARTHQUAKE TSUNAMI PARAMETERS AND THEIR CORRELATION WITH THE MAIN SOURCE OF THE FIRST TSUNAMI WAVE, SEPTEMBER 28, 2018

Madlazim*,[1,2] Tjipto Prastowo,[1,2] and Muhammad Nurul Fahmi[3]

[1]*Physics Department, The State University of Surabaya, Surabaya 60231, INDONESIA. E-mail: madlazim@unesa.ac.id*
[2]*Center for Earth Science Studies, The State University of Surabaya, Surabaya 60231, INDONESIA*
[3]*Physics Department, Postgraduate Program, Institut Teknologi Sepuluh Nopember, Surabaya 60111, INDONESIA*

ABSTRACT

The purpose of this study is to analyze the main source of the Palu-Indonesia tsunami based on the direction of rupture, Centroid Moment Tensor (CMT), the tsunami parameters, including the rupture duration (T_{dur}), the 50 Seconds Exceed Duration (T50ex) and the dominant period (T_d) of the earthquake that occurred on September 28, 2018. The method employed in this study involves fitting the rupture duration versus seismic station azimuth graph to estimate the direction of the rupture, the full waveforms inversion method for determining the CMT and the direct procedure method for estimating tsunami parameters. The estimated direction of the earthquake rupture is azimuth 179°, which almost coincides with the Palu Koro Fault (PKF) azimuth. The direction of the earthquake rupture passed below the surface of the seawater in Palu Bay, which could possibly be the main source of the tsunami. The strike and dip of the nodal plane generated by the earthquake are 350° and 64°, respectively, which shows that a vertical displacement pushed seawater vertically in Palu Bay and caused the tsunami. All tsunami parameters from the earthquake exceeded the threshold; therefore, it is very likely that the earthquake was the main source of the first tsunami wave. The estimation results of the rupture directivity, Centroid Moment Tensor, and tsunami parameters are confirmed by inundation data that are qualitatively comparable with the observations.

Keywords: *Earthquake Rupture Duration; CMT; Tsunami Parameters; Tsunami Source; Inundation*

1. INTRODUCTION

A tectonic earthquake with a magnitude of 7.5 occurred some time ago around the Palu-Koro fault. The cause of the earthquake was speculated to be a submarine landslide, which could have caused tsunamis in Palu and Donggala on September 28, 2018. Even though three phenomena of earth disasters simultaneously occurred (earthquake, tsunami, and liquefaction), the most detrimental among the three phenomena was the tsunami phenomenon.

A tsunami is a phenomenon of sea surface wave propagation generated by the release of endogenous energy from the earth via the mechanism of tectonic earthquakes, submarine landslides, or other sources (Ward 2011). Large tsunamis associated with submarine strike-slip earthquakes are very rare. Strike-slip faults usually produce small tsunamis due to a lack of large vertical deformation (Gusman *et al.* 2017; Lay *et al.* 2018). However, the Palu-Koro fault zone that crosses Sulawesi Island is a strike-slip fault system in a complex tectonic region, which could facilitate vertical deformation. The strike-slip system may also include complicated fault geometry, such as nonvertical faults, arches, etc. This fault geometry can lead to complex fracture dynamics and produce a variety of pattern shifts during fractures, which can trigger tsunamis (Legg & Borrero 2001; Borrero *et al.* 2004).

Recorded history for local tsunamis generated by other strike-slip faults, such as the 1906 earthquake in San Francisco California, the 1994 earthquake in Mindoro Philippines, the 1999 earthquake in Izmit Turkey (Legg *et al.* 2003), and the 2016 Kaikoura earthquake in New Zealand (Power *et al.* 2017; Ulrich *et al.* 2019a). Large-scale strike-slip earthquakes can also produce tsunami aftershocks (Geist & Parsons 2005). We employ several ways to mitigate the tsunami disaster generated by the strike-slip fault system: first, by knowing the position and direction of the maximum main stress, intermediate stress and minimum stress from an area where strike-slip faults have been identified; second, by knowing the direction of the rupture caused by the September 28, 2018 earthquake; and third, a tsunami generated by the strike slip fault can also be analyzed using the tsunami parameters, namely, the rupture duration (T_{dur}), the duration greater than 50 seconds (T50ex) and the dominant period (T_d) (Lomax & Michelini 2011; Madlazim 2013).

Research on the direction of the rupture, which has been carried out by Madlazim (2011), provides results to estimate the direction of the rupture using short-period signals that have been recorded by two pairs of stations. If the duration of the rupture of the signal directed by the station is smaller than the signal recorded by the pairing station, then it can be interpreted that the direction of the rupture is toward this station. Madlazim *et al.* (2019) has also conducted research on the use of tsunami parameters for tsunami early warning applications 4 minutes after an earthquake. The results of the study indicated that a false warning was not issued for any of the 300 earthquakes that occurred in Indonesia. Tsunami parameters in the form of rupture duration (T_{dur}), duration greater than 50 seconds (T50ex) and dominant period (T_d) are useful to test whether the main source of the tsunami on September 28, 2018 is caused by seismic energy or landslides.

Tsunami parameters are useful for detecting whether an earthquake can cause a tsunami. Lomax & Michelini (2009b, 2011) have determined that the rupture length parameter of an earthquake is the most dominant parameter as an indicator of a tsunami, while it is known that the rupture length is proportional to the earthquake rupture duration; so the earthquake rupture duration can be applied for early warning of tsunamis (Geist & Yoshioka 1996). In addition, the duration of the rupture can also provide additional information about the direction of the rupture, which can be useful for explaining how a tsunami could occur after the earthquake on September 28, 2018.

Centroid Moment Tensor (CMT) is the most complete and accurate information about earthquake sources; it has previously been investigated by many seismologists, including Kasmolan *et al.* (2010) and Ichinose *et al.* (2003). The Centroid Moment Tensor is utilized to determine the strike, dip and rake angles of an earthquake. Among these three angles, two angles are related to tsunami events, namely, the strike angle and the dip angle. The strike angle is determined from the North moving in a clockwise direction. Generally, the direction of the strike is the direction of the fault that caused the earthquake. The direction of earthquake rupture is usually in the direction of the fault that caused the earthquake. The dip angle illustrates the slope of the fault plane with respect to the horizontal plane. For a 90 ° dip angle, the fault plane is vertical. In this condition, it is not possible for an earthquake to generate a tsunami because there is no vertical displacement; so it is not possible to push vertical water above sea level.

The results of the calculation of the direction of the rupture, the Centroid Moment Tensor and tsunami parameters were confirmed with inundation data to determine the rational primary source of the tsunami on September 28, 2018, seismic energy or landslides. Researchers classified the research results related to the main source of tsunamis in Palu on September 28, 2018. There are 3 sources of tsunamis. First, the main source of tsunamis is seismic energy (Ulrich *et al.* 2019b). Second, the main source of tsunamis is landslide energy (Sepulveda *et al.* 2018; Heidarzadeh *et al.* 2019). Third, the main source of tsunamis is seismic energy, which is reinforced by landslide energy (Liu *et al.* 2018; van Dongeren *et al.* 2018).

In the research by Ulrich *et al.* (2019b), it has been concluded that the main source of the tsunami in Palu after the earthquake of September 28, 2018 was caused by seismic movements, which produced vertical movements that could cause tsunamis. This finding has been proven via earthquake dynamics modeling, in which the time and rupture speed, 3D geometric complexity of the fault, and effect of seismic waves on the propagation of the rupture are important parameters and is also supported by tsunami amplitude modeling and inundation height data.

In this study, we have discussed the main tsunami sources that were released from seismic earthquakes or landslides using analysis of the direction of rupture, Centroid Moment Tensor, and tsunami parameters that occurred after the Palu earthquake on September 28, 2018. Furthermore, the results of the estimation of the three seismic quantities were confirmed by the travel time data of the inundation recorded by the tide gauge around Palu Bay.

2. SETTING OF PALU-KORO FAULT

Sulawesi is located in the eastern part of Indonesia, which experiences high seismic activity. Sulawesi Island is located at the triple junction between the Sunda plate, Australian plate and Philippine Sea (Bellier *et al.* 2006; Socquet *et al.* 2006, 2019) (Fig. 1a). This condition can cause the area around Sulawesi to be very prone to earthquakes. The Australian Plate and Philippine Sea are centered toward the Sunda plate due to the subduction and rotation zones of the Molucca Sea, Banda Sea and Timor Plate, which causes a complicated fault pattern.

The Central Sulawesi region is one of the earthquake prone areas in Indonesia because it is located near the source of earthquakes, which originates both on land and at sea. The source of an earthquake in the sea is the subduction of the Sulawesi and Molucca Sea Plates, while the source of an earthquake on land is several active faults on the mainland of Central Sulawesi, one of which was the Palu Koro Fault.

The Palu Koro fault, which is located along the Palu Koro valley and stretches from Palu Bay in the southeast direction, caused the Palu earthquake on September 28, 2018. This fault is the main geological structure in Central Sulawesi Province. According to the latest geodetic measurements, the Palu-Koro fault has a relatively high slip rate of 40 mm/year (Walpersdorf *et al.* 1998; Socquet *et al.* 2006), and according to geomorphology, the upper limit is 58 mm/year (Daryono 2018). The focal mechanism of the Palu-Koro fault indicated that it has a dip value of 65, which most likely caused the tsunami strike-slip earthquake that occurred on September 28, 2018 (Ulrich *et al.* 2019b). The Palu Koro fault has caused many tsunami disasters. According to Watkinson & Hall (2017), the Palu-Koro Fault is considered to pose a threat to the area through which it passes. Referring to previous data, four tsunamis were caused by the earthquake in the Palu-Koro fault that struck the northwest coast of Sulawesi in the past century (1927, 1938, 1968 and 1996) (Pelinovsky *et al.* 1997; Prasetya *et al.* 2001).

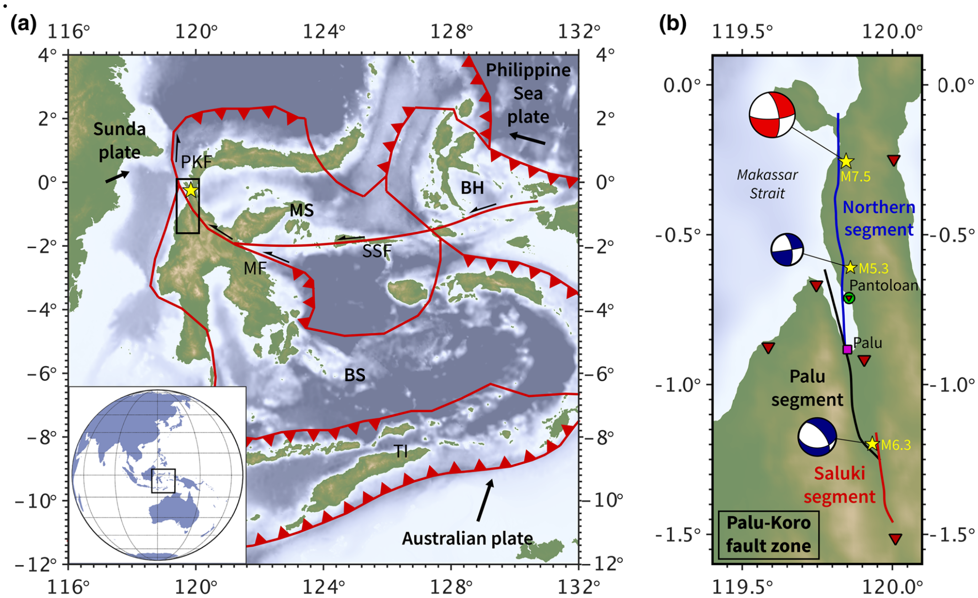

Fig. 1. (a) Tectonic structure of the Palu-Koro fault; the epicenter of the September 28, 2018 earthquake is marked by a yellow star (Ulrich et al., 2019b).

In Figure 1.(a) above the plate boundaries are marked with black lines that represent Bird (2003), Socquet *et al.* (2006), and Argus *et al.* (2011). PKF is the Palu-Koro fault zone; MF is the Matano fault zone; MS is the Molucca Sea plate; SSF is the Sula-Sorong fault zone; TI is the Timor plate; BH is the Bird's Head plate; and BS is the Banda Sea plate. The black arrows indicate the far-field plate velocities with respect to Eurasia (Socquet *et al.* 2006).

The black square represents the enlarged area at point (b), which is a magnification of the picture in the black box that shows the area where the earthquake occurred. The red triangle denotes an earthquake recording station. The focal mechanisms and epicenters of the earthquake on September 28, 2018 are shown: the top event was obtained from (USGS 2018), for the middle event is the aftershock earthquake on October 1, 2018 and the lowest event is the earthquake that occurred on January 23, 2005. The two latter events can be obstacles to the dip of the Palu-Koro fault.

3. METHODS

The method employed in this study is the method for fitting the data of rupture vs azimuth station seismic duration to estimate the direction of the rupture, the full waveforms inversion method for estimating earthquake CMT, and the direct procedure method for estimating tsunami parameters (rupture duration, dominant period, and 50 seconds exceed duration).

3.1. Estimation of Rupture Direction

The direction of the earthquake rupture can be estimated from the following equation. The duration of the rupture (T_{dur}) can be determined using the direct procedure for an earthquake seismogram, as expressed by Eq. (1).

$$Tdur=LVr-LVpcos\theta \qquad (1)$$

where L is the length of the rupture, Vr is the rupture speed, Vp is the phase velocity and θ is the angle between the azimuth station and the fault azimuth. The direction of the rupture can be estimated from Eq. (1) when the angle θ is zero, which means that T_{dur} has a minimum value (Hwang *et al.* 2011).

The duration of the rupture T_{dur} in Eq. (1) is estimated from the delay time after the arrival of the P wave for 90% ($T^{0,9}$), 80% ($T^{0,8}$), 50% ($T^{0,5}$), and 20% ($T^{0,2}$) from the peak value (Lomax & Michelini 2009a). The mathematical equation to calculate T_{dur} can be determined as follows:

$$Tdur=1-wT0,9+wT0,2 \qquad (2)$$

$$w\ =T0,2+T0,52-2040s \qquad (3)$$

with a limit of $T^{0,9} < T_{dur} < T^{0,2}$

T_{dur} can be estimated using seismogram data downloaded from the IRIS website, http://ds.iris.edu/wilber3/find_event. We employ the distance between the earthquake epicenter and the farthest seismic station, which is 40° from the azimuth station from 0° to 360°. Vertical component seismogram data from 56 seismic stations were utilized.

3.2. Full Waveform Inversion

The Centroid Moment Tensor from the September 28, 2018 earthquake can be determined by the full waveform inversion method developed by Ichinose *et al.* (2003). This method applies a three-component local waveform that is recorded by a seismic station and then estimated using the Green function. To calculate the Green function, we need a speed model for 1 dimension. The Green function is a picture of the signal to be recorded by a seismograph to obtain the model of the signal. The three-component Green function equation can be written as,

$$unx,t=Mij\xi,t*\partial \quad \partial\xi jGnjx,\xi,t\xi 0$$

$$Mij\xi,t*Gn,jx,\xi,t \tag{4}$$

where un is the n-shift record, $Mij$is the 6 component moment tensor at the point of the earthquake source, ξ is the position of the earthquake source, x is the position of the receiver, Gn,j is a Green function depending on the elastic nature of the earth and the sign ($*$) shows convolution.

3.3. Estimation of Tsunami Parameters (T_{dur}, T_d, and T_{50ex})

To determine the values of the tsunami parameters, we employed the direct measurement procedure that has been developed by (Lomax & Michelini 2011; van Dongeren *et al.* 2018). The parameters for earthquakes can be determined via high frequency (HF) analysis of the vertical components of broadband seismograms that have been described in the study (Lomax *et al.* 2007; Lomax & Michelini 2009a, 2009b, 2011; Madlazim 2011), as shown in Eq. 5. T_d can be estimated using the direct method without inversion, which accelerates the process. To determine the dominant period (T_d), T_d is calculated using the time domain (τc) with the following equation (Nakamura 1988; Wu & Kanamori 2005; Lomax & Michelini 2013):

$$\tau c=2\pi T1T2v2tdtT1T2v2tdt \tag{5}$$

where T_1 = 0 seconds (P onset) and T_2 = 55 seconds from a teleseismic earthquake seismogram (Lomax & Michelini 2009a). T_{50Ex} estimation was performed using the direct procedure of earthquake seismograms, namely, (1) filtering the velocity seismogram of vertical components using a high-frequency Butterworth filter (1-5 Hz), (2) automatically selecting P wave arrival times, (3) calculating the RMS amplitude (Ar) and the duration of 50 seconds after the arrival of P waves, (4) calculating T_{50Ex}, which is the ratio T50/Ar (Lomax & Michelini 2009b). Measurement of tsunami parameters caused by earthquakes in real time has been applied and can be accessed on the web http://aptsunami.fmipa.unesa.ac.id/www/

To estimate the tsunami parameters, T_{dur}, T_d, and T_{50Ex} in this study utilized seismogram data downloaded from the IRIS website: http://ds.iris.edu/wilber3/find_event. We apply the distance between the earthquake epicenter and the farthest seismic station at 15° with the azimuth of the station from 0° to 360°. Vertical component seismogram data recorded by 20 seismic stations were employed.

4. RESULTS AND DISCUSSION

The results of the estimated direction of the rupture, Centroid Moment Tensor (CMT) and tsunami parameters to test the main source of the tsunamis that occurred after the earthquake on September 28, 2018 are explained as follows:

4.1. Rupture Directivity

To estimate the direction of the earthquake rupture on September 28, 2018, we collected data from 56 seismic stations that have the closest azimuth, whose value is 1.82° to the station that has the furthest azimuth value of 356,83°. We calculated the value of rupture duration (T_{dur}) for each station.

The blue dots in Fig. 2 represent the earthquake rupture duration data for each azimuth; they are fitted to form a red line. On the red line, two hills of waves and 1 valley of waves are formed, which means that on the two hills of waves, a high average T_{dur} value occurs at azimuth 1.82° to 6.89° and 255.84° to 356.83°, whereas a low average T_{dur} value occurs at azimuth 140.33° to 193.28°, for 1 valley. In the data, we the lowest T_{dur} value of 10.8 s occurred on the 179° azimuth. To determine the direction of the rupture, the smallest T_{dur} value is interpreted as the direction of the rupture, according to the results of the study by Hwang *et al.* (2011) and Madlazim (2011). If the duration of the rupture of the signal recorded by the station is smaller than the signal recorded by the other station, then it can be interpreted that the direction of the rupture is oriented toward this station.

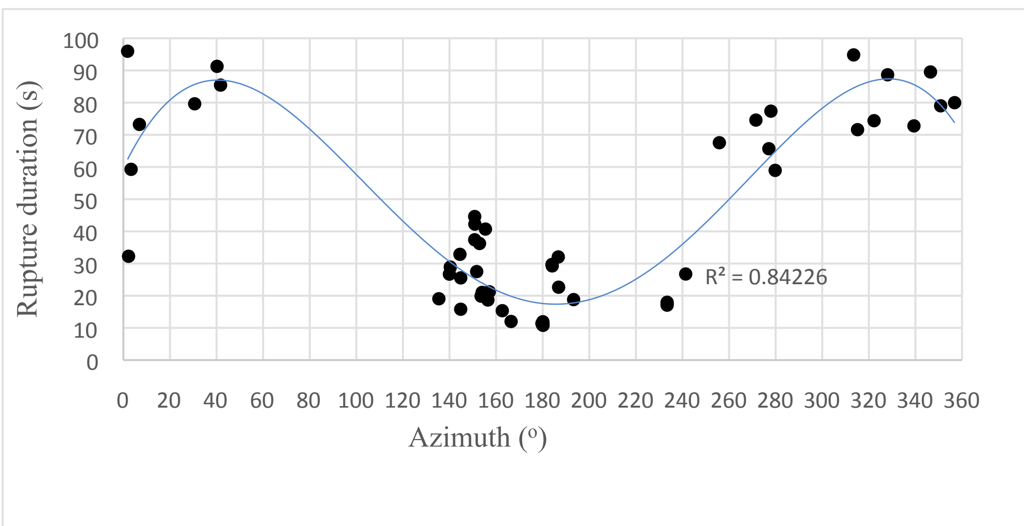

Fig. 2. Relationship between the duration of rupture (T_{dur}) with the azimuth seismic station that records data waveforms. In this graphic, there are 56 data points from the station that recorded the earthquake on September 28, 2018.

In the case of September 28, 2018, the direction of the rupture moved in the direction of the azimuth 179°, which means that it almost coincides with the Palu-Koro Fault zone (Fig. 1b). Thus, the direction of the rupture passes through the underwater segment of the Palu bay, where according to research by Heidarzadeh *et al.* (2019), the maximum tsunami wave heights at two tidal gauge stations, Pantoloan (in Palu Bay) and Mamuju (outside Palu Bay) are 380 cm and 24 cm, respectively. This finding is correlated with Ulrich *et al.* (2019b), who concluded that the tsunami that occurred after the September 28, 2018 earthquake was largely localized in Palu Bay. Thus, the estimation results of this rupture direction are consistent with the results of the study, which indicates the main source of the tsunami that occurred after the September 28, 2018 earthquake was a seismic earthquake. The results of this study are supported by the results of research by Ulrich *et al.* (2019b) and Madlazim *et al.* (2019).

4.2. Centroid Moment Tensor

Part of the results of the CMT estimation are strike, dip, and rake values in the September 28, 2018 earthquake. Fig. 3 shows the results of a description of the full waveform fitting between observed data and synthetic data that have been calculated by the Green function. Each seismic station that records an earthquake has three local components that are observed and symbolized as T for the tangential component, R for the radial component, and Z for the vertical component. Black waveforms indicate waveforms obtained from observational data, while red waveforms indicate synthetic waveforms obtained from calculations. The matching level of local fitting full waveforms between synthetic signals (red) and observed signals (black) is expressed by the percentage value of Variance Reduction (VR). The full-waveform inversion in this study employs a frequency of 0.02 Hz to 0.05 Hz and uses a 3-component local signal recorded by 5 seismic stations (Fig. 4), which causes a Variance Reduction (VR) value of 81%. If the VR value exceeds 50%, the results of the CMT solution can be categorized as reliable (Vackář *et al.* 2017).

The value of the focal mechanism at the source modeled in this study are strike, dip, and rake angles of 350°, 64°, and -6°, respectively, which is very close to the value of the focal mechanism released by USGS, namely, 350°, 65°, and -17°. The 350 ° strike angle corresponds to the Palu-Koro Fault (PKF) direction. From this strike angle, it can be seen that the direction of the rupture that leads to the station passed through Palu bay. The dip angle of 64 ° is almost the same as the CMT estimate of Ulrich *et al.* (2019b). The dip angle of 64 ° indicates a shift in the vertical component, which pushed seawater vertically and caused the tsunami. The same results were also obtained by Ulrich *et al.* (2019b), who discovered that the dip value from the Palu-Indonesia earthquake on September 28, 2018, is 65°. Fig. 4 is an image of the station distribution map utilized in this study. We employed 5 stations (SMKI.IA SGKI.IA BKB.IA, TOLI2.IA, and LUWI.IA), whose positions include the earthquake epicenter and earthquake focal mechanism (Fig. 4).

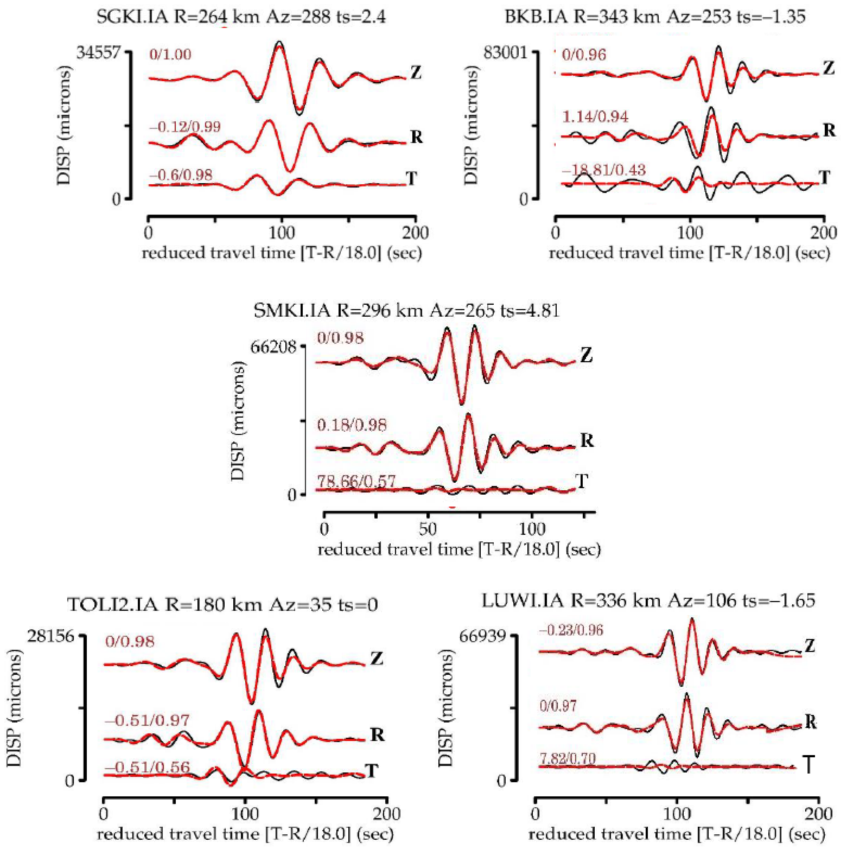

Fig. 3. Results of full waveform inversions between synthetic data and earthquake observation data on September 28, 2018.

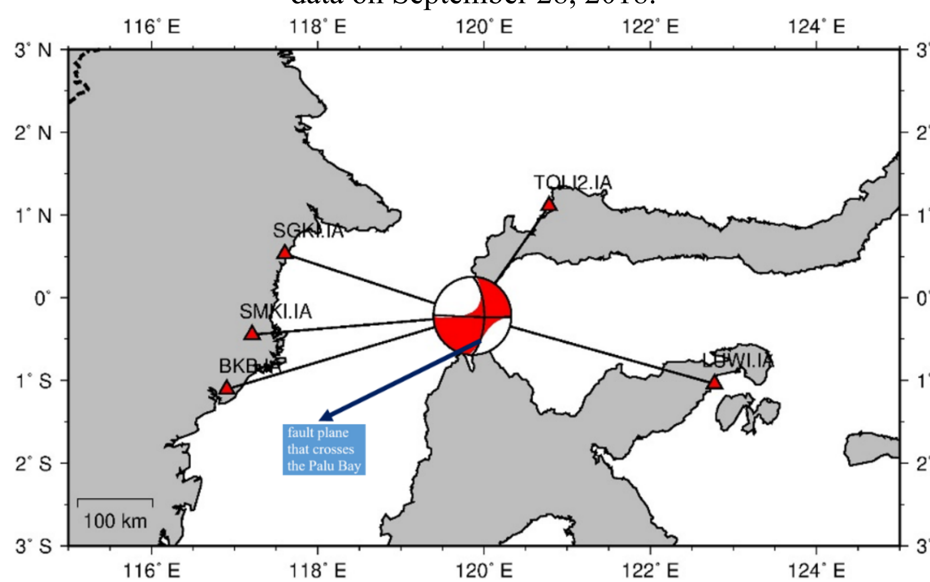

Fig. 4. Results distribution map of 5 seismic stations and earthquake beach ball on September 28, 2018, whose direction of strike angle passes through Palu Bay, which corresponds to the direction of the PKF (Ulrich *et al.* 2019b).

4.3. Tsunami Parameters

Three tsunami parameters are applied to indicate whether an earthquake has the potential to cause a tsunami. The three tsunami parameters are the duration of rupture (T_{dur}), dominant period (T_d) and 50 Seconds Exceed Duration (T_{50Ex}). If the T_{dur} exceeds or is equal to the 65-second threshold, an earthquake has the potential to cause a tsunami. If the T_{dur} is less than the threshold, the earthquake has no tsunami potential. If T_d exceeds or is equal to the 10-second threshold, an earthquake has the potential to cause a tsunami. If T_d is less than the threshold, then an earthquake has no tsunami potential. If T_{50Ex} exceeds or equals a threshold of 1, an earthquake has the potential to cause a tsunami. If T_{50Ex} is less than the threshold, then an earthquake has no tsunami potential. The following examples present the results of the T_{dur}, T_d and T_{50Ex} estimates from the earthquake seismogram on September 28, 2018, as recorded by the PLAI seismic station, where all three tsunami parameters exceed the threshold.

Data from the estimated tsunami parameters from an average of 20 seismic stations employed in this study are presented in Table 1 as follows:

All tsunami parameters estimation results presented in Table 1 exceed the threshold. Thus, the results of the estimated tsunami parameters support the hypothesis that the main source of the tsunamis that occurred after the September 28, 2018 earthquake was a seismic earthquake. The results of this study are supported by the results of research by Ulrich *et al.* (2019b) and Madlazim *et al.* (2019).

Simulations of inundation heights at various locations around Palu Bay, where observations have been recorded by Ulrich *et al.* (2019b) and then observed with some estimates, yielded inundation data that was too high in the northern boundary of Palu bay and a little too low in the southern part near the Grandmall of Palu City. These findings conclude that large errors at the height of the inundation are randomly distributed and the inundation originates from the effect of local amplification, which cannot be captured in the scenario due to a lack of bathymetry/topographic resolution. The maximum water depth is calculated from the tsunami scenario near Palu City. Qualitatively, the results of this scenario are quite consistent with the observations, because the depth of the largest puddle is close to the Grandmall area, where major damage from the tsunami was reported. Tsunami scenarios stem from seismic displacement from dynamics. Earthquake rupture scenarios produce inundations that are qualitatively comparable to available observations. The wave amplitude and the height of the puddle fits well given the limited quality of available topographic data (Ulrich *et al.* 2019b).

All tsunami parameters from the earthquake on September 28, 2018 exceed the threshold; so it is very likely that earthquakes are the main source of tsunamis. The estimated results of the rupture direction, CMT, and tsunami parameters are confirmed by waterlogging data that are qualitatively comparable with available observations. The wave amplitude matches well (Ulrich *et al.* 2019b).

Table 1. Average values of the tsunami parameters for the September 28, 2018 earthquake

T_{dur} (s)	T50Ex	T_d (s)	T_{dur}*T_d (s^2)	T_d*T50Ex (s)
93.01	2,01	10.39	966.47	21.50

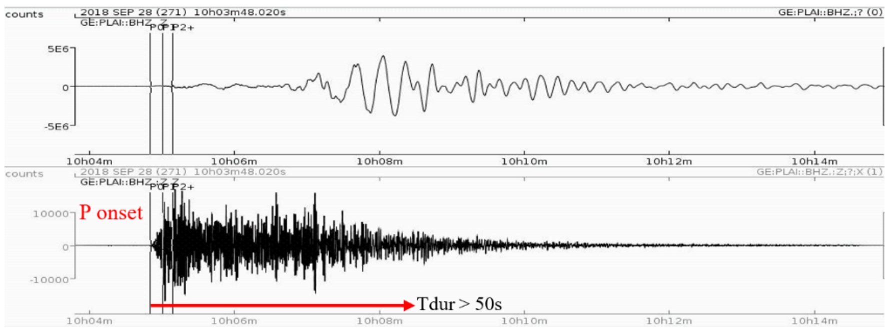

Fig. 5. Seismogram recorded by PLAI station (above), Rupture Duration (T_{dur}) = 120.0s.

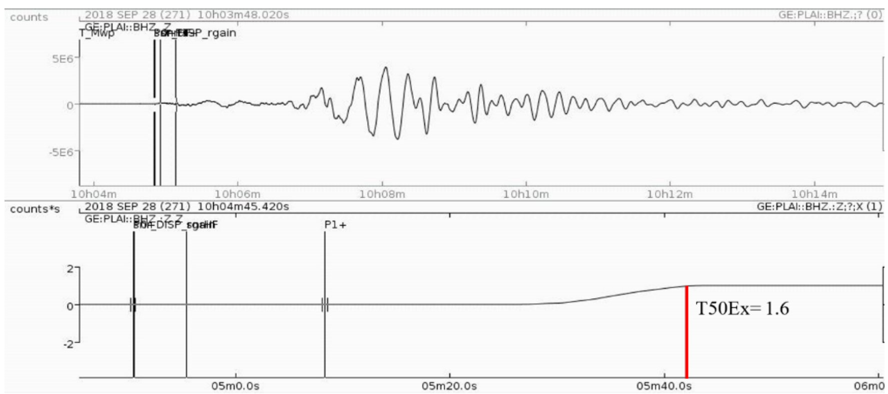

Fig. 6. Seismogram recorded by PLAI station (above), Exceed duration (T_{50Ex}) = 1.6.

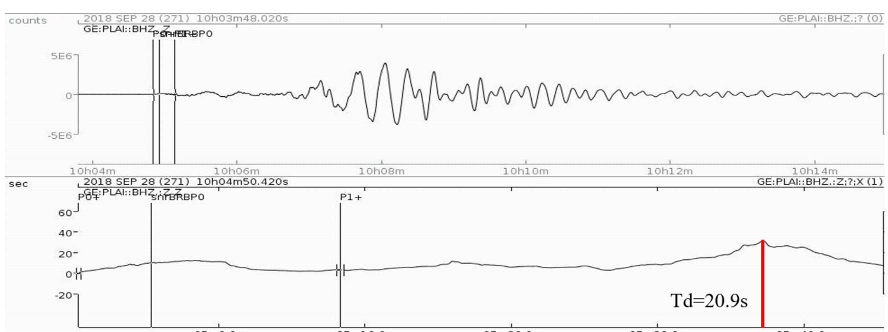

Fig. 7. Seismogram recorded by PLAI station (above), dominant period (T_d) = 20.9 s.

Based on the observations as shown in the video which can be accessed at the following link https://www.youtube.com/watch?v=y0UOfVr7jBE . There were three tsunami waves after the Palu earthquake on September 28, 2018. The height of the first tsunami wave was not too big, on average, it was around 0.8 meters, but it was enough to make the people around the Palu Strait coast surprised because previously the tsunami early warning had been canceled. This first tsunami wave was generated by the seismic energy from the earthquake. Meanwhile, the height of the second and third tsunami waves on the coast of the Palu Strait was very large, more than 6 meters. This could not have been caused by a strike-slip type earthquake, but it is very likely that it was caused by a landslide whose water waves were amplifying.

5. CONCLUSIONS

Based on the estimation of the direction of the rupture, the rupture moves in the direction of the azimuth 179°, which means that it passes under Palu bay, where there is a maximum tsunami wave height. The results of the CMT solution are in the form of a strike angle of 350°, which corresponds to the PKF direction and rupture direction. A dip angle of 64° indicates the existence of a vertical displacement component that can push the water in Palu bay, which eventually causes a tsunami. The tsunami parameter estimation results also support that the main source of tsunamis that occurred after the earthquake on September 28, 2018, was a seismic earthquake because all tsunami parameters exceed the threshold. Thus, it is very likely that earthquakes comprise the main source of the first tsunamis wave. The estimation results of the direction of the rupture, CMT, and tsunami parameters are confirmed by inundation data from tsunamis, bathymetry/topography, in which there is a wave height of seawater.

ACKNOWLEDGMENTS

The authors sincerely thank the Indonesian Agency for Geophysics, Climatology, and Meteorology (BMKG) Indonesia for providing the earthquake data employed in this study, GEOFON GFZ and Incorporated Research Institutions for Seismology (IRIS) for the seismic data were available from their respective sites at http://eida.gfz-potsdam.de/webdc3/ and http://www.iris.edu/wilber3/find. This article has also benefited from constructive reviews from two anonymous reviewers. We also thank the Ministry of Education and Culture's DRPM for supporting this research. This work is funded by DRPM, The Ministry of Education and Culture, The Republic of Indonesia under grant number B/11632/UN38.9/LK.04.00/2020.

REFERENCES

Argus, D.F., Gordon, R.G. & DeMets, C., 2011. Geologically current motion of 56 plates relative to the no-net-rotation reference frame, *Geochem. Geophys. Geosystems*, 12, Q11001.

Bellier, O., Sébrier, M., Seward, D., Beaudouin, T., Villeneuve, M. & Putranto, E., 2006. Fission track and fault kinematics analyses for new insight into the Late Cenozoic tectonic regime changes in West-Central Sulawesi (Indonesia), *Tectonophysics*, 413, 201–220.

Bird, P., 2003. An updated digital model of plate boundaries, *Geochem. Geophys. Geosystems*, 4, 1027.

Borrero, J.C., Legg, M.R. & Synolakis, C.E., 2004. Tsunami sources in the Southern California bight, *Geophys. Res. Lett.*, 31, 211.

Daryono, M.R., 2018. Paleoseismologi tropis Indonesia (dengan studi kasus di Sesar Sumatra, Sesar Palukoro-Matano, Dan Sesar Lembang). Available at: http://docplayer.info/111161004-Paleoseismologi-tropis-indonesia-dengan-studi-kasus-di-sesarsumatra-sesar-palukoro-matano-dan-sesar-lembang-disertasi.html, Accessed September 2019.

Geist, E. & Yoshioka, S., 1996. Source parameters controlling the generation and propagation of potential local tsunamis along the Cascadia margin, *Nat. Hazards*, 13, 151–177.

Geist, E.L. & Parsons, T., 2005. Triggering of tsunamigenic aftershocks from large strike-slip earthquakes: analysis of the November 2000 New Ireland earthquake sequence, *Geochem. Geophys. Geosystems*, 6, Q10005.

Gusman, A.R., Satake, K. & Harada, T., 2017. Rupture process of the 2016 Wharton Basin strike-slip faulting earthquake estimated from joint inversion of teleseismic and tsunami waveforms, *Geophys. Res. Lett.*, 44, 4082–4089.

Heidarzadeh, M., Muhari, A. & Wijanarto, A.B., 2019. Insights on the source of the 28 September 2018 Sulawesi Tsunami, Indonesia based on spectral analyses and numerical simulations, *Pure Appl. Geophys.*, 176, 25–43.

Hwang, R.-D., Chang, J.-P., Wang, C.-Y., Wu, J.-J., Kuo, C.-H., Tsai, Y.-W., Chang, W.-Y. & Lin, T.-W., 2011. Rise time and source duration of the 2008 MW 7.9 Wenchuan (China) earthquake as revealed by Rayleigh waves, *Earth Planets Space*, 63, 427–434.

Ichinose, G., Anderson, J., Smith, K. & Zeng, Y., 2003. Source parameters of Eastern California and Western Nevada earthquakes from regional moment tensor inversion, *Bull. Seismol. Soc. Am.*, 93, 61–84.

Kasmolan, M., Santosa, B.J., Lees, J.M. & Utama, W., 2010. Earthquake source parameters at the sumatran fault zone: identification of the activated fault plane, *Cent. Eur. J. Geosci.*, 2, 455–474.

Lay, T., Ye, L., Bai, Y., Cheung, K.F. & Kanamori, H., 2018. The 2018 MW 7.9 Gulf of Alaska earthquake: multiple fault rupture in the Pacific plate, *Geophys. Res. Lett.*, 45, 9542–9551.

Legg, M.R. & Borrero, J.C., 2001. Tsunami potential of major restraining bends along submarine strike-slip faults, in *Proceedings of the International Tsunami Symposium*, pp. 331–342, NOAA/PMEL.

Legg, M.R., Borrero, J.C. & Synolakis, C.E., 2003. Tsunami hazards from strike-slip earthquakes. American Geophysical Union, Fall Meeting 2003, abstract id OS21D-06. Available at: http://docplayer.info/111161004-Paleoseismologi-tropis-indonesia-dengan-studi-kasus-di-sesarsumatra-sesar-palukoro-matano-dan-sesar-lembang-disertasi.html, Accessed September 2019.

Liu, P.L.F., Barranco, I., Fritz, H.M., Haase, J.S., Prasetya, G.S., Qiu, Q., Sepulveda, I., Synolakis, C. & Xu, X., 2018. What we do and don't know about the 2018 Palu Tsunami—a future plan. In AGU fall meeting 2018. Available at: https://agu.confex.com/agu/fm18/meetingapp.cgi/Paper/476669, Accessed 2019.

Lomax, A. & Michelini, A., 2009a. Mwpd: a duration–amplitude procedure for rapid determination of earthquake magnitude and tsunamigenic potential from P waveforms, *Geophys. J. Int.*, 176, 200–214.

Lomax, A. & Michelini, A., 2009b. Tsunami early warning using earthquake rupture duration, *Geophys. Res. Lett.*, 36, L09306.
Lomax, A. & Michelini, A., 2011. Tsunami early warning using earthquake rupture duration and P-wave dominant period: the importance of length and depth of faulting, *Geophys. J. Int.*, 185, 283–291.
Lomax, A. & Michelini, A., 2013. Tsunami early warning within five minutes, *Pure Appl. Geophys.*, 170, 1385–1395.
Lomax, A., Michelini, A. & Piatanesi, A., 2007. An energy-duration procedure for rapid determination of earthquake magnitude and tsunamigenic potential, *Geophys. J. Int.*, 170, 1195–1209.
Madlazim, 2011. Toward Indonesian tsunami early warning system by using rapid rupture durations calculation, *Sci. Tsunami Hazards*, 30, 233–243.
Madlazim, 2013. Assessment of tsunami generation potential through rapid analysis of seismic parameters-case study: comparison of the sumatra earthquakes of 6 April and 25 October 2010, *Sci. Tsunami Hazards*, 32, 29–38.
Madlazim, Rohadi, S., Koesoema, S. & Meilianda, E., 2019. Development of tsunami early warning application four minutes after an earthquake., *Sci. Tsunami Hazards*, 38, 132–141.
Nakamura, Y., 1988. On the urgent earthquake detection and alarm system (UrEDAS), in *Proceedings of the 9th World Conference on Earthquake Engineering,* pp. 673–678, Tokyo-Kyoto.
Pelinovsky, E., Yuliadi, D., Prasetya, G. & Hidayat, R., 1997. The 1996 Sulawesi tsunami, *Nat. Hazards*, 16, 29–38.
Power, W., Clark, K., King, D.N., Borrero, J., Howarth, J., Lane, E.M., Goring, D., Goff, J., Chagué-Goff, C., Williams, J., Reid, C., Whittaker, C., Mueller, C., Williams, S., Hughes, M.W., Hoyle, J., Bind, J., Strong, D., Litchfield, N. & Benson, A., 2017. Tsunami runup and tide-gauge observations from the 14 November 2016 M7.8 Kaikōura earthquake, New Zealand, *Pure Appl. Geophys.*, 174, 2457–2473.
Prasetya, G.S., De Lange, W.P. & Healy, T.R., 2001. The makassar strait tsunamigenic region, Indonesia, *Nat. Hazards*, 24, 295–307.
Sepulveda, I., Haase, J.S., Liu, P.L.F., Xu, X. & Carvajal, M., 2018. On the contribution of co-seismic displacements to the 2018 Palu tsunami. In AGU Fall Meeting 2018. Available at: https://agu.confex.com/agu/fm18/meetingapp.cgi/Paper/476669, Accessed September 2019.
Socquet, A., Hollingsworth, J., Pathier, E. & Bouchon, M., 2019. Evidence of supershear during the 2018 magnitude 7.5 Palu earthquake from space geodesy, *Nat. Geosci.*, 12, 192–199.
Socquet, A., Simons, W., Vigny, C., McCaffrey, R., Subarya, C., Sarsito, D., Ambrosius, B. & Spakman, W., 2006. Microblock rotations and fault coupling in SE Asia triple junction (Sulawesi, Indonesia) from GPS and earthquake slip vector data, *J. Geophys. Res. Solid Earth*, 111, B08409.
Ulrich, T., Gabriel, A.-A., Ampuero, J.-P. & Xu, W., 2019a. Dynamic viability of the 2016 Mw 7.8 Kaikōura earthquake cascade on weak crustal faults, *Nat. Commun.*, 10, 1213.

Ulrich, T., Vater, S., Madden, E.H., Behrens, J., van Dinther, Y., van Zelst, I., Fielding, E.J., Liang, C. & Gabriel, A.A., 2019b. Coupled, physics-based modeling reveals earthquake displacements are critical to the 2018 Palu, sulawesi tsunami, *Pure Appl. Geophys.*, 176, 4069–4109.

USGS, 2018. Available at: https://earthquake.usgs.gov/earthquakes/eventpage/us1000h3p4/moment-tensor, Accessed September 2019.

Vackář, J., Burjánek, J., Gallovič, F., Zahradník, J. & Clinton, J., 2017. Bayesian ISOLA: new tool for automated centroid moment tensor inversion, *Geophys. J. Int.*, 210, 693–705.

van Dongeren, A., Vatvani, D. & van Ormondt, M., 2018. Simulation of 2018 tsunami along the coastal areas in the palu bay. In AGU fall meeting 2018. Available at: https://agu.confex.com/agu/fm18/meetingapp.cgi/Session/66627, Accessed September 2019.

Walpersdorf, A., Rangin, C. & Vigny, C., 1998. GPS compared to long-term geologic motion of the North arm of Sulawesi, *Earth Planet. Sci. Lett.*, 159, 47–55.

Ward, S.N., 2011. Encyclopedia of solid earth geophysics: tsunami, in *National Geophysical Research Institute (NGRI). Council of Scientific and Industrial Research (CSIR)*, pp. 1–1539, ed. Gupta, H. K. Springer Netherlands.

Watkinson, I.M. & Hall, R., 2017. Fault systems of the Eastern Indonesian triple junction: evaluation of quaternary activity and implications for seismic hazards, *Geol. Soc. Lond. Spec. Publ.*, 441, 71.

Wu, Y. & Kanamori, H., 2005. Experiment on an onsite early warning method for the taiwan early warning system, *Bull. Seismol. Soc. Am.*, 95, 347–353.

ISSN 8755-6839

SCIENCE OF TSUNAMI HAZARDS

Journal of Tsunami Society International

Volume 39 Number 4 2020

THE 25 MARCH 2020 TSUNAMI AT THE KURIL ISLANDS: ANALYSIS AND NUMERICAL SIMULATION

Andrey Zaytsev [1,2], Guney G. Dogan[3], Grigory Dolgikh[4], Stanislav Dolgikh[4], Ahmet C. Yalciner[3] and Efim Pelinovsky[2,5]

[1] *Special Research Bureau for Automation of Marine Researches, Yuzhno-Sakhalinsk, Russia*
[2] *Nizhny Novgorod State Technical University n.a. R.E. Alekseyev, Nizhny Novgorod, Russia*
[3] *Middle East Technical University, Ankara, Turkey*
[4] *V.I. Ilichev Pacific Oceanological Institute, Vladivostok, Russia*
[5] *Institute of Applied Physics, Nizhny Novgorod, Russia*

ABSTRACT

A strong earthquake with a magnitude of 7.5 occurred near the island of Paramushir (Kuril Islands) on 25 March 2020. It caused a weak tsunami in Kamchatka and the Kuril Islands. Earthquake and tsunami data from three DART buoys are discussed and compared with numerical simulations. It is shown that the calculated and measured tsunami characteristics on the DART buoys is in very good agreement. There are also data on the recording of this earthquake by a laser strain-meter installed in the Sea of Japan at Shults cape at a distance of more than 2,000 km from the epicenter of the earthquake. There is also an instrumental recording of the tsunami at the Vodopadnaya point in the southeast of Kamchatka. Unfortunately, there was a large storm at sea at this time, and the amplitudes of tsunami waves and storm waves were comparable to each other, so here the agreement between calculations and observations does not seem good enough.

Key words: *tsunami, numerical simulation, laser strain-meter, shallow-water equations, tsunami observations*

1. INTRODUCTION

On 25 March 2020, at 02:49 GMT (05:49 Moscow time), a strong earthquake occurred east of the Kuril Islands near Paramushir Island with M = 7.5. The epicenters of the earthquake and intensity contours on a 12-point scale are MSK-64 shown in Fig. 1. It caused a tsunami on a number of islands of the Kuril ridge and was also recorded by DART buoys (their locations are shown in Fig. 1). The earthquake was also recorded by laser strain-meters at Shults cape in the Sea of Japan (Figure 1), and the tsunami was instrumental at the Vodapadnaya station in southeast Kamchatka (Figure 1). The present work presents available data on earthquake and tsunami, as well as numerical simulation of the tsunami.

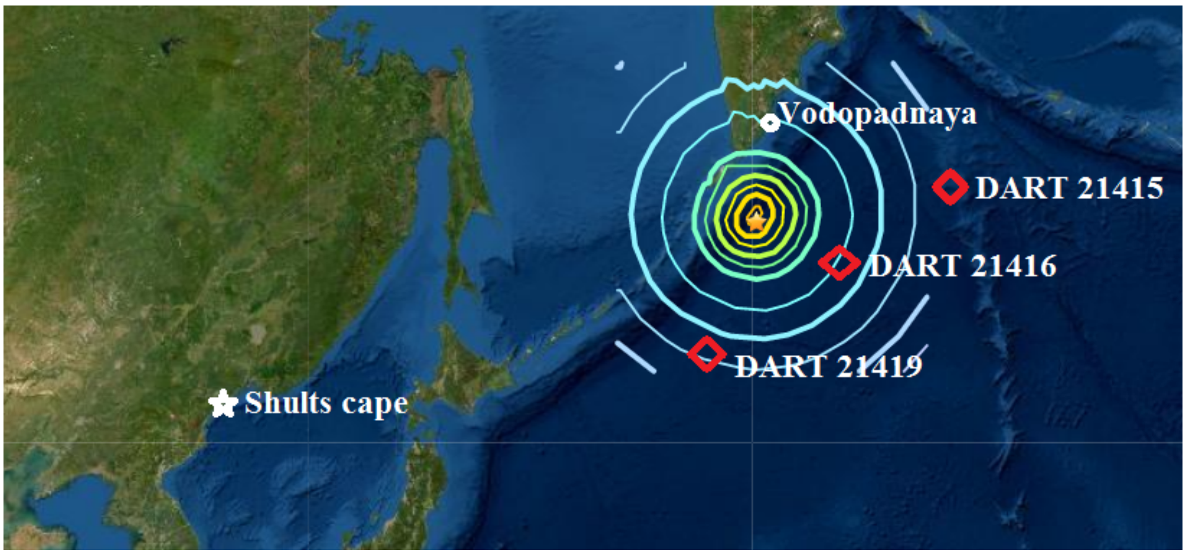

Fig. 1. The epicenter of the 25th March 2020 earthquake with intensity circuits, as well as the position of the DART buoys

It should be noted that catastrophic tsunamis previously occurred in this area, especially note the tsunami of November 4, 1952, which led to the death of several thousand people [Gordon A. Macdonald and Chester K. Wentworth, 1954]. In the north of the Kuril Islands and on the Kamchatka Peninsula, Chilean tsunamis of 1960, 2010 and 2015 were recorded [Liu et al, 1994]. Therefore, the analysis of developments in this area has an undeniable scientific and practical interest.

2. EARTHQUAKE AND TSUNAMI RECORDING

In Russia, earthquake parameters were determined in the Service of Urgent Reports (SSD) of the Federal Research Center "Unified Geophysical Service of the Russian Academy of Sciences" (FIC EGS RAS) in Obninsk using station data obtained from digital seismic stations of Russia, CIS countries and abroad [http://www.ceme.gsras.ru/cgi-bin/new/quake_stat.pl?sta=20201185&l=0] (USGS data will be listed in the next section.) An urgent message about this earthquake 11 minutes after its occurrence was transmitted to the operational duty officer of the Russian Emergencies Ministry. According to eyewitnesses [https://sakhalin.info/news/186919] in Severo-Kurilsk (Paramushir Island), the tsunami wave arrived at 15:15 local time (4:15 GMT); its height, determined visually, was about 50 cm. There were no casualties and destruction. According to information from the post of UGMS Sakhalin in the city of Severo-Kurilsk (Fr. Paramushir), the first tsunami wave arrived at 15:04 local time with a height of 40 cm. the second wave came after 50 minutes and a third wave arrived after another 60 minutes. It is worth noting that at this time, a cyclone passed over the region, and there was a storm at sea, but against the background of the storm, large waves stood out clearly, which everyone seemed to be a tsunami.

Instrumentally, waves were recorded at the Vodopadnaya sea level measurement station, the Russian Tsunami Warning Service. The station is located on the southeastern coast of the Kamchatka Peninsula and has coordinates: 51.833 °N., 158.067 °E [http ://rtws.ru/sea-level/vodopodnaya]. According to the analysis of the record, large waves that differ from background waves are observed 45 minutes after the earthquake, which coincides with the calculation results presented below (Figure 2).

Fig. 2 Record of tsunami waves (orange line) at the point "Vodopadnaya" station

The earthquake and the strain jump associated with the movements of the seabed in the center of tsunami formation were also recorded by a laser strain-meter installed at the marine experimental base of POI FEB RAS "C. Shults," at coordinates 42.58 N 131.157 E at a distance of almost 2150 km from the epicenter (Kuril Island). Figure 3 shows the processed recording of a laser strain-meter with a measuring length of 52.5 meters and a north-south orientation. To isolate variations in the micro deformations of the earth's crust caused by a tsunamigenic earthquake, variations in the micro deformations of the earth's crust caused by fluctuations in atmospheric pressure were subtracted from the laser strain-meter data, as described in [Dolgikh et al. 2020] Based on the experience of recording past earthquakes and tsunamis [Dolgikh et al. 2007, Zaytsev et al, 2019], it was possible to talk about a possible tsunami hazard. On the recording of the laser strain-meter, the earthquake was recorded at 02:53 GMT and after 4 minutes the beginning of the deformation anomaly that caused the tsunami was recorded. And already 15 minutes after the start of the earthquake, it was possible to talk about the occurrence of a tsunami.

Fluctuations of the bottom during the earthquake and tsunami were also recorded by the DART buoy system shown in Figure 1 (these records will be shown below compared to the results of the numerical simulation).

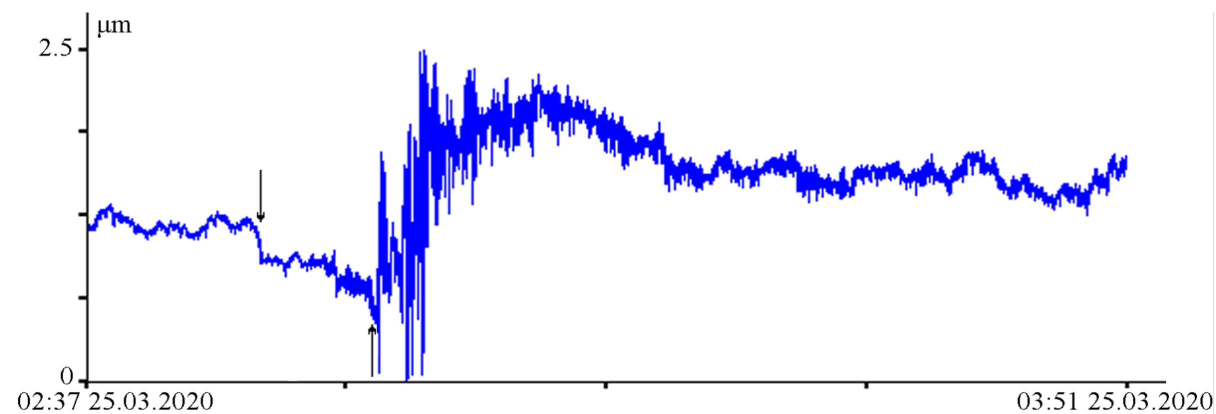

Fig. 3 Processed recording of laser strain-meter signal. The down arrow shows the time of the earthquake, the up arrow shows the registration of deformation movement, showing the beginning of tsunami

3. NUMERICAL TSUNAMI SIMULATION

To numerically simulate the tsunami on 25th March 2020, we used data from the US Geophysical Service [https://earthquake.usgs.gov/earthquakes/eventpage/us70008fi4/finite-fault]. The coordinates of the epicenter are 49.0°N, 157.7°E and the focal depth is 57 km. Figure 4 shows the surface projection of the sliding distribution superimposed on the GEBCO bathymetry. Thick white lines indicate the main boundaries of the plates [Bird, 2003]. The figure shows the shear distribution (slip) along the fault. As can be seen from Figure 4, this value varies from 1 to 4 m. In our calculations, we used the value of 2.5 m. The fault length is 80 km; the fault width is 30 km, the angle between the meridian and the fault line (strike angle) is 204 °, the angle of incidence (dip angle) is 48 ° and the angle of movement (rake angle) is 89 °.

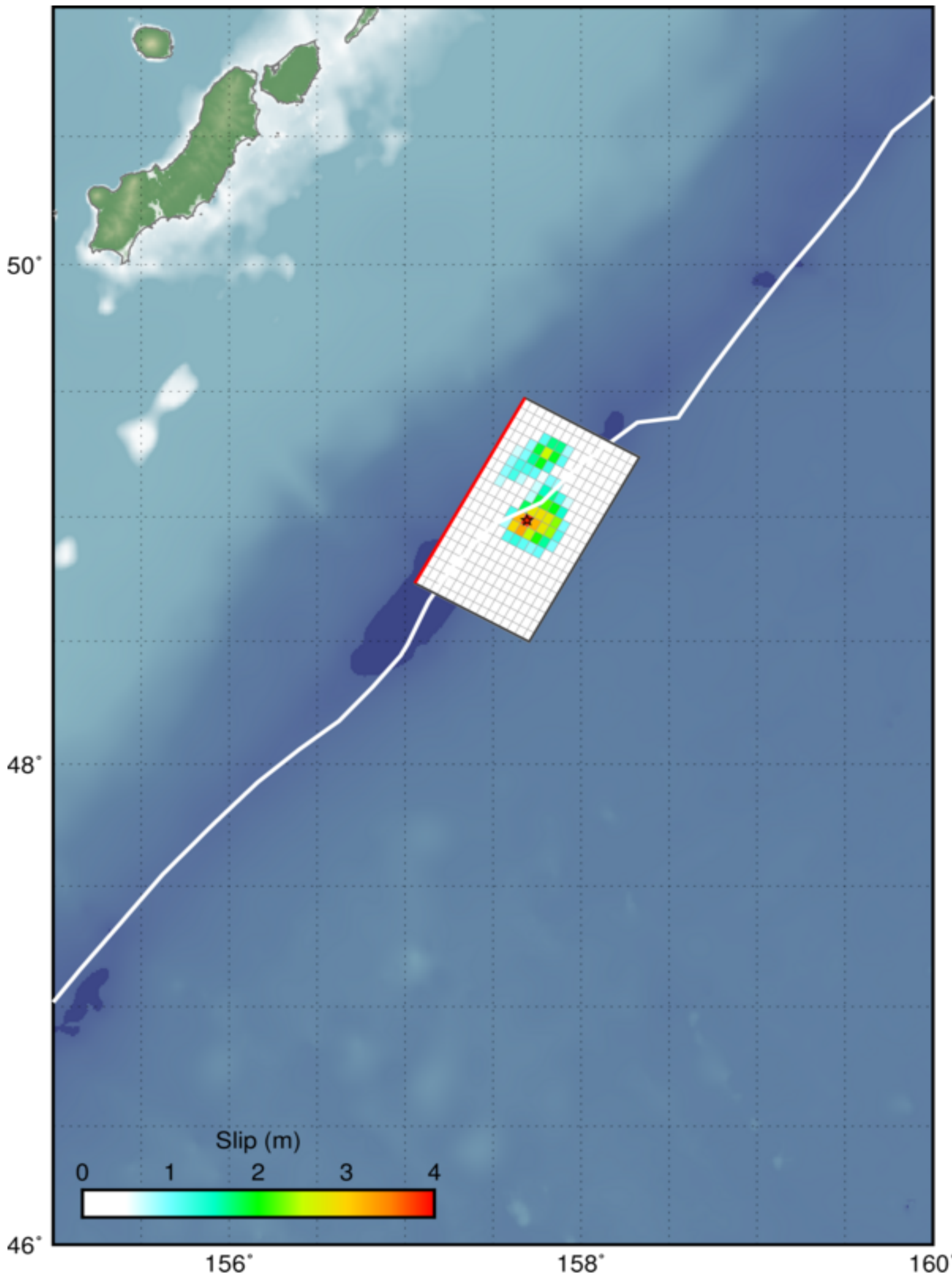

Fig. 4. Surface projection of sliding distribution superimposed on GEBCO bathymetry. Thick white lines indicate the main boundaries of the plates [Bird, 2003]. Gray circles, if any, are the locations of aftershocks

Using the available earthquake information, the initial displacement of sea level at the time of the earthquake is calculated according to the Okada formulas [Okada, 1985]. The maximum increase in the water level in the center is 25 cm and the decrease in the level is 4 cm. The propagation of tsunami waves was carried out using the NAMI-DANCE computational complex [Zaytsev et al. 2019; Zaytsev et al. 2016], solving the system of equations of shallow water in spherical coordinates on the rotating Earth taking into account the friction force.

$$\frac{\partial M}{\partial t}+\frac{1}{R\cos\theta}\frac{\partial}{\partial\lambda}\left(\frac{M^2}{D}\right)+\frac{1}{R\cos\theta}\frac{\partial}{\partial\theta}\left(\frac{MN\cos\theta}{D}\right)+\frac{gD}{R\cos\theta}\frac{\partial}{\partial\lambda}+$$
$$+\frac{gn^2}{D^{7/3}}M\sqrt{M^2+N^2}=fN, \tag{1}$$

$$\frac{\partial N}{\partial t}+\frac{1}{R\cos\theta}\frac{\partial}{\partial\lambda}\left(\frac{MN}{D}\right)+\frac{1}{R\cos\theta}\frac{\partial}{\partial\theta}\left(\frac{N^2\cos\theta}{D}\right)+\frac{gD}{R}\frac{\partial}{\partial\theta}+$$
$$+\frac{gn^2}{D^{7/3}}N\sqrt{M^2+N^2}=-fM, \tag{2}$$

$$\frac{\partial\eta}{\partial t}+\frac{1}{R\cos\theta}\left[\frac{\partial M}{\partial\lambda}+\frac{\partial}{\partial\theta}\left(N\cos\theta\right)\right]=0, \tag{3}$$

where η – the displacement of the water surface, t - time, M and N - the components of water flow along longitude λ, and latitude θ, f - the Coriolis parameter (f = 2Ω sin[theta]) and [omega] is the rotation speed of the Earth. (rotation period 24 hour), R - Earth radius, $D = h(x, y) + \eta$ – the total depth of the basin and h (x, y) is the unperturbed depth of the water, g is the gravitational constant, n is the roughness coefficient of the bottom (the so-called Manning formula). We took n = 0.015 m-1/3s, which is characteristic of the natural bottom (sand, fine pebbles).

For modeling, a bathymetry data, which was obtained from the 30-second bathymetry of the World Ocean (GEBCO30 Digital Atlas) including more accurate coastal bathymetry of the Kuril Islands, which was obtained from various sources of navigation charts, was used. The grid size used in the simulations is 500 m. Numerical modeling was carried out for 6 hours. Completely reflecting boundary conditions were adopted on the shore, and conditions for the free departure of waves on the morph. The distribution of the maximum wave amplitudes for the entire calculation time is shown in Figure 5. The main impact of the tsunami falls on the island of Paramushir.

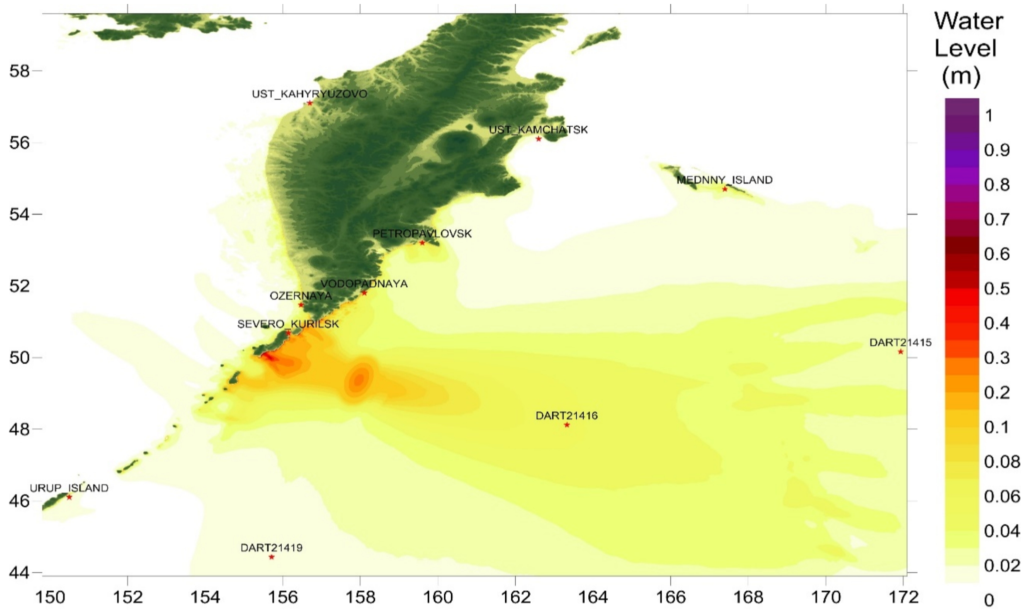

Fig. 5 Distribution of computed maximum water surface elevations during tsunami of 25th March 2020

The tsunami was recorded at several stations. The Deep Sea Tsunami Detection Station (DART 21415, Figure 1) with coordinates 50.164 N. 171.934 E. (50 ° 9 '51 "N 171 ° 56' 4" E), installed at a depth of 4811 m, first recorded an earthquake, and after 1 hour 10 minutes, a tsunami. Figure 6 shows the tsunami record and the results of the calculations of wave parameters at this point. The wave heights here are about 1.5 cm, and the period is about 30 minutes. Simulations results show good agreement with the real record.

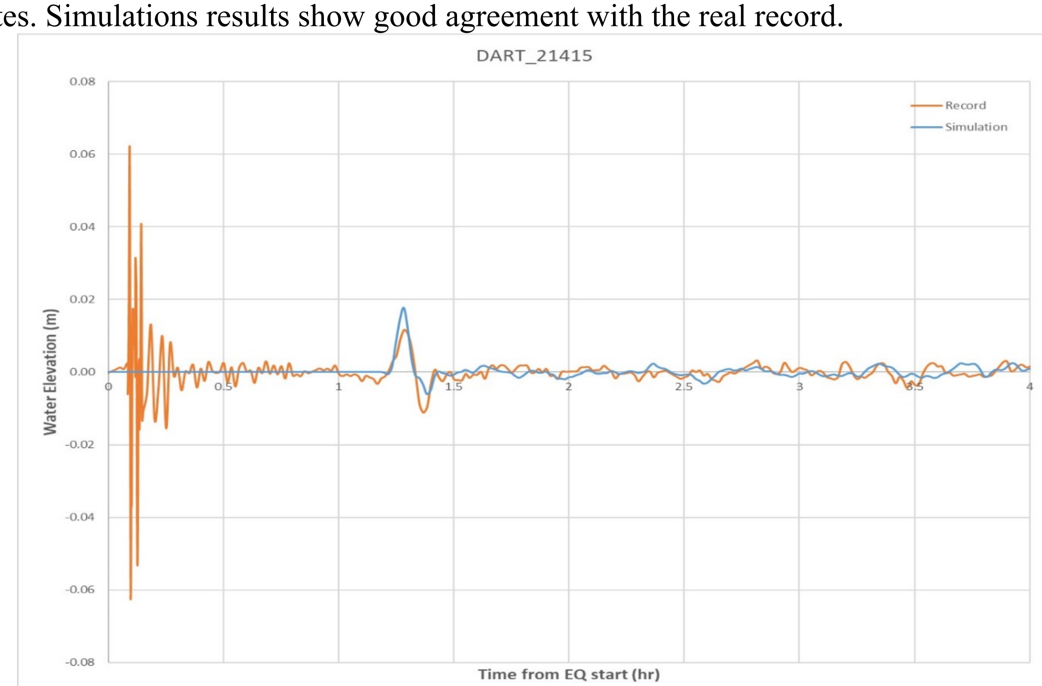

Fig. 6 Recording of tsunami wave 25th March 2020 and calculation results at DART 21415

The Deep Sea Tsunami Detection Station (DART 21416, Figure 1) with coordinates 48.122 N. 163.328 E. (48 ° 7 '18 "N 163 ° 19' 42" E), installed at a depth of 5831 m, and recorded a tsunami 25 minutes after the earthquake. Figure 7 shows the tsunami record and calculation results at this point. The maximum wave height is about 4.5 cm and a period of about 20 minutes. A good agreement of calculations with measurements is also obtained at this location.

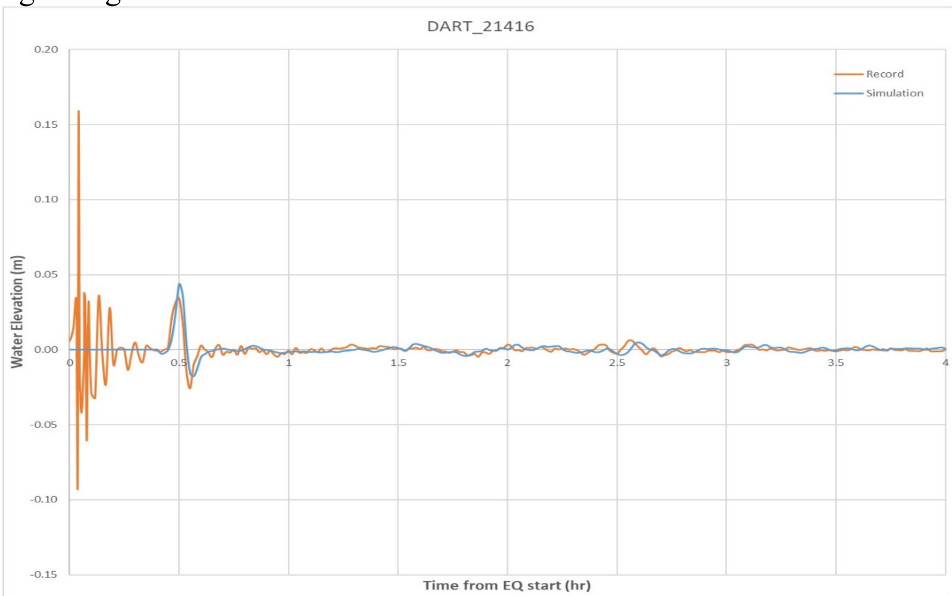

Fig. 7 Recording of tsunami wave 25th March 2020 and calculation results at DART 21416

The Deep Sea Tsunami Detection Station (DART 21419, Figure 1) with coordinates 44.435 N. 155.717 E (44 ° 26 '6 "N 155 ° 43' 0" E), installed at a depth of 5282 m, and recorded a tsunami 35 minutes after the earthquake noises remains unclear.

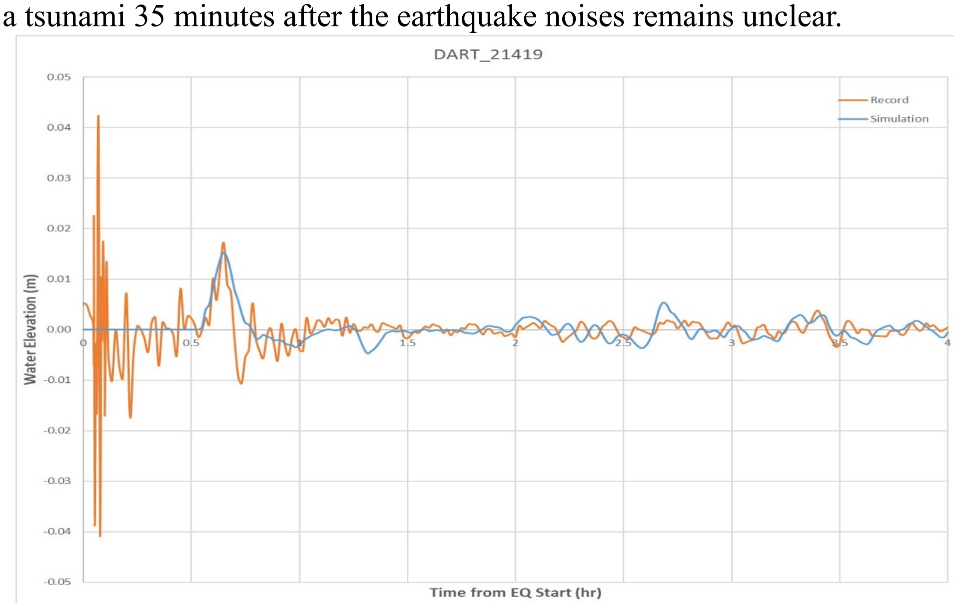

Fig. 8 Recording of tsunami wave 25th March 2020 and calculation results at DART 21419

Figure 8 shows the tsunami record and calculation results at this point. The maximum wave height is calculated as 1.6 cm and a period of about 35 minutes is obtained. Calculations show good agreement with the real record, which, however, is noisy, unlike records on other DART buoys.

Figure 9 shows the comparison of the calculation results with the tsunami record at the Vodopadnaya station). The agreement of these calculations with observations is not very good since, as already indicated, there was a storm at sea on this day, and the waves were significant. Relatively good agreement is observed for the first wave both in terms of arrival and in terms of wave height. A particularly large difference is observed 2.5 hours after the earthquake. The nature of such large waves can be related to both storm conditions and possible interference of tsunami waves arriving in the design area after reflection from the coast outside the design area. Currently, we do not have enough information to explain the appearance of large waves a few hours after the earthquake.

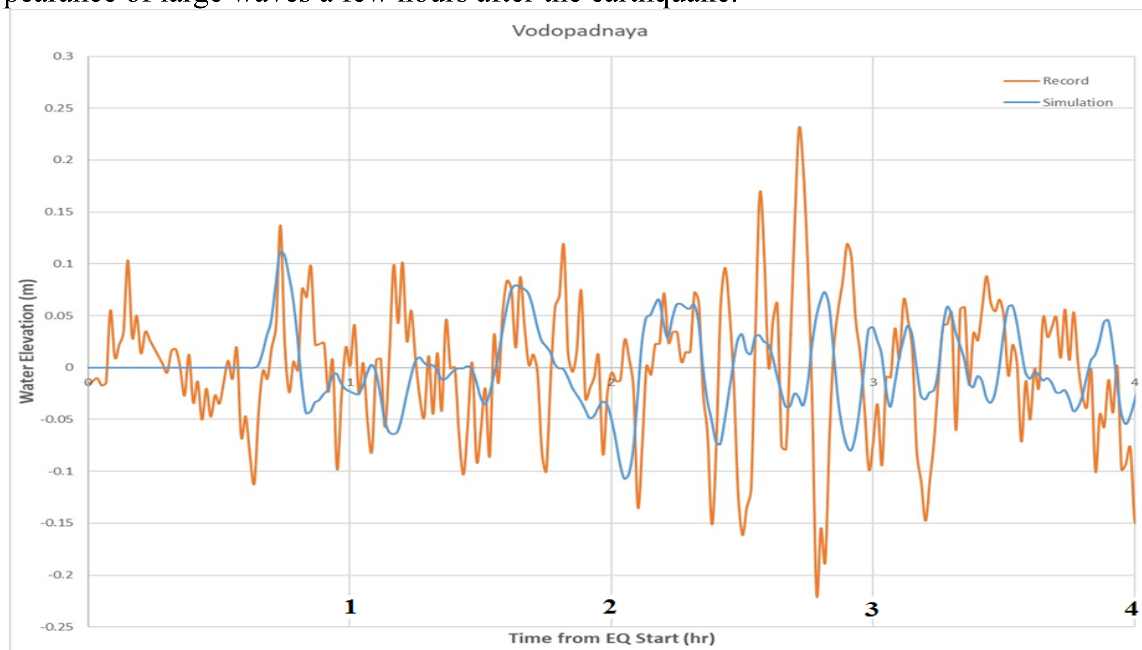

Fig. 9. Recording of tsunami waves (orange line) and calculation results (blue line) at the point "Vodopadnaya" station

4. CONCLUSIONS

On March 25, a strong earthquake with a magnitude of 7.5 near the island of Paramushir (Kuril Islands) caused a weak tsunami in Kamchatka and the Kuril Islands. The event was recorded by three DART buoys and a laser strain-meter installed in the Sea of Japan at Shults cape. We present the instrumental data on the recording of the earthquake and the tsunami. Using the shallow water theory, numerical modeling of the tsunami on 25th March 2020 was carried out. Comparison of the simulation results with tsunami records at deep-sea

DART stations show very good agreement. On the other hand, the agreement between the instrumental recording of the tsunami in the southeast of Kamchatka was not very good, since at that time, a storm raged at the sea, and storm waves were comparable to tsunami waves. Nevertheless, the arrival of the first tsunami wave is well reproduced in numerical modeling.

Acknowledgments

The work was partly supported by the subject "Study of the fundamental foundations of the origin, development, transformation and interaction of hydro acoustic, hydro physical and geophysical fields in the World Ocean", RFBR grants (18-05-80019, 19-55-15005, 20-05-00162) and the grant of the Russian President MD-148.2020.5

REFERENCES

1. **Bird P.** An updated digital model of plate boundaries Geochemistry *Geophysics Geosystems* 2003 Volume 4, 52 pages

2. **Dolgikh G.I., Dolgikh S.G., Kovalev S.N., Koren I.A., Ovcharenko V.V., Chupin V.A., Shvets V.A., Yakovenko S.V.** Recording of deformation anomaly of a tsunamigenous earthquake using a laser strain meter *Doklady Earth Sciences.* 2007. V. 412. № 1. P. 74-76

3. **Dolgikh G.I., Dolgikh S.G., Vasilevskaya L.N., Lisina I.A.** Interaction of the atmosphere and lithosphere in the minute range of periods *Doklady Earth Sciences.* 2020. V. 490. № 1. P. 18-22.

4. **Gordon A. Macdonald and Chester K. Wentworth** The tsunami of November 4, 1952, on the Island of Hawaii *Bulletin of the Seismological Society of America* (1954) 44 (3): 463–469.

5. **Liu, P. L.-F., Cho, Y.-S., Seo, S. N. and Yoon, S. B. (1994)** Numerical Simulation of Tsunami Propagation and Inundation with Application to Hilo, Hawaii, *Technical Report, School of Civil and Environmental Engineering, Cornell University.*

6. **Okada Y.** Simulated empirical law of coseismic crustal deformation Journal *of Physics of the Earth.* 1995. V. 43. P. 697 – 713.

7. **Zaytsev A., Kostenko I., Kurkin A., Pelinovsky E., Yalciner A.** The depth effect of earthquakes on tsunami heights in the Sea of Okhotsk *Turkish J. Earth Sci.* 2016. Vol. 25, N 4. P. 289–299.

8. **Zaytsev, A., Kurkin, A., Pelinovsky, E., Yalciner, A.C.** Numerical tsunami model NAMI-DANCE *Science of Tsunami Hazards.* 2019. V. 38, No. 4. P. 151–168.

9. **Zaytsev A.I., Pelinovsky E.N., Kurkin A.A., Pronin P.I., Yalciiner A., Dogan G., Susmoro H., Prasetya G., Hidayat R., Dolgikh G.I., Dolgikh S.G., Zahibo N.** Generation of the 2018 Tsunami on Sulawesi island: possible sources *Doklady Earth Sciences.* 2019. T. 486. № 1. C. 588-592.

ISSN 8755-6839

SCIENCE OF TSUNAMI HAZARDS

Journal of Tsunami Society International

Volume 39 Number 4 2020

EVALUATION OF THE IMPACT OF MAJOR EARTHQUAKES ON EXCITING LONG PERIOD FREE-EARTH LITHOSPHERIC OSCILLATIONS, ATMOSPHERIC-IONOSPHERIC PERTRUBATIONS, AND FAR-FIELD TSUNAMI-LIKE WATER LEVEL FLUCTUATIONS

George Pararas-Carayannis
Tsunami Society International

ABSTRACT

The whole Earth resonates like a bell with normal modes of resonance at distinct frequencies. When extremely large earthquakes strike, the Earth's free oscillations are excited. These excited, long period, enhanced earth oscillations have frequencies which have a tendency to resonate over long periods of time after a major earthquake. The Great Sumatra-Andaman Islands Earthquake of 26 December 2004 - the largest event in the last half century – was the first event in the Moment Magnitude (Mw 9) category to be recorded with modern digital instruments. The earthquake generated distinct stronger free oscillations of the Earth's lithosphere. Also, further coupling of these oscillations reportedly resulted in distinct atmospheric as well as ionospheric perturbations of certain modalities and frequencies. The present paper examines whether the excited stronger "spheroidal normal modes" of free earth oscillations could have contributed as well to tsunami generation enhancement, and to the lasting and persistent tidal oscillations that were recorded in the Andaman Sea and elsewhere. The present review further examines the efficiency of coupling of excited stronger solid free earth oscillations with the ocean, and analyzes whether these could have contributed significantly to the destructiveness of the tsunami that was observed in the Indian Ocean, or to unusual far-field water level fluctuations recorded by tide gauges in the Pacific and Atlantic Oceans – which cannot be supported by calculated tsunami travel times. Additionally to the 2004 event, other major earthquakes, volcanic and meteorological events are similarly examined as to their possible excitation of free Earth oscillations or coupling with the sea surface and the atmosphere, to generate far-field, tsunami-like sea level fluctuations or meteotsunamis.

Keywords: *Surface seismic waves; free earth oscillations; Tsunamis, Earthquake source observations; 26 December 2004 earthquake; spheroidal, Toroidal modes; Rayleigh & Love Wave Interactions*

1. INTRODUCTION

The Earth is not a perfect sphere. Beneath and above its surface, the distribution of rock and mineral formations is uneven, thus causing pockets of varying density and therefore of gravity. Also, near the equator, the earth's spinning rotation creates a bulge, thus raising its surface and resulting in a decrease in the pull of gravity, while near the north and southern poles the gravitational acceleration is highest. Also, in certain regions where tectonic plates move apart, the earth's crust is not as thick and gravity is weaker. Finally, large surface features on the earth's surface such as mountain ranges increase the force of gravity. NASA satellites probing and measuring the Earth's gravity when they approach regions of higher density are pulled forward, at slightly higher speed and slow down somewhat when they reach regions of lesser crustal density.

Furthermore, Planet Earth can be considered to be a mechanical system with a finite body of mass. All mechanical systems possess natural vibrations that can be excited by internal or external forces. Researchers at UC Santa Barbara and Tokyo Institute of Technology have determined that the Earth vibrates continuously and suspect atmospheric turbulence as the cause of tiny spheroidal waves (Tanimoto et.al., 1990; Tanimoto, 2001). However, when a large earthquake occurs, different seismic phases are generated which propagate away from the source region, through and around the earth. Typical periods for compressional P- and shear S-waves are of the order of a few seconds, while the surface seismic waves have longer periods.

Often, these seismic phases interfere both constructively and destructively with each other in a resonant way, so that their arrival and graphic and digital signatures at different seismic stations may vary significantly. Additionally, when large earthquakes strike, the Earth's free oscillations are excited - thus the whole Earth resonates like a bell with normal modes of resonance at distinct frequencies. These self-excited, long period, free earth oscillations have frequencies which have a tendency to resonate over long periods of time after a major earthquake. To understand how the earth's natural vibrations are being excited and enhanced by earthquakes, we need to review some of the progressive historical developments that have taken place in the field of seismology.

The history of studies relating to seismic waves goes back to Poisson in 1829 (Poisson, 1829) and Lamb in 1882 (Lamb, 1982). Studies of seismic surface waves begun with Rayleigh in 1885 and with Love in 1911 (Love, 1911). Such early studies helped determine the Earth's upper-mantle structure and rheological heterogeneity. Most of our subsequent understanding about the Earth's interior has come from the application of the ray-theoretic methods to seismological data. Ray theory is useful for periods shorter than a minute. Travel-times of seismic phases constitute an important component of the ray theory concept. However, before reviewing the enhancement of the long period free-earth oscillations caused by large earthquakes and their coupling with the atmosphere and ionosphere, or with the seas and oceans in increasing near-field tsunami heights or far-field tsunami-like wave activity observations or measurements, we need to also review briefly the earlier pioneering research in seismology that has further increased our understanding of the earth's near surface and internal structure (Pararas-Carayannis, 2000a, 2000b; 2000c). The following section pertains to a brief review of such early studies and of research in seismology that led to the understanding of tectonic interactions and crustal displacements and perturbations responsible for tsunami generation mechanisms, as well to far-field tsunami-like sea level fluctuations that cannot be supported by normal wave refraction and tsunami travel times.

Also, the present study is a preliminary evaluation on whether great earthquakes such as the 26 December 2004 Sumatra Earthquake, or other events of large magnitude, affect the earth's free oscillations, and whether they contribute to the enhancemnet of near-field generation of the destructive tsunami waves that were observed in the Indian Ocean and adjacent seas, or to the unusual far-field water level fluctuations recorded by tide gauges in both the Pacific and the Atlantic Oceans, which do not conform with tsunami travel times based on wave refraction and ocean bathymentry. In addition, the present study provides a brief review of the Earth's free modes of natural oscillations and of their excitment by major or great tsunamigenic earthquakes.

2. EARLY HISTORY OF PIONEERING RESEARCH IN SEISMOLOGY

Although earthquakes from the beginning plagued humanity and millions of lives were lost, the causes of earthquakes were not studied systematically until the 19th Century. A book addressing seismic hazards was written by an Irish Engineer, Robert Mallet and was entitled, "The Great Neapolitan Earthquake of 1857". The first book on "Principles of Observational Seismology", which resulted from his investigation of this particular earthquake, was a milestone in the evolution of seismology.

The subsequent history of evolution of seismology is quite interesting. Mallet and his contemporary Englishman, John Milne, were the pioneers of such research (Mair, 2013). However Milne is considered to be the father of seismology because he made a remarkable impact on the study of earthquakes by designing and constructing earthquake measuring devices and by collecting and publishing earthquake data and maps of worldwide earthquake distribution. This early data formed the basis for the initial understanding of earthquakes and for measuring important seismic parameters.

The early history of pioneering research in seismology is extensively documented in the scientific literature and in a summary of a previous issue of "Science of Tsunami Hazards" (Pararas-Carayannis, 2000c). This report mentions that the first seismographs in the United States were installed in 1887 at the Berkeley campus of the University of California and at the Lick Observatory at Mount Hamilton, California. Prior to the great San Francisco earthquake of 1906, earthquake research in U.S.A. had advanced very slowly compared to efforts in Japan and Europe. However, around the turn of the century, a small number of U.S. Geological Survey scientists and geology professors at a few U.S. universities, begun to contribute earthquake data and to compile lists of historic earthquakes in the U.S. and around the world. At that time, and in spite of the earlier work in Japan and Europe, still very little was known about earthquakes, how and where they occurred, or the risks they presented. The modern theory of plate tectonics had not yet been proposed and was still years away. Nothing was known about the Earth's free oscillations or their excitement by earthquakes, or the mechanisms of tsunami generation, in general.

The great 1906 San Francisco earthquake was a major event that triggered the interest of many scientists and resulted in numerous scientific investigations. Comprehensive studies of this earthquake and of the San Andreas fault-system in California marked the beginning of modern seismology in the U.S.A. and the understanding of the earth's internal structure. According to the historical record, the exhaustive investigation and surveys of the 1906 San Francisco earthquake illustrated the importance of collecting valid, extensive, and repetitive data on earthquakes, their effects, and on the faults on which they occur. These comprehensive studies of this particular earthquake - formed the basis for the understanding of earthquakes in California and elsewhere in the USA and around the world.

A final report on the great San Francisco earthquake - often referred to as the Lawson report - was published in 1908. The report was a comprehensive compilation of detailed studies by more than twenty scientists on the 1906 earthquake's damage, intensities, the slip movement along the San Andreas Fault, the seismograph records of the earthquake from around the world, and the underlying geology in northern California. One of the scientists was Henry Reid, a professor of Geology at Johns Hopkins University. Professor Reid examined extensively the ground displacements of the 1906 earthquake on the San Andreas fault. Based on his observations he reached the conclusion that this earthquake must have involved stored energy and accumulated stress, which was suddenly released, thus he proposed the "elastic rebound theory" of earthquakes. His concept of elasticity continues to influence today's scientific thinking about earthquakes (Pararas-Carayannis, 2000a).

3. EARLY STUDIES OF THE EARTH'S SEISMICITY - INTERACTIONS OF SURFACE SEISMIC WAVES WITH THE LITHOSPHERE, HYDROSPHERE, ATMOSPHERE, IONOSPHERE AND ENHANCEMENT OF FREE-EARTH OSCILATIONS.

As stated above, the earlier studies of the earth's seismicity were initiated by S.D. Poisson (Poisson, 1829), by Mallet and Milne in 1857 (the two founding fathers of engineering seismology)(Mair, 2013), by Horace Lamb (Lamb,1882) on vibrations of an elastic sphere (Ewing et.al 1957; Feynman, 1963), by Rayleigh in 1885 on seismic waves propagated along the plane surface of an elastic solid known as "Rayleigh waves", and by A.E.H. Love (Love, 1911 a,b), who developed a mathematical model of surface seismic waves, known as "Love Waves". Both types of surface seismic waves known as "Rayleigh" and "Love" can be damaging to structures, but particularly the "Love" waves that result in horizontal accelerations. However, none of these earlier studies correlated surface or deeper seismic motions of earthquakes as contributing to the earth's free oscillations.

To help understand the excitation of free Earth oscillations – which are standing waves - mainly by the surface seismic waves or by their combined coupling with the sea surface and the atmosphere, to generate near-field or far-field, tsunami-like sea level fluctuations or meteotsunamis, the following section provides a brief review of their interactions of both "Rayleigh" and "Love" waves. These interactions may be further influenced by sea tides, and "spring tides", depending on the moon's urnal and di-urnal position and on its gravitational alignment with other celestial bodies.

3.1 “Rayleigh” Wave Interactions

The “Rayleigh” waves are known to cause both vertical and horizontal ground motions. These waves are more pronounced near the earth’s surface and as they propagate, they lift and drop the ground and also move it horizontally. Their stress occurs mainly on the vertical plane (Fig. 1). Because of the vertical motions and coupling with the lithosphere, the hydrosphere, the atmopshere and the ionosphere, the Rayleigh waves can result in oscillations in these regimes and may have an exciting effect on the free earth oscillations and may be responsible in somewhat enhancing the oberved far-field tsunami-like waves – the travel times of which cannot be supported by tsunami propagation based on the shallow water wave-equations. The following is a brief description of the motions on the surface of the earth caused by “Rayleigh” wave (Fig 1).

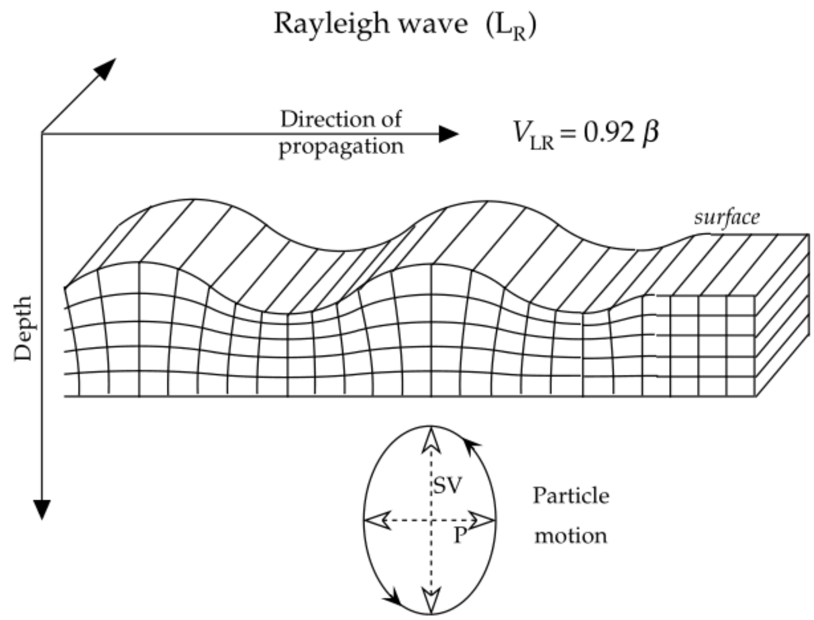

Fig. 1. Diagram of “Rayleigh” wave propagation on the surface of the earth. The resulting motions include both longitudinal and traverse motions that decrease exponentially as the distance from the surface increases. The waves are more pronounced near the surface and their stress occurs mainly on a vertical plane.

Since Rayleigh waves from large earthquakes involve vertical motions, research results on delayed ionospheric oscillations of Rayleigh waves from large earthquakes, could be detected and recorded by high-frequency Doppler sounding techniques (Furumoto, 1970). To illustrate such coupling with both the atmosphere and the ionosphere, this particular study used the 10 MHz recording of Rayleigh waves to estimate the initial phase of the source of the Kuril earthquake of 11 August 1969. From such recordings also of ionospheric perturbations, the initial motion from this quake appeared to be downward and, because of the rapidity of such recording, this approach to tsunami source mechanism estimation was considered to be a useful indicator of potential tsunamigenesis, and thus was recommended for use by the Pacific Tsunami Warning System (PTWC) (Pararas- Carayannis, 2000 a, b, c).

3.2 "Love" Wave Interactions

In contrast, the "Love" waves travel without vertical displacement and they move the ground from side to side in a horizontal plane, but at right angles to the direction of propagation. "Love" waves are known to be particularly damaging to the foundations of structures because of the horizontal ground motions they generate and the horizontal shearing of the ground (Fig. 2). The waves are more pronounced near the surface and their stress occurs mainly on a horizontal plane. The resulting motions include lateral ground motions and also decrease exponentially as the distance from the surface increases. Although the "Love" waves do not contribute directly to tsunami wave heights, the horizontal stresses and particle motions they cause may result in bookshelf type of failures of sedimentary structures near a tsunami generating area and thus contribute to the enhancement of tsunami heights. Such was the case with the great 2011 Tohoku-Oki earthquake in Japan (Pararas-Carayannis, 2011).

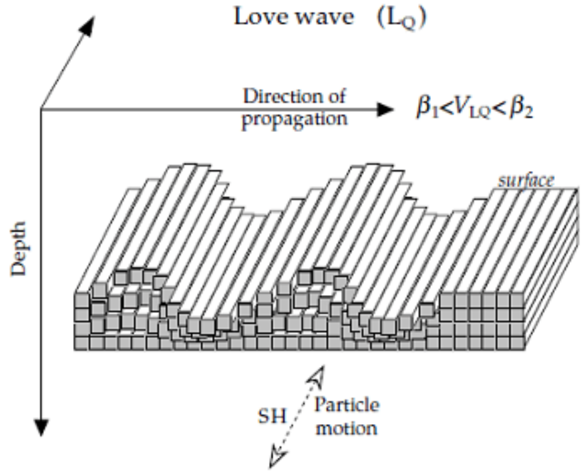

Fig. 2. Diagram of "Love" wave propagation on the surface of the earth.

3.3 Modes of the Earth's Free Oscillations

Large earthquakes generate two distinct types of free modes of natural oscillations (standing waves) in the Earth – the spheroidal which are equivalent to the Rayleigh Waves, and the toroidal which are equivalent to the Love waves. The spheroidal mode, has two sub-classifications and the toroidal has three. Both types of oscillations have an infinite number of modes (Ben-Menahem, 1964; Brune, 1964; Buland, 1964,1981; Dahlen, 1968, Dahlen & Sailor, 1979; Dahlen & Tromp, 1998; Geller & Stein, 1979). Free oscillations have relatively long periods of hours to days. In the present study, we refer only to the earth's free oscillations modes of only certain frequencies that are excited by major or great earthquakes.

4. BASIC MOTIONS OF THE EARTH'S FREE OSCILLATION MODES

The influence of gravity on the vibrations of an elastic globe were studied as early as 1898 (Bromwich, 1898) and by many more researchers in later years (Dahlen & Smith, 1975; Woodhouse & Dahlen, 1978; Valette, 1986; Woodhouse, 2008). The normal free oscillations of the Earth were extensively studied by numerous other researchers following the 1964 Chilean Earthquake, the largest tsunamigenic event in recorded history (Brune, 1964; Ben-Menahem, 1964; Dahlen, 1968; Buland, 1981; Park Et Al, 2005; He & Tromp, 1996; Lognonné & Clévédé, 2002).

As described in the scientific literature, the basic motions of the Earth's free oscillations can be illustrated with the following diagram of the spheroidal (radial and tangential (football)) and toroidal modes (Fig. 3).

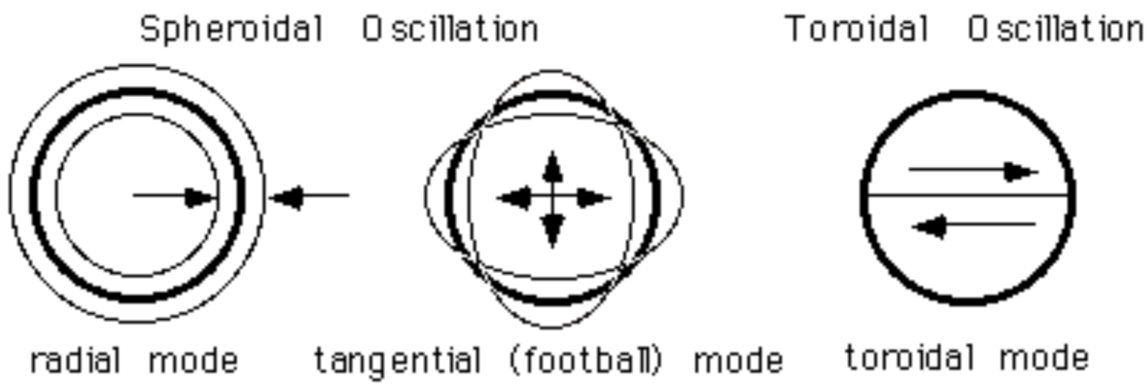

Fig. 3. Spheroidal and Toroidal Free Earth Oscillations

4.1 Long-period Toroidal oscillations (T)

The toriodal oscillations involve shear motions parallel to the surface of the earth and are not as significant as the spheroidal modes. Relative displacement motion for toroidal oscillations is always perpendicular to the radius vector. These oscillations involve only the earth's crust and mantle. They are equivalent to the Love waves.

4.2 Long-period Spheroidal oscillations (S)

The displacement for spheroidal oscillations has both radial and tangential components. They are equivalent to the Rayleigh waves. The most important of the Earth's "spheroidal normal mode" is the so called "football" or "rugby" mode, abbreviated as OS2. It has a 53.8 minute period or 0.31 mHz frequency. Another spheroidal normal mode of motion - also with a radial component - is the "balloon' or "breathing" mode, abbreviated as OS0. It has a 20.6 minute period or 0.81 mHz frequency. The third of the spheroidal modes is the OS3 with a period of 35.5 minutes or 0.47 mHz frequency.

4.3 Tiny Natural Earth Vibrations Generation by Atmospheric Turbulence

For the purpose of determining the Earth's natural oscillation modes, scientists from the University of California at Santa Barbara and from the Tokyo Institute of Technology, analyzed gravimeter data from 1983 to 1994 and found 61 days to be seismically "quiet". For this period of time, they identified several such natural modes in the range of 2 to 7 milli-Hz – which were very small vibrations with periods of hundreds of seconds. The acceleration of material in the solid Earth which were produced by these spheroidal waves was only in the the order of nano-gals, or 10^-9 cm/sec^2 thus suspecting that the cause of the tiny vibrations resulted by atmospheric turbulence. (Tanimoto et al., Geophysical Research Lett., May 15; toshiro@magic.geol.ucsb.edu)

4.4 Impact of Major Earthquakes on Long Period Free-Earth Oscilations on the Lithosphere

Subsequent studies of the normal-mode theory on the free Earth's oscillations are based on the geometrical ray theory of optics (Singh & Rani 2011). This particular approach views these oscillations as standing waves rather than traveling waves, and their peaks are identifiable in the amplitude spectrum of a seismogram.

Theoretically, the free oscillations from an arbitrary earthquake source can be derived by solving the governing radial differential equations of motion and correlating the earth's elastic-gravitational response, which can be expressed as a sum of such free oscillations or normal modes. The same methodology can be used to calculate synthetic seismograms on a spherical earth by normal mode summation, and interpret the propagation of Love and Rayleigh waves and mode-ray duality. However, such a theoretical solution requires many assumptions as to the Earth's sphericity, rotation and rheological homogeneity. Since the Earth is neither homogeneous nor completely spherical, the calculated modes will differ from what actually occurs when a large earthquake strikes – as discussed in the following section.

5. EXCITMENT BY EARTHQUAKES OF THE EARTH'S FREE OSCILLATIONS

Planet Earth vibrates continuously even in the absence of earthquake activity. The Earth's free oscillations were observed for the first time in the early 1960's. The systematic study of the earth's free oscillations begun after the Great Chilean earthquake of 22 May 1960 - the largest during the 20th Century. Since then, the earth's free oscillations and their excitment by earthquakes have been extensively studied by many researchers. As mentioned, such studies determined two distinct types of free modes of natural oscillations – the spheroidal, which are equivalent to the Rayleigh waves, and the toroidal, which are equivalent to the Love waves. The spheroidal mode has two sub-classifications and the toroidal has three. Both types of free coscillations have an infinite number of modes. This occurs because the Earth is spherically asymmetric and has lateral heterogeneities within it. Furthermore, the influence of its rotation splits the modes. However, at the very low frequency range (below 10 mHz), which has been used extensively in the last 40 to 50 years, the free oscillations can be observed and provide valuable information on the whole Earth (Montagner & Roult, 2004).

The earth's free oscillations have relatively long periods of hours to days. These modes are excited and altered by earthquakes. As mentionrd, normal modes have been used to calculate accurate synthetic seismograms and derive the centroid moment tensor of earthquakes. Also, the relative excitement of ultra-long period spheroidal oscillations has been used to calculate more accurately the energy and moment magnitude of great earthquakes. For example, the Kamchatka Earthquake of 1952 had a 57 min fundamental mode. The following section pertains to recent major or great earthquakes. The relative excitment of certain modes of spheroidal oscillations were used by some researchers in calculating more accurately the energy release and moment magnitudes of some of the recent strong earthquakes – particularly of the 9 June 1994 om Bolivia and of the 26 December 2004 in Indonesia.

5.1 The 9 June 1994 Earthquake in Bolivia

The 9 June 1994 earthquake in Bolivia was unique in the sense that it was unusually strong, had a focal depth of 636 kilometers and a rapid rupture rate which ranged from 1 to 3 km/second (Silver EtAl, 1995).

Based on analysis of IRIS broad-band seismograms for this earthquake and by inversion of the sections with duration of 330 seconds which included several phases of refracted compressional P-waves and Raleigh as well as Love waves – the latter with duration of long period (175 to 250 seconds) - the dip-slip mechanism for this quake and its scalar moments were determined, both agreeing and corresponding to a moment magnitude Mw=8.3 (Kikuchi & Kanamori, 1994).

5.2 The 26 December 2004 Earthquake

The Great Sumatra-Andaman Islands Earthquake of 26 December 2004 - the largest event in a last half century - was the first event in the Moment Magnitude (Mw 9) category to be recorded with modern digital instruments. This earthquake generated distinct strong free oscillations of the Earth's lithosphere. Also, further coupling of these oscillations resulted in atmospheric as well as ionospheric perturbations of certain modalities and frequencies.

This earthquake was extensively studied and reviewed in the scientific literature (Montagner & Roult, 2004; Kayal & Wald, 2004; Stein and Ocal, 2005; Pararas-Carayannis, 2005; Gower, 2005). Based on the history of past earthquake events and a clearly identifiable seismic gap along western Sumatra (see Fig. 4 below), the occurence of this great earthquake was predicted as early as 1989 and included in a report to the United Nations Development Program (UNDP) (Pararas-Carayannis, 1989 a; 1989 b).

With the sponsorship and coordination of UNESCO-Intergovernemental Oceanographic Commission, UNDP sponsored and funded a field investigation and subsequently approved the proposed plan (Pararas-Carayannis, 1989a). This report recommended specificaly a five year plan of action designed to mitigate the impact of the pending disaster with the installation of monitoring instrumentation and the establishement of a Regional Tsunami Warning System that could provide timely warnings for the countries bordering the Indian Ocean.

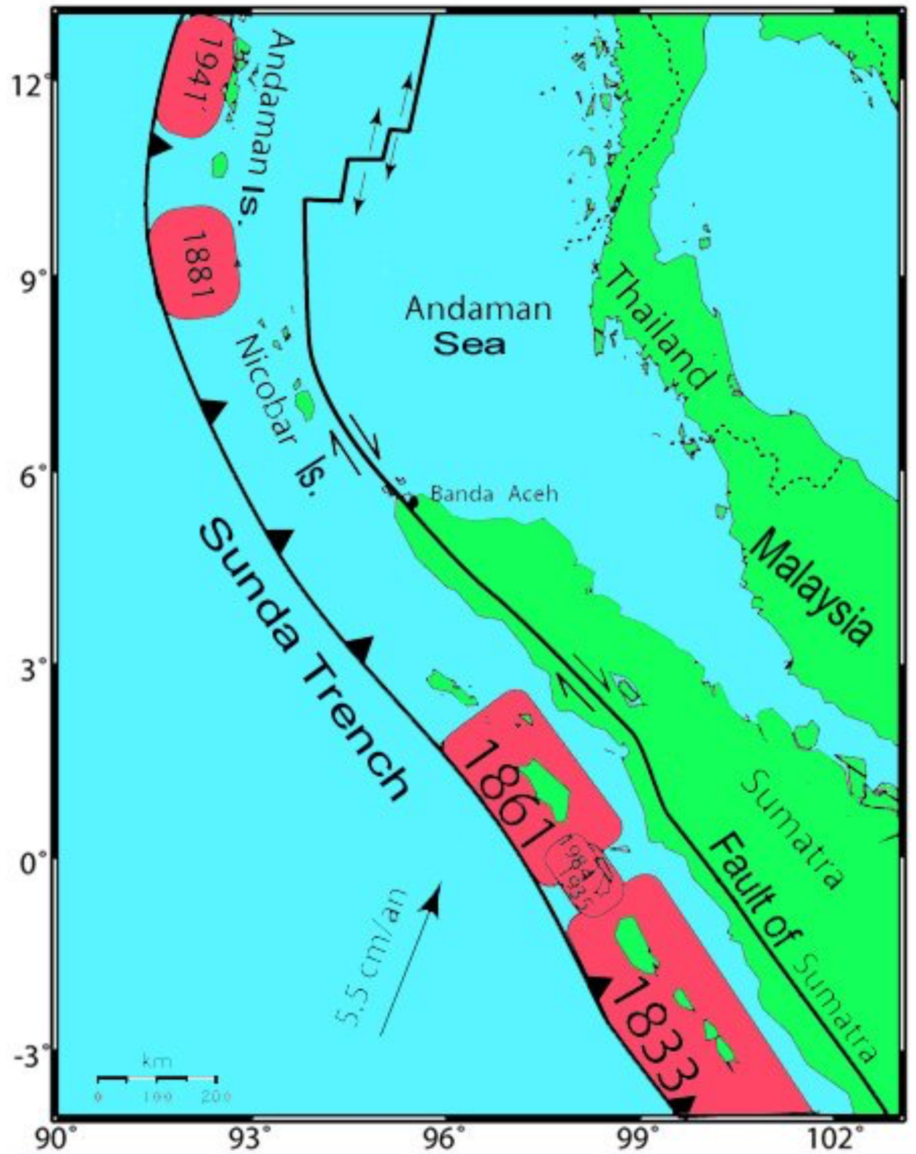

Fig. 4. Identifiable seismic gap along western Sumatra
After http://www.drgeorgepc.com/Tsunami2004Indonesia.html

The anticipated great earthquake finally occurred a few years later on 26 December 2004 along the indicated seismic gap as shown in Figure 5, but included an extention to the Nicobar and Andaman Islands, the segments that ruptured by earthquakes in 1881 and 1941.

5.2a Spheroidal and Toroidal Modes of the 26 December 2004 Earthquake

From a technical point of view, this earthquake provided high-quality seismic data which was recorded by the broad-band stations of the Federation of Digital Seismograph Networks (FDSN). These recordings made it possible to observe a very large collection of split modes, not only of the spheroidal but also of the toroidal modes (Montagner & Roult, 2004; Stein and Okal, 2005; **http://www.iris.iris.edu/sumatra/).**

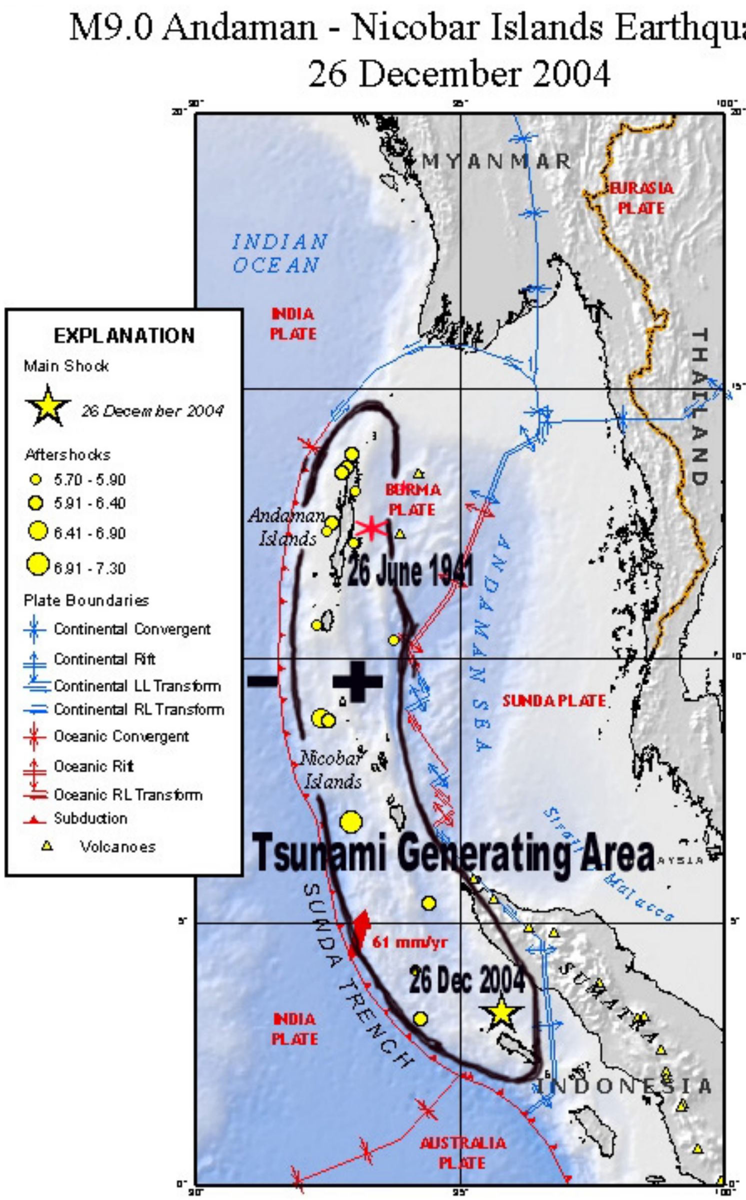

Fig. 5 Tsunami Generating Area of the 26 December 2005 Earthquake (After http://www.drgeorgepc.com/Tsunami2004Indonesia.html - Modified USGS map showing the earthquake epicenter, the distribution of initial major aftershocks, and the interaction of major tectonic plates along the Sunda Trench)

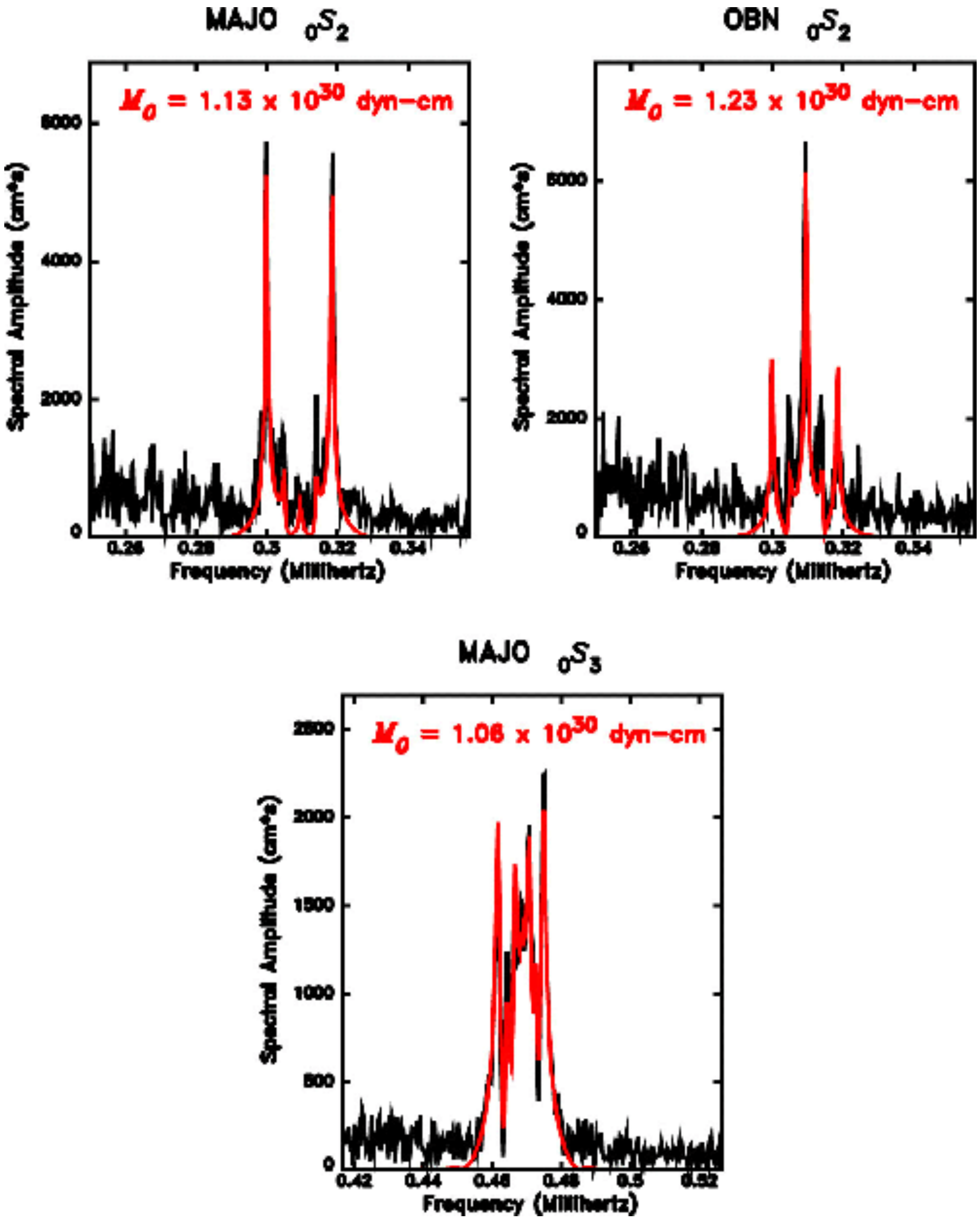

Fig. 6. Analysis of the longest period normal modes of the earth, OS2 and OS3, of the 26 December 2004 earthquake, yielded a greater moment magnitude Mw = 9.3 rather than the Mw = 9.0 that was initially measured from long period surface waves (source: http://www.iris.iris.edu/sumatra/ Credit**:** Seth Stein and Emile Okal, Department of Geological Sciences, Northwestern University)

Another study used the relative excitement of ultra-long period spheroidal oscillations to calculate more accurately the energy and moment magnitude of this event. In fact, analysis of the longest period normal modes of the earth – the OS2 and OS3 – were used to calculate its energy release and moment magnitude. Based on Fourier analysis of long seismograms and further analysis of normal mode multiplets of the 0S2 and 0S3 spheroidals with periods of about 3,231 seconds (53.85 min.) and 2,134 seconds (35.5667 min), the Moment of the December 26, 2004 Sumatra earthquake was determined to be 1.3 x 10^{30} dyn-cm. (Stein and Okal, 2005). This was approximately three times larger than the 4 x 10^{29} dyn-cm that had been measured from long period surface waves (see Fig. 6 above). Analogous re-evaluations of other major or great historical earthquakes can be expected to result in greater estimates of Mw magnitudes, than those conventionally calculated and reported.

Hence, the 2004 earthquake's ultra-long period magnitude, was re-evaluated to be Mw = 9.3, which was significantly greater than the previously estimated Moment Magnitude Mw = 9.0. – making this earthquake the second largest ever instrumentally recorded.

Even with the initially lower Moment Magnitude of MW = 9.0 estimate, the scale of motion was particularly unique and remarkable for seismic recordings. In terms of units of displacement, the peak-to-peak ground motions observed globally were greater than one centimeter for the long oscillations (100+sec) of the Love (G) and Rayleigh (R) surface waves.

5.3 The 11 March 2011 Earthquake in Japan

The great Tohoku-Oki earthquake (Mw 9.0) of 11 March 2011 off the Pacific coast of Honshu Island in Japan was a megathrust event which produced displacement of at least 40 m.. was extremely destructive and generated a very destructive and anomalously high tsunami. Prior tsunamigenic earthquakes in this region occurred in 1611, 1896 and 1933. The 1896 Meiji-Sanriku earthquake was also a megathrust event which generated a destructive tsunami (Tanioka & Seno, 2001). The 1933 Sanriku-oki earthquake was also very destructive, and generated tsunami waves with heights ranging from 10 to 25 meters along the coast of Iwate perfecture of Honshu Island. Critical reviews and evaluations of historical events in Japan, as well as that of that of 11 March 2011 were undertaken by many researchers (Iida et al, 1967; Kanamori, 1971; Ammon et al., 2011; Koper et al 2011; Pararas-Carayannis 2011; Lay et al, 2011 a & b).

5.3a Review of Geotectonic Changes Associated with the 2011 Earthquake

Research on geotectonic changes indicates that the landmass of Honshu Island moved in an east-southeasterly direction, opposite to the direction of the under-thrusting forces. (Fig. 7).

Based on the Global Positioning System, the Geospatial Information Authority in Tsukuba, Japan, estimated that the Oshika Peninsula near the epicenter area moved by a little over 5 meters (17 feet) eastward and subsided by a little over 1 meter (4 feet). Additionally, the Geospatial Information Authority stated that there were land mass movements in many areas of Honshu, from the northeastern region of Tohoku to the Kanto region, including Tokyo. Slip and fault displacements were estimated to be up to 40 meters (Ammon et al., 2011).

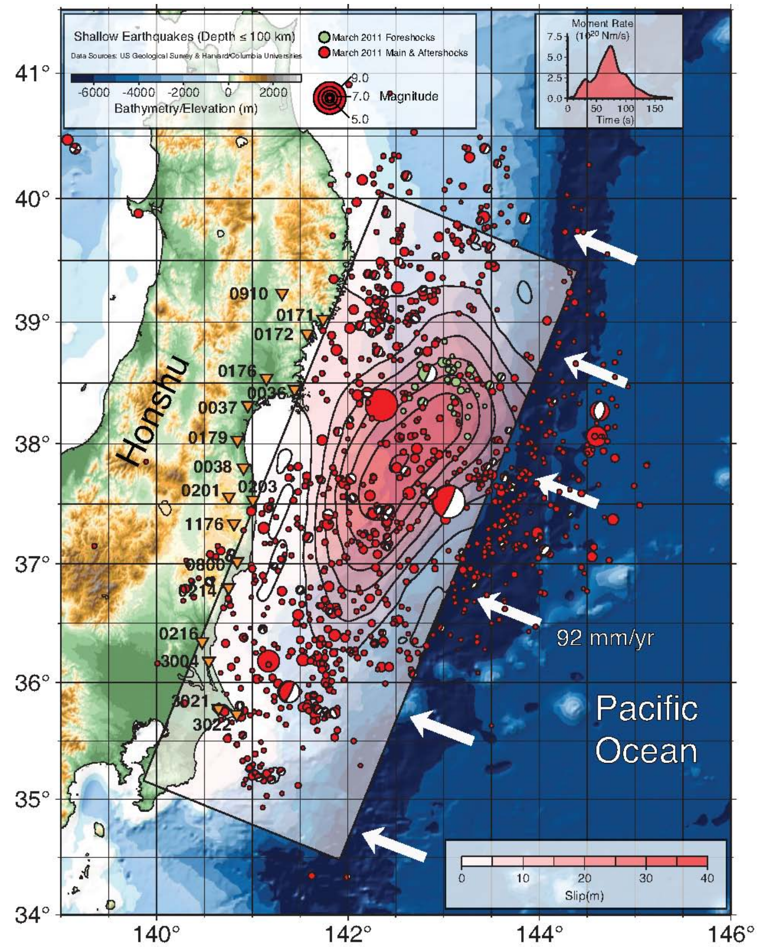

Fig. 7. Tsunami Generating Area showing the epicenter of the main earthquake on March 11, 2011 (After Ammon et al., 2011)

5.3b Review of the Mechanism of the 2011 Earthquake

In order to evaluate the tsunami source mechanism and the larger than expected heights of tsunami waves that were recorded or observed, an examination was undertaken of the above-stated seismo-tectonics of the region and of the earthquake's focal mechanism, energy release, rupture patterns and of the spatial and temporal sequencing and clustering of major aftershocks (Pararas-Carayannis 2013).

Based on this analysis, it was determined that the greater tsunami wave heights resulted from a combination of crustal deformations of the ocean floor due to up-thrust tectonic motions (Fig. 8). Additional uplift resulted from the quake's slow and long rupturing process, but also from large co-seismic lateral movements of surface seismic waves, which compressed and deformed the compacted sediments of the accretionary prism on the overriding plane.

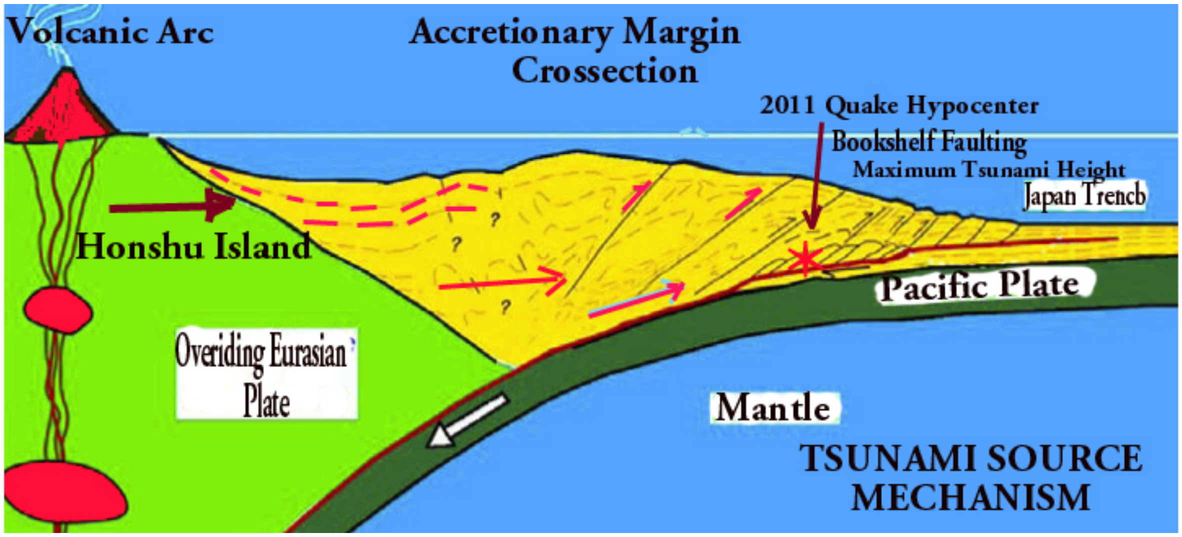

Fig. 8. Postulated Crossection of the Accretionary Margin east of Honshu Island. Compression of the Sedimentary Prism and Subsequent Normal and Bookshelf Faulting contributed to the Tsunami's Source Mechanism and to greater Tsunamigenic Efficiency.

5.3c Review of the Mechanism of the 2011 Tsunami Generation

As mentioned in section 3.2 of this report - "Love" waves do not usually affect or enhance significantly tsunami wave heights, but the 2011 earthquake in Japan was an exception because the sedimentary prism east of Honshu Island was thick and highly fractured. Thus, the surface "Love" waves contributed to lateral compression of the sediments and, in combination with "Rayleigh" waves, contributed synergistically in both normal and bookshelf faulting.

At first, the sediments on the accretionary prism compressed elastically. However the elastic deformation was short-lived, as in the next few seconds the rupturing process nucleated existing normal faults on the continental shelf on both sides of the rupture. The reverse thrust motions and the lateral compression ruptured the sedimentary layers of the accretionary prism, which begun failing sequentially in a bookshelf fashion creating several parallel and en-echelon thrust faults (Pararas-Carayannis, 2011).

The deformation occurred randomly and non-uniformly along parallel normal faults and along the oblique, en-echelon faults to the earthquake's overall rupture direction - the latter failing in a sequential bookshelf manner with variable slip angles (Fig. 8). These additional deformational changes on the accretionary margin contributed to the generation of higher tsunami waves than those resulting only from the crustal displacements.

Vertical crustal displacements due to up-thrust faulting were estimated to be more than 10 meters. From lateral compression and folding of the sediments additional uplift was estimated to be about 7 meters - mainly along the leading segment of the accretionary prism of the overriding tectonic plate as shown in Figure 8 (Pararas-Carayannis 2013).

Tsunami generation was greater along the shallow eastern segment of the fault off the Miyagi Prefecture where most of the energy release of the earthquake and the deformations occurred, while the segment off the Ibaraki Prefecture - where the rupture process was rapid - released less seismic energy, compaction and deformation of sedimentary layers. Thus the tsunami was of lesser offshore height in the Ibaraki segment (Pararas-Carayannis 2013). As postulated in the following section, the spheroidal and the toroidal modes of the earth's oscillations did not affect in any significant way the height of the tsunami waves in the near-field area.

5.3d Evaluation of the Impact of Spheroidal and Toroidal Modes to the 2011 and 2004 Earthquakes' Crustal Displacement and Heights of Tsunami Waves

In searching the literature, no reference was found on whether the relative excitement of the earth's ultra-long period from the 2011 Japan earthquake was used to calculate more accurately – or to revise - its energy and moment magnitude. In the opinion of the author, because the spheroidal oscillations have very long periods, there was no contribution to the near-field tsunami heights. Also, the spheroidal oscillations could not have affected significantly the far-field tsunami wave heights.

In the following section there is a brief discussion of the excited "spheroidal normal modes" that followed the 26 December 2004 earthquake in Indonesia, which may have contributed somewhat to the puzzling higher tsunami-like wave (2.6 meter) recorded at Manzanilo, Mexico. Although some small contribution to tsunami generation by the earth's spheroidal normal modes is possible - and as previously stated - it is not expected to be significant because of the long periods of such oscillations.

6. IMPACT OF EARTH'S SPHEROIDAL OSCILLATIONS ON EARTHQUAKE DYNAMIC MOTIONS, ON TSUNAMI GENERATION, ON ATMOSPHERIC AND ON IONOSPHERIC FLUCTUATIONS

This section of the report reviews the postulated impact by the earth's excited spheroidal oscillations on dynamic motions of the lithosphere, on far-field tsunami generation, on interactions with the atmosphere and ionosphere and, finally, on whether there was an effect on the large magnetic field deviation of the earth, known as the "South Atlantic Anomaly".

6.1 Further Evaluation of the Impact of Spheroidal and Toroidal Modes on Earthquake Dynamic Motions and Tsunami Generation

Section 5.3d included a brief summary of postulated dynamic motions caused by spheroidal and toroidal modes from the 2011 and 2004 earthquakes. Section 5.3d dealt with the mechanism of tsunami generation and whether such excited oscillations contibuted to near and far field tsunami wave height enhancement. The following summary refers to the effects that sediments can have on earthquake rupture velocity and tsunami generation for other subduction zone regions - such as Makran in the North Arabian Sea, the Sunda Trench segment in the Andaman Sea, and along the Mid-America Trench - which have been separately examined (Pararas-Carayannis, 1992; 2005; 2006).

For earthquake events in these regions, no correlation was made on whether the earth's long-period spheroidal oscillations were a partial causative factor for changes in the earthquake's rupture velocity, for the lateral or vertical displacement of surface or shallow subducted sedimentary layers, or for the augmentation in the height of tsunami waves. In all such regions of subduction, block motions of consolidated sediments were also associated with bookshelf-type of faulting, of surface sediments - which contributed to slow-rupturing, silent and deadly tsunami-earthquakes. Such was the case with the 2 September 1992 Nicaragua earthquake, with the exception that in this source region, only a limited amount of softer sedimentary layers existed in the accretionary prism. For this event, it was the slower rupture rate that contributed to the more significant tsunami that occurred.

Also, for the 1963 and 1975 earthquakes in the Kuril Islands, the large tsunami excitation was attributed to a slip in the accretionary sediment wedge (Fukao, 1979). Based on normal mode theory, Okal (1988), also showed that a tsunami source in the shallow sedimentary layer excites a much larger tsunami. The reason for such an outcome is that the extremely shallow block motions occur within shallow-subducted sediments where there is a lot of shear - thus the rupture is slower in speed. In all of such cases, the degree of sediment consolidation along a plate boundary appears to be a key factor in locking slippage on the megathrust region of the tectonic boundary, then releasing greater energy when the stress thresholds are exceeded. As already mentioned, such was the case of the 11 March 2011 earthquake in Japan, which was a megathrust event with the Pacific plate moving underneath the Eurasian plate (see Fig. 7).

As stated, great earthquakes generate strong shock waves and dynamic oscillations that affect the entire earth/water inter-phase in the oceanic regions where they strike. When they occur, the entire sea floor moves up and down from the shocks and rare-fractions that occur when massive amounts of energy are released deep in the earth. However, these are short period perturbations that occur rapidly over a time period that may last to a maximum of 60-80 seconds, a window of time may be too short for effective coupling with the water column in the source region. Thus, it is the net crustal displacements caused by an earthquake that contribute mainly to the major component of tsunami-genesis, and not the shorter time-period oscillations.

As for the effect of the earth's excited "spheroidal normal modes", such as those that followed the 26 December 2004 earthquake in Indonesia, it is possible that may have contributed somewhat to the higher tsunami-like observations observed and reported at distant stations. Although such additional contribution to tsunami generation by the earth's spheroidal normal modes is possible - and as previously stated - it is not expected to be significant because of the long periods of such oscillations.

As mentioned, what was a paradox for the 2004 tsunami was the unusually high tsunami-like wave of 2.6 meters recorded by the tide station at Manzanilo, Mexico, on the Eastern Pacific Ocean. Given the great distance of Manzanilo, Mexico, from the source region along the Sunda Trench in Western Sumatra, and the extensive chains of islands that separate the Indian from Pacific Ocean, this wave height was unusual and raises questions on whether excitment of the longest period normal modes of the earth, such as the OS2 and OS3 may have been somewhat responsible for the far-field, higher tsunami recording in Manzanilo and elsewhere, although such contribution cannot be quantitatively measured and confirmed.

6.2 Evaluation of Coupling of the Earth's Spheroidal Oscillations with the Atmosphere and Ionosphere - Generation of Atmospheric and Ionospheric Oscillations

Regarding the coupling of the excited spheroidal oscillations with the atmosphere and the ionosphere, it is also difficult to determine quantitatively (Lognonné et al.,1998; Rhie & Romanowicz 2004). It is not known if any micro-barometers recorded this coupling of the Earth's cumulative (free and excited) spheroidal oscillations with the atmopsphere following the 26 December 2004 great Sumatra earthquake, and whether distinct "normal modes" were detected. However, such combined coupling with the solid earth spheroidal motions would be expected to generate both atmospheric and ionospheric pertrubations which could be measurable by microbarographs if they were available - and by means of the Doppler Effect (Artru et al., 2001, As mentioned in section 3 of this report, delayed ionospheric oscillations of Rayleigh waves were detected and recorded by high-frequency Doppler sounding techniques from the Kuril earthquake of 11 August 1969. In fact, the 10 MHz recording of Rayleigh waves was used to estimate the initial phase of the source of this earthquake (Furumoto, 1970), and as previously indicated, such timely estimation was considered to be a useful indicator of potential tsunami-genesis, and was recommended as early as 1970 for additional use by the Pacific Tsunami Warning Center (PTWC) in issuing tsunami warnings for the Pacific Ocean (Pararas-Carayannis, 2000 a, b, c).

6.3 Evaluation of Interactions of Spheroidal Oscllations with the Earth's Magnetic Field Anomalies and Exogenous Astronomical Influences.

In section 5.2 of this report about the great Earthquake of 26 December 2004, reference was made to the very large collection of split modes, not only of the spheroidal but also of the toroidal modes (Montagner & Roult, 2004; Stein and Okal, 2005; http://www.iris.iris.edu/sumatra/ ; Park EtAl, 2005). According to Park Et.Al (2005), at periods greater than 1000 seconds, the Earth's seismic free oscillations have anomalously large amplitude when referenced to the Harvard Centroid Moment Tensor fault mechanism - which was estimated to be from 300 - to 500 - seconds surface waves. Such surface oscillations cannot affect the earth's magnetic field – which is determined by the movement of molten iron inside the earth's outer core, thousands of kilometers below the surface. The earth's internal density changes and movement of mass close to the earth's outer core and mantle interface, generates electrical currents which are mainly responsible for the earth's magnetic field and localized magnetic field anomalies. For example, when NASA satellites probing and measuring the Earth's gravity approach regions of higher density, they are pulled forward, at slightly higher speed and slow down somewhat when they reach regions of lesser crustal density.

Figure 9 is a NASA map of an area mainly affected by a growing lower magnetic anomaly, known as the "South Atlantic Anomaly". This area stretches above the earth between South America and southwest Africa, as shown. The anomaly is not related to the earth's normal or excited spheroidal oscillations. The most probable cause is the offset between the earth's magnetic and rotational poles, the weakened magnetic field poles, and the energetic particles which penetrate closer to the earth's surface in this region, where the Van Allen radiation belt is weaker. The Van Allen radiation belt is the protective zone which traps most of the energetically charged particles originating from solar winds, but not as effectively in the region of the aforementioned "South Atlantic Anomaly". Apparently, the exogenous astronomical influence of solar winds are the cause of this South Atlantic Anomaly and the earth's normal or excited spheroidal oscillations have nothing to do with it. The adverse effect of this magnetic anomaly in this particular region between South America and southwest Africa – and of concern for NASA - is only for their technological systems onboard satellites orbiting over this region.

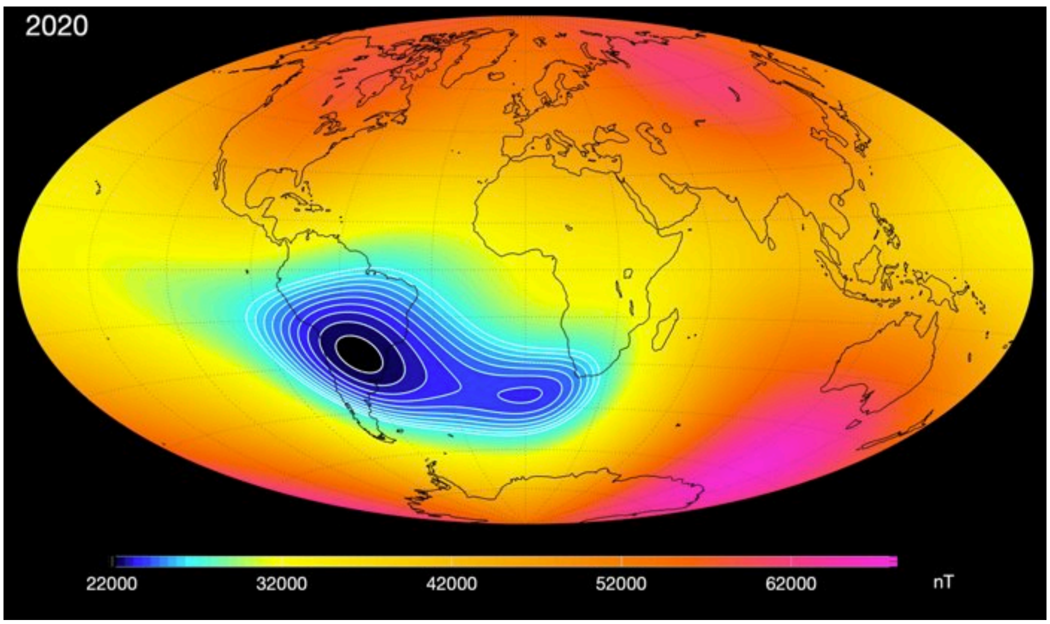

Fig. 9. Map of the region over South America and Southern Atlantic Ocesn showing the growing lower magnetic anomaly, known as the "South Atlantic Anomaly", where NASA satellites change their orbital velocities.

CONCLUSIONS

Based on the above review and preliminary evaluation, the following postulations, determinations and conclusions may be stated. Because of its rotation, the earth is aspherical and bulges in the equatorial zone region. The earth can be considered to be a mechanical system with a finite body of mass. All mechanical systems possess natural vibrations that can be excited by internal or external forces. The normal free oscillations of the earth have been extensively studied by numerous researchers following recent earthquakes. Major and great earthquakes excite the earth's free oscillations with distinct frequencies which resonate over long periods of time. Coupling of these excited spheroidal oscillations result in distinct atmospheric as well as ionospheric perturbations of certain modalities and frequencies but, as expected, to a much lesser extent lithopsheric oscillations. The coupling of excited spherical oscillations with the seas and oceans do not appear to enhance the height of tsunami waves in the near-field region of an earthquake, with a few exceptions, to far-field sea level fluctuations that resemble tsunami waves. However, atmospheric pressure disturbances from volcanic and meteorological events appear to couple more effectively with the atmosphere and the ionosphere to generate measurable pertrubations, although their possible influence on free earth oscillations cannot be easily distinguished or quantitativly measured accurately.

No correlation was made on whether the earth's long-period spheroidal oscillations result in changes in the earthquake's rupture velocity, for the lateral or vertical displacement of surface or shallow subducted sedimentary layers, or for significant augmentation in the height of tsunami waves. However research on normal mode theory, indicated that a tsunami source in the shallow sedimentary layer excites a much larger tsunami. This occurs when extremely shallow block motions occur within shallow-subducted sediments where there is a lot of shear - thus where the rupture is slower in speed. In all of the cases that have been examined by researchers, the degree of sediment consolidation along a plate boundary appears to be a key factor in locking slippage on the megathrust region of the tectonic boundary, then releasing greater energy when the stress thresholds are exceeded. The "South Atlantic Anomaly", a magnetic field between South America and southwest Africa is not related to the earth's normal or excited spheroidal oscillations. Delayed ionospheric oscillations of Rayleigh waves from large earthquakes, have been detected and recorded by high-frequency Doppler sounding techniques.

REFERENCES

Ammon, C. J., T. Lay, H. Kanamori, and M. Cleveland, 2011. A rupture model of the 2011 off the Pacific coast of Tohoku Earthquake, *Earth Planets Space*, **63**, this issue, 693–696, 2011.

Artru, J., P. Lognonné, and E . Blanc (2001), Normal **modes** modeling of postseismic ionospheric oscil-lations, *Geophys. Res. Lett., 28*,697–700.

Ben-Menahem, A., 1964. Mode-ray duality. *Bulletin of the Seismological Society of America*, **54**, 1315–1321.Google Scholar

Bromwich, T. J. I'. A., 1898. On the influence of gravity on elastic waves, and, in particular, on the vibrations of an elastic globe. *Proceedings of the London Mathematical Society*, **30**, 98–120.CrossRefGoogle Scholar

Brune, J. N., 1964. Travel times, body waves and normal modes of the Earth. *Bulletin of the Seismological Society of America*, **54**, 2099–2128.Google Scholar

Buland, R., 1981. Free oscillations of the Earth. *Annual Review of Earth and Planetary Science*, **9**, 385–413.CrossRefGoogle Scholar

Dahlen, F. A., 1968. The normal modes of a rotating, elliptical Earth. *Geophysical Journal of the Royal Astronomical Society*, **16**, 329–367.CrossRefGoogle Scholar

Dahlen, F. A. and M. L. Smith, 1975. The influence of rotation on the free oscilla- tions of the Earth, Philos. Trans. R. Soc. Lond., Ser. A, 279, 583-629, 1975.

Dahlen F. A., and Tromp J., 1998 Theoretical Global Seismology, ISBN 0-691-00124-3. Princeton, 1998. 1025 pp.

Dahlen, F. A. and Sailor R. V., 1979 Rotational and elliptical splitting of the free oscillations of the earth, Geophys. J., 58, 609-624, 1979.

Ewing, M.,W.S. Jardetzky, and F. Press (1957), *Elastic Waves in Layered Media*, McGraw-Hill, New York.

Feynman, R. P. (1963), *Lectures on Physics*, vol.1, chap.4, Addison-Wesley, Boston, Mass.

Fukao,Y., 1979 Tsunami earthquakes and subduction processes near deep-sea Trenches. J,. Geophys Res., 84, 2303-2314,1979.

Furumoto, A. S., 1970. Ionospheric recordings of Rayleigh waves for estimating source mechanism. In: Tsunamis in the Pacific Ocean., Adams, W.M., Ed., Proc. Int. Symp. on Tsunami Res. held in Honolulu, HI, Oct. 7-10, Univ. Press, Hawaii, pp. 119-133, 1970. (USE)

Geller, R. and Stein, S., 1979. Time domain attenuation measurements for fundamental spheroidal modes (0S6-0S28) for the 1977 Indonesian earthquake, Bull. Seism. Soc. Am., 69, 1671-1691, 1979.

Gower, J.(2005), Jason 1 detects the 26 December 2004 tsunami, *Eos, Trans. AGU, 86*,37–38.

Iida, K., D. C. Cox, and G. Pararas-Carayannis, 1967. Preliminary catalog of tsunamis occurring in the Pacific Ocean, *Data Report* 5, HIG-6 7–10, Hawaii Inst. Geophys. Univ. Hawaii, Honolulu, pp. 261, 1967.

He, X., and J. Tromp (1996), Normal-mode constraints on the structure of the Earth, *J.Geophys.Res.,101*,20,053–20,082.

Ji C. , http://neic.usgs.gov/neis/eq_depot/2004/eq_041226/neic_slav_ff.html.

Kanamori, H., 1971. Seismological evidence for a lithospheric normal faulting; the Sanriku earthquake of 1933, *Phys. Earth Planet. Inter.*, **4**, 289–300, 1971.

Kayal, M., and M.L.Wald (2004), Asia's deadly waves: Scientists; at Warning Center, alert for the quake, none for a tsunami,*N.Y.Times*,Sect.A,p.1,Dec.28.

Kikuchi M. & Kanamori H., 1994. The mechanism of the Deep Bolivia Earthquake of June 9, 1994. Geophysical Research Letters, Volume21, Issue 22. 1 November 1994, Pages 2341-2344

Koper, K. D., A. R. Hutko, T. Lay, C. J. Ammon, and H. Kanamori, 2011, Frequency-dependent rupture process of the 2011 M_w 9.0 Tohoku Earthquake: Comparison of short-period *P* wave backprojection images and broadband seismic rupture models, *Earth Planets Space*, **63**, this issue, 599–602, 2011.

Lamb, Horace M.A., 1982. On the Vibrations of a Spherical Shell November 1882 https://doi.org/10.1112/plms/s1-14.1.50

Lay, T., Ammon, C.J., Kanamori, H, 2011a. Outer trench-slope faulting and the 2011 M_w 9.0 off the Pacific coast of Tohoku Earthquake. *Earth Planet Sp* **63,** 37 (2011). https://doi.org/10.5047/eps.2011.05.006

Lay, T., Y. Yamazaki, C. J. Ammon, K. F. Cheung, and H. Kanamori, 2011b. The 2011 M_w9.0 off the Pacific coast of Tohoku Earthquake: Comparison of deep-water tsunami signals with finite-fault rupture model predictions, *Earth Planets Space*, **63**, this issue, 797–801, 2011b.

Lognonné, P.,C. Clévédé,and H. Kanamori (1998), Normal mode summation of seismograms and barograms in a spherical Earth with realistic atmosphere,*Geophys.J.Int.,135*,388–406.

Lognonné, P., and E. Clévédé (2002), Normal **modes** of the Earth and planets,in *International Handbook of* ***Earthquake*** *and Engineering Seismology, Part A*, edited by H.K.Lee et al., chap.10, pp.125–147, Elsevier,NewYork.

Love, A. E. H., 1911a. *Some Problems of Geodynamics*. Cambridge: Cambridge University Press. Reprinted in 1967 by Dover Publications, New York.Google Scholar

Love, A. E. H., 1911b. "Elasticity" . In Chisholm, Hugh (ed.). Encyclopædia Britannica (Eleventh ed.). Cambridge University Press – via Wikisource.

Mair, A., 2013. The fourteenth Mallet–Milne lecture. *Bull Earthquake Eng* **11,** 711–714 (2013). https://doi.org/10.1007/s10518-013-9448-1

Montagner J-P, & Genevieve Roult, 2004. Normal modes of the Earth. Institut de Physique du Globe, UMR/CNRS 7154.

https://www.researchgate.net/publication/231042632_Normal_modes_of_the_Earth

Okal E. A., 1988, Seismic parametes controlling far-field tsunami amplitudes: a review, Natural Hazards, 1, 67-96, 1988.

Okal, E. A., and Synolakis, C. E., 2004 Source discriminants for near-field tsunamis, Geophys. J. Intl., 158, 899-912, 2004.

Pararas-Carayannis G., 1989a. Five Year Plan for The Development of A Regional Warning System in the Southwest Pacific. A Report prepared for the United Nations Development Program (UNDP), New York, May 1989, 21 p.

Pararas-Carayannis G., 1989b. Editor, IOC Workshop on the Technical Aspects of Tsunami Warning Systems, Tsunami Analysis, Preparedness, Observation and Instrumentation, Novosibirsk, USSR, 4-5 August 1989, Intergovernmental Oceanographic Commission, UNESCO Report; 286 pp, Workshop Report Supplement, 1989.

Pararas-Carayannis, G., 2000a. EARLY TSUNAMI RESEARCH IN THE U.S. - A Brief History of Tsunami Research
http://www.drgeorgepc.com/TsunamiResearchHistUSA.html

Pararas-Carayannis G., 2000b "The Big One -The Next Great California Earthquake", 385pp. Forbes Press, http://www.drgeorgepc.com/BookTheBigOne.html

Pararas-Carayannis G. (2002), Evaluation of the threat of mega tsunami generation from postulated massive slope failures of island stratovolcanoes on La Palma,Canary Islands, and on the island of Hawaii, *Sci.Tsunami Haz., 20*, 251–277.

Pararas-Carayannis G. (2005), The Great Earthquake and Tsunami of 26 December 2004 in Southeast Asia and the Indian Ocean. http://drgeorgepc.com/Tsunami2004Indonesia.html

Pararas-Carayannis, G. 2011. TSUNAMIGENIC SOURCE MECHANISM AND EFFICIENCY OF THE MARCH 11, 2011 SANRIKU EARTHQUAKE IN JAPAN, Science of Tsunami Hazards. Vol 30, N2. 2011, pp 126- 152
http://tsunamisociety.org/302GPCc.pdf

Pararas-Carayannis, G. 2013. The Great Tohoku-Oki Earthquake and Tsunami of March 11, 2011 in Japan: A Critical Review and Evaluation of the Tsunami Source Mechanism. Pure and Applied Geophysics 171(12) DOI: 10.1007/s00024-013-0677-7

Park, J., et al. (2005), Earth's free oscillations excited by the 26 December 2004 Sumatra-Andaman earthquake, *Science*, **308**, 1139– 1144.
http://www.iris.iris.edu/sumatra/

Poisson, S.D. (1829) Mémoire sur l'équilibre et le Mouvement des Corps élastiques. Mémoires de l'Académie Royal des Sciences de l'Institut de France, 8, 357-570

Rayleigh (Lord) D.C.L., F.R.S., 1885 (Nov.). On Waves Propagated along the Plane Surface of an Elastic Solid https://doi.org/10.1112/plms/s1-17.1.4
https://londmathsoc.onlinelibrary.wiley.com/doi/abs/10.1112/plms/s1-17.1.4

Rhie, J., and B. Romanowicz (2004), Excitation of Earth's continuous free oscillations by atmospheric-ocean-seafloor coupling, *Nature, 431*, 552–556, doi:10.1038/nature02942.

Silver[1] P.G., Beck S. L., Wallace[2] T.C. [2], [3] Meade C., Myers[2] S.C. , James D. E. & Kuehnel R., James[1], 1995; Rupture Characteristics of the Deep Bolivian Earthquake of 9 June 1994 and the Mechanism of Deep-Focus Earthquakes, Science Vol. 268, pp 69-73, DOI: 10.1126/science.268.5207.69

Singh S.J., Rani S. (2011) Free Oscillations of the Earth. In: Gupta H.K. (eds) Encyclopedia of Solid Earth Geophysics. Encyclopedia of Earth Sciences Series. Springer, Dordrecht. https://doi.org/10.1007/978-90-481-8702-7_160

Stein, S., and M.Wysession (2003), *An Introduction to Seismology, Earthquakes, and Earth Structure*, Blackwell, Malden, Mass.

Stein S., and Okal E., 2005. Ultra-long period seismic moment of the great December 26, 2004 Sumatra earthquake and implications for the slip process

Stein, S. and Geller R., 1977, Amplitudes of the earth's split normal modes, J. Phys. Earth, 25, 117-142, 1977.

Suda, N., K. Nawa, and Y. Fukao (1998), Earth's back-ground free oscillations, *Science, 279*, 5359, 2089–2091.

Tanimoto, T., 1990. Lateral variation of Q from singlet modal Q measurements of OS2, Geophys. Res. Lett. 17, 669-672, 1990.

Tanioka, Y. and T. Seno, 2001. The sediment effect on tsunami generation of the 1896 Sanriku tsunami earthquake, *Geophys. Res. Lett.*, **28**, 3389–3392, 2001.

U.S. Geological Survey (2004), FAQ—Magnitude 9.0 off W coast of northern Sumatra,Web page dated 25 December 2004, **Earthquake** Hazards Program. Available at http://earthquake.usgs.gov/eqinthenews/2004/usslav/neic_slav_faq.html

Valette, B., 1986. About the influence of pre-stress upon adiabatic perturbations of the Earth, Geophys. J. R. astr. Soc., 85, 179-208, 1986.

Woodhouse J. H. 2008. Long period Seismology and the Earth's Free Oscillations. 9th Workshop on Three-Dimensional Modelling of Seismic Waves Generation, Propagation and their Inversion, 22 September - 4 October, 2008, International Centre for Theoretical Physics, http://indico.ictp.it/event/a07174/session/148/contribution/82/material/0/0.pdf

Woodhouse, J. H. and F. A. Dahlen, 1978. The effect of a general aspherical perturbation on the free oscillations of the Earth, Geophys. J. R. astr. Soc., 53, 335-354, 1978.

ISSN 8755-6839

SCIENCE OF TSUNAMI HAZARD

Journal of Tsunami Society International

Volume 39 **Number 4** **2020**

WWW.TSUNAMISOCIETY.ORG

TSUNAMI SOCIETY INTERNATIONAL, 1741 Ala Moana Blvd. #70, Honolulu, HI 96815, USA.

WWW.TSUNAMISOCIETY.ORG